

# INVESTIGATIONS OF CONDENSED MATTER BY MODERN NEUTRON SCATTERING METHODS

## Activity Report (theme 04-4-1121-2015/2020)

**Theme Code:** 04-4-1121-2015/2020  
**Laboratory:** Frank Laboratory of Neutron Physics  
**Department:** Neutron Investigations of Condensed Matter (NICM)  
**Field of Research:** Condensed Matter Physics  
**Theme Title:** Investigations of Condensed Matter by Modern Neutron Scattering Methods  
**Leaders:** D.P.Kozlenko, V.L.Aksenov, A.M.Balagurov

## ANNOTATION

The JINR basic facility — the IBR-2 high-flux pulsed reactor — is the leading Russian and one of the best neutron pulsed sources in the world. At the reactor, a suite of neutron spectrometers has been constructed and successfully employed in a wide range of fundamental and applied condensed matter investigations by neutron scattering techniques. In 2012, after completion of modernization, regular research activities and the realization of the FLNP User Program were resumed on the IBR-2 reactor. In previous years, the complex of IBR-2 spectrometers has been significantly upgraded, and the number of instruments has increased from 11 to 15. The research activities using neutron scattering techniques, the operation and modernization of the spectrometer complex of the IBR-2 reactor were carried out by the employees of the FLNP NICM Department. Some experimental investigations were performed in neutron and synchrotron centers in Russia and abroad in accordance with the existing cooperation agreements and accepted beam time application proposals. Within the framework of activities on the modernization of the IBR-2 spectrometers' complex the primary goals were the creation of final configuration of a new DN-6 diffractometer for studying microsamples, a multipurpose GRAINS reflectometer, a facility for neutron radiography and tomography, and scheduled modernization of the available spectrometers. The present report provides information on the most important results of scientific investigations conducted in 2018-2020 and activities on the modernization of the IBR-2 spectrometers' complex.

## **1. THEME 1121: OBJECTIVES AND ORGANIZATION OF RESEARCH ACTIVITIES IN 2018 – 2020**

The main objectives of research in the framework of the theme involved the application of neutron scattering techniques and complementary methods to investigate the structure, dynamics and microscopic properties of nanosystems and novel materials, which are of importance for the development of modern concepts in the field of condensed matter physics, materials science, chemistry, geophysics, engineering, biology and pharmacology, and have broad prospects for application in state-of-the-art technologies in power industry, electronics, pharmacology, medicine.

The experimental research activities conducted by the personnel of the FLNP NICM Department were carried out mainly on the spectrometers of the IBR-2 reactor. In addition, some experimental investigations were performed in neutron and synchrotron centers in Russia and abroad including steady-state and pulsed neutron sources in RRC KI, ISIS RAL, ILL, PSI, LLB, FRM-2, HMI, BNC, as well as synchrotron sources KSRS, ESRF and PETRA-III. This work was performed in accordance with the Topical Plan for JINR Research and International Cooperation under the existing cooperation agreements and accepted beam time application proposals.

The activities on the modernization of the IBR-2 spectrometers' complex were focused on the realization of the top-priority projects aimed at creating the final configuration of the new DN-6 diffractometer for studying microsamples, multipurpose GRAINS reflectometer, facility for neutron radiography and tomography, as well as conducting scheduled modernization of the available spectrometers.

Within the framework of investigations under the theme, the employees of the NICM Department maintained broad cooperation with many scientific organizations in JINR Member States and other countries. The cooperation, as a rule, was documented by joint protocols or agreements. In Russia, particularly active collaboration was with the thematically close organizations, such as RRC KI, PNPI, MSU, IMP UB RAS, IC RAS, INR RAS and others. A complete list of organizations cooperating with the NICM Department is given in Appendix 1.

## **2. FLNP DEPARTMENT OF NEUTRON INVESTIGATIONS OF CONDENSED MATTER**

The NICM Department structurally consists of two sectors (Diffraction and Neutron Optics) and two groups (Small-Angle Scattering and Inelastic Scattering) (**Fig. 1**). In its turn, the Diffraction Sector comprises 4 groups (HRFD/FSD, DN-2, DN-12, SKAT/EPSILON) and the Neutron Optics Sector consists of 3 groups (REMUR, REFLEX, GRAINS). In 2020, the Department's staff comprised 116 employees; among them are 9 Doctors of Science, 36 Candidates of Science, 2 Laureates of State Prize. 37 employees are from the JINR Member States and 10 employees are by-workers. As may be seen from **Fig. 2** illustrating the age distribution of the NICM Department employees, the personnel of the Department is well balanced in age and harmoniously combines highly skilled scientists with young and middle-aged specialists.

## NICM Department

### Sector 1 – Diffraction

**Group 1 – HRFD/FSD**  
**Group 2 – DN-2**  
**Group 3 – DN-12**  
**Group 4 – SKAT**

### Sector 2 – Neutron Optics

**Group 1 – REMUR**  
**Group 2 – REFLEX**  
**Group 3 – GRAINS**

### Group YuMO

### Group NERA

**Fig. 1.** Structure of the NICM Department.

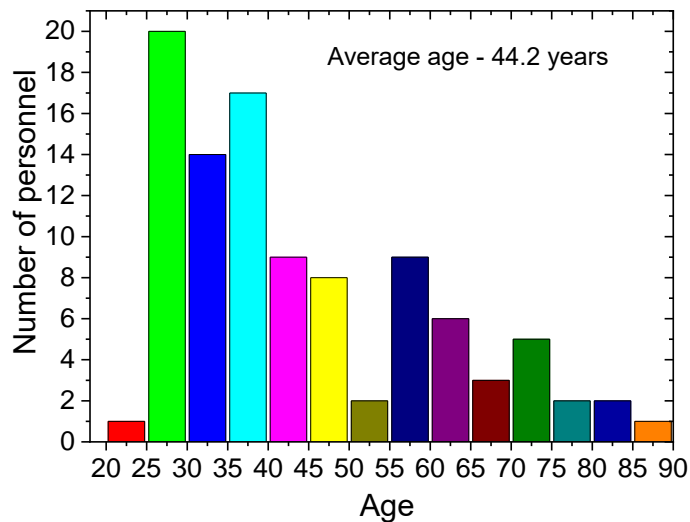


**Fig. 2.** Age distribution of the NICM Department employees (as of 2020).

In the reporting period, investigations of the NICM Department employees were regularly awarded with the JINR and FLNP prizes. Young employees of the Department were granted I.M.Frank's and F.L.Shapiro's scholarships, as well as JINR fellowships for young scientists and specialists; they repeatedly became prizewinners at the JINR Scientific Conferences of Young Scientists and Specialists. The list of most important prizes awarded to the NICM Department employees in the reporting period is given in Appendix 2.

A considerable number of grants and state contracts supervised or executed with the participation of the Department employees is a significant indicator of a high level of research being conducted and the topical importance of scientific directions being realized. A list of grants and state contracts is given in Appendix 3. All in all, during the reporting period the Department employees published 363 papers, presented 347 reports at conferences, and received 3 patents for inventions and 2 certificates of state registration of computer programs.

### 3. MAIN SCIENTIFIC RESULTS IN 2018 – 2020

The NICM Department employees are specialists in performing neutron scattering studies of condensed matter using neutron diffraction from poly- and single crystals, small-angle neutron scattering in substances with nano-scale inhomogeneities, inelastic incoherent nuclear and magnetic neutron scattering, reflection and scattering of polarized neutrons at interfaces.

A list of main scientific topics studied by the employees of the NICM Department includes:

- Investigation of the structure and properties of novel functional materials;
- Investigation of the structure and properties of materials under extreme conditions;
- Investigation of fundamental regularities of real-time processes in condensed matter;
- Investigation of atomic dynamics of materials for nuclear power engineering;
- Computer simulation of physical and chemical properties of novel crystalline and nanostructured materials;
- Investigation of magnetic properties of layered nanostructures;
- Investigation of structural characteristics of carbon- and silicon-containing nanomaterials;
- Investigation of molecular dynamics of nanomaterials;
- Investigation of magnetic colloidal systems in bulk and at interfaces;
- Structural analysis of polymer nanodispersed materials;
- Investigation of supramolecular structure and functional characteristics of biological materials;
- Investigation of structure and properties of lipid membranes and lipid complexes;
- Investigation of texture and physical properties of Earth's rocks, minerals and construction materials;
- Non-destructive control of internal stresses in industrial products and construction materials;
- Introspection of internal structure and processes in industrial products, rocks and natural heritage objects.

A characteristic feature of these studies is their interdisciplinary character involving both condensed matter physics and various allied fields of science — materials science, chemistry, biology, geology, engineering sciences.

In view of a large amount of scientific investigations carried out during the reporting period, their results are presented below in the form of brief reviews of the main studies and supplemented by a list of related publications.

#### 3.1. Structure investigations of novel oxide, intermetallic and nanostructured materials.

Recently, a new binary perovskite oxide,  $\text{Mn}_2\text{O}_3$ , was synthesized under high-pressure and high-temperature conditions. The uniqueness of this material lies in the fact that the A and B positions of the perovskite structure ( $\text{ABO}_3$ ) are occupied by the same manganese ions. A comprehensive study of the structural, magnetic, and ferroelectric properties of this material in the low-temperature region was carried out (**Fig. 3**). The existence of two complex modulated antiferromagnetic phases ( $T_{N1} \approx 100$  K,  $T_{N2} \approx 50$  K) was established. In the AFM phase arising at  $T_{N1}$ , a longitudinal spin density wave with the propagation vector  $k_1 = (0\ 0\ 1/8)$  arises. At temperatures  $T < T_{N2}$ , an incommensurate AFM phase is formed with helicoidally and cycloidally modulated components described by a combination of wave vectors  $k_{2-0} = (0\ 0\ 1.244)$ ,  $k_{2-1+} = (0\ 0\ 1.006)$ ,  $k_{2-1-} = (0\ 0\ 0.494)$ ,  $k_{2-2+} = k_{2-2-} = (0\ 0\ 0.256)$ . The spin-induced spontaneous ferroelectric polarization and the magnetoelectric effect were observed in the region  $T < T_{N2}$  [1].

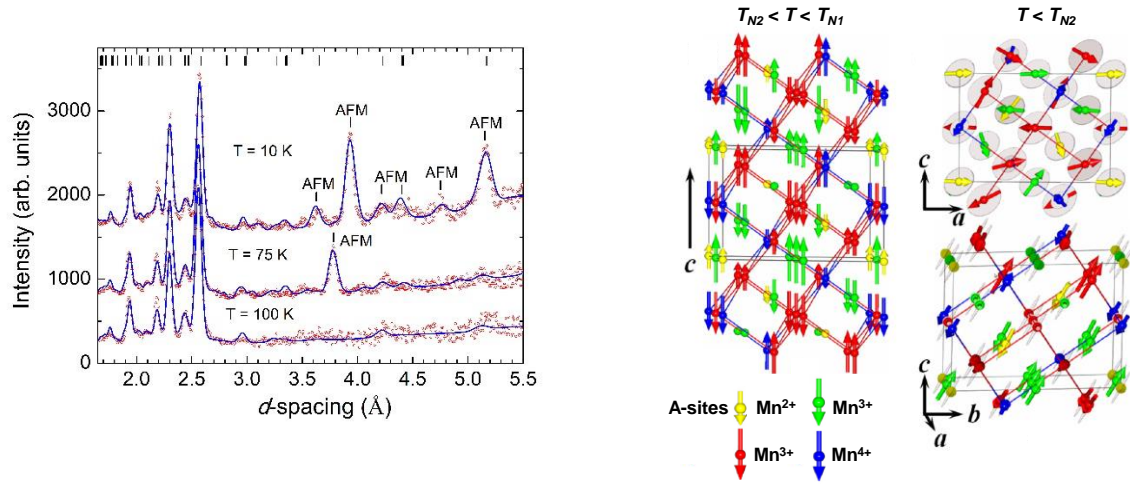


**Fig. 3.** Neutron diffraction spectra (left) and symmetry of modulated magnetic oxide structures (right) of  $\text{Mn}_2\text{O}_3$  oxide.

The structural and magnetic properties of  $\text{Ca}_3\text{Co}_2\text{O}_6$  oxide—a model quasi-one-dimensional magnetic system with spin chains—were studied by neutron and synchrotron radiation diffraction in a pressure range of up to 6.8 and 32 GPa, respectively, and temperature interval of 10-290 K [2]. Under normal pressure, an antiferromagnetic incommensurate state of a spin density wave with the propagation vector  $q_{\text{sdw}} = (0, 0, 1.01)$  and Néel temperature  $T_N = 25$  K is formed in this compound. In the temperature range  $T < 15$  K, the appearance of a disordered magnetic phase was also observed, in which the short-range order is characterized by a magnetic correlation length  $\xi = 128$  Å. Under high pressure,  $P = 2.1$ , the suppression of the incommensurate AFM phase and the emergence of a new commensurate AFM phase with a propagation vector  $q_{\text{caf}} = (0.5, -0.5, 1)$  and  $T_{\text{NC}} = 26$  K were observed (**Fig. 4**). The pressure dependence of the Curie temperature for the pressure-induced AFM phase was analyzed in the framework of the mean field theory approach, and a good agreement for the calculated value of  $dT_N/dP$  gradient with the experimental result ( $dT_N/dP \approx 0.65$  K/GPa) was obtained. The role of intra- and interchain magnetic interactions in the mechanism of the observed magnetic phase transition was analyzed in the framework of existing theoretical models.

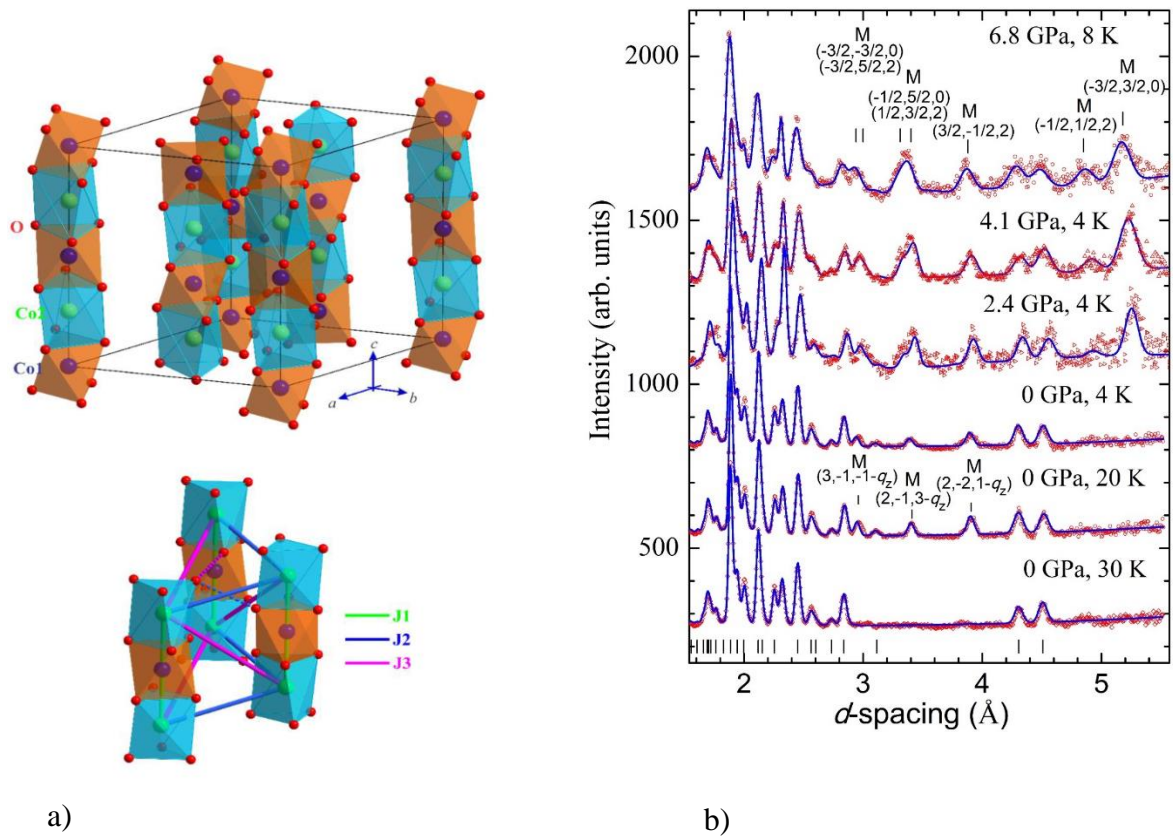


**Fig. 4.** a) Rhombohedral crystal structure (top) and the geometry of intrachain ( $J_1$ ) and interchain ( $J_2$ ,  $J_3$ ) exchange interactions (bottom) in  $\text{Ca}_3\text{Co}_2\text{O}_6$ . b) Neutron diffraction spectra of  $\text{Ca}_3\text{Co}_2\text{O}_6$  measured in the pressure range of 0-6.8 GPa and temperature range of 4-30 K and processed by the Rietveld method.

The mineral magnetite ( $\text{Fe}_3\text{O}_4$ ) is one of the first magnetic materials used by mankind since ancient times, and now it also finds wide application in the development of advanced technologies. It exhibits a number of unusual physical phenomena that have been the focus of extensive research for more than a century. Recently, the pressure-induced anomalous behavior of physical properties of magnetite in the vicinity of the structural phase transition at  $P \sim 25$ – $30$  GPa, has been discovered. To clarify the nature of this phenomenon, the magnetic and electronic properties of magnetite were studied using neutron diffraction and  $^{57}\text{Fe}$  synchrotron Mössbauer spectroscopy in the pressure range of 0-40 GPa and temperature range of 10-300 K [3]. In the high-pressure phase, the formation of ferrimagnetic ordering at a temperature of  $T_{\text{NP}} \sim 420$  K was observed and its symmetry was deduced. The structural, magnetic, and electronic phase diagram of magnetite was determined in the studied range of thermodynamic parameters (**Fig. 5**).

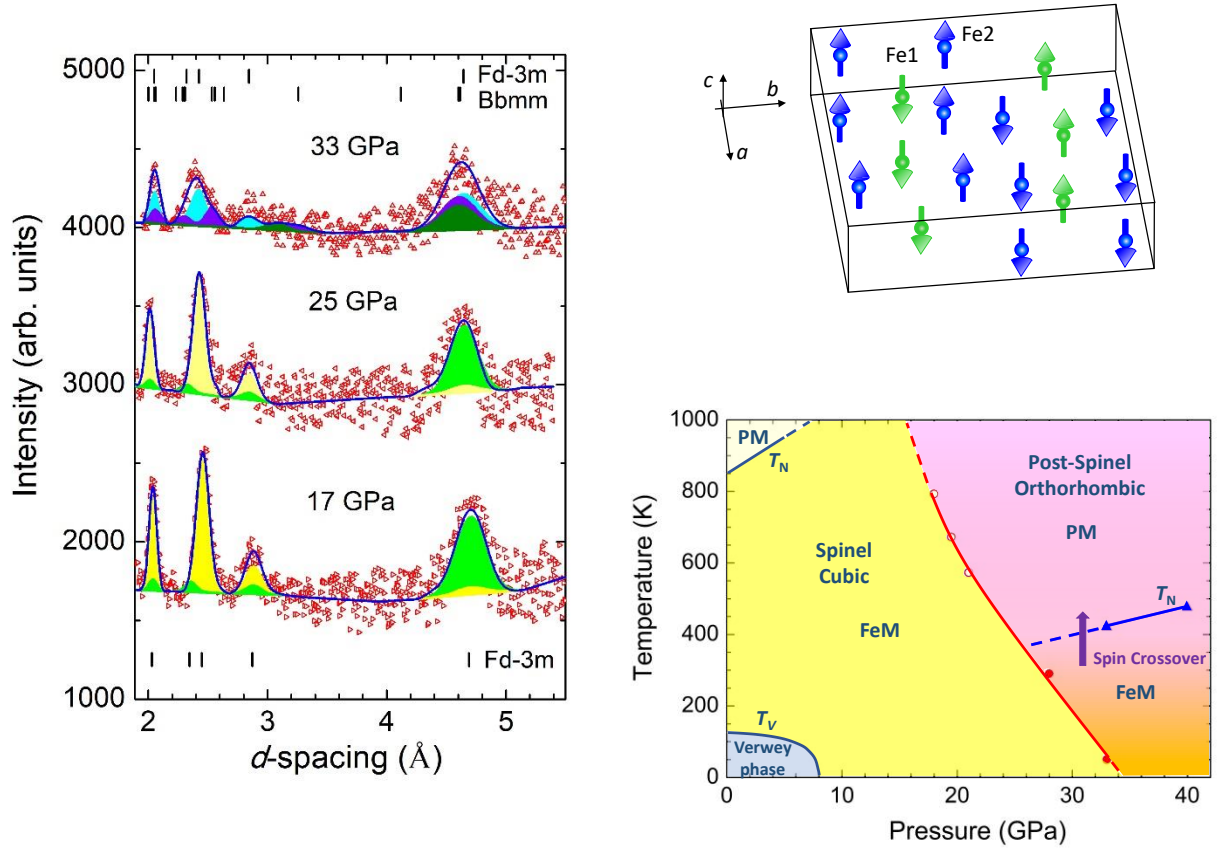


**Fig. 5.** Left: Neutron diffraction patterns of magnetite measured with a diamond anvil high-pressure cell at pressures of up to 33 GPa on the DN-6 diffractometer and treated using the Rietveld method. Right: Magnetic structure of high-pressure orthorhombic phase of magnetite (top) and structural, magnetic and electronic phase diagram of magnetite (bottom).

Steels and iron alloys have been so far the main construction materials, demonstrating an impressive diversity of useful properties. Correspondingly, they have actively been studied for centuries. At the same time, at least some fundamental properties of iron as their main component still do not have a generally accepted explanation. In particular, this concerns a mechanism of phase transitions between its allotropic modifications,  $\alpha$ - and  $\gamma$ -phases. The most commonly used Bain model in the theoretical analysis of the rearrangement of atoms during the  $\alpha \rightarrow \gamma$  transition in iron and steels implies the expansion of the bcc cell along one of the fourth-order axes by  $\sim 21\%$  and compression in the perpendicular plane by  $\sim 12\%$ . As a result, a body centered tetragonal cell is formed, where a change in the axes transforms it into an fcc cell. Such a rearrangement of atoms does not imply their coordinated displacements in contrast to the rearrangement accompanying a cooperative (martensitic) phase transition. However, the rate of transformation is so high that despite large deformations, the long-range order, in fact, holds at all stages of the rearrangement of the structure.

To obtain information on microscopic mechanisms of the rearrangement of the atomic structure in technically pure Fe, for the first time, *in situ* neutron diffraction was applied [4]. The experiments were carried out on the HRFD diffractometer with three types of samples: a fine-crystalline iron powder, as-cast iron produced by casting in a template and as-cast iron which passed a cycle of slow heating to the complete transition to the  $\gamma$  phase and slowly cooling to return to the  $\alpha$  phase. The heating-cooling cycle in the temperature range of up to  $960^\circ\text{C}$  was repeated three times. In **Fig. 6** the  $\alpha \rightarrow \gamma$  transition is shown as 2D distributions of the intensities

of peaks in the (interplanar distance vs. temperature/time) coordinates for Fe-1 (as-cast) and Fe-2 (powder) samples measured when heated at a constant rate of  $\Delta T/\Delta t \approx 0.5^\circ\text{C}/\text{min}$ . In the Fe-1 sample,  $\gamma$ -phase appears only after almost complete disappearance of  $\alpha$ -phase (**Fig. 6**). The gap between the disappearance of  $\alpha$ -phase and the appearance of  $\gamma$ -phase was confirmed on heating all studied as-cast samples within the accuracy of the content of the  $\alpha$ -phase in the middle of the gap region and its temperature width, which both depend to some extent on the heating rate. The situation for the powder Fe-2 is completely different: a change in the content of the phases occurs synchronously and with the intersection of a level of 0.5 in the middle of the time interval corresponding to the appearance of  $\gamma$ -phase and the disappearance of  $\alpha$ -phase. As can be seen from **Fig. 6**, the time interval from the beginning of a decrease in  $\alpha$ -phase to its complete disappearance in the powder is about 18 min, whereas this time interval for the as-cast sample and the corresponding temperature interval are almost twice as large.

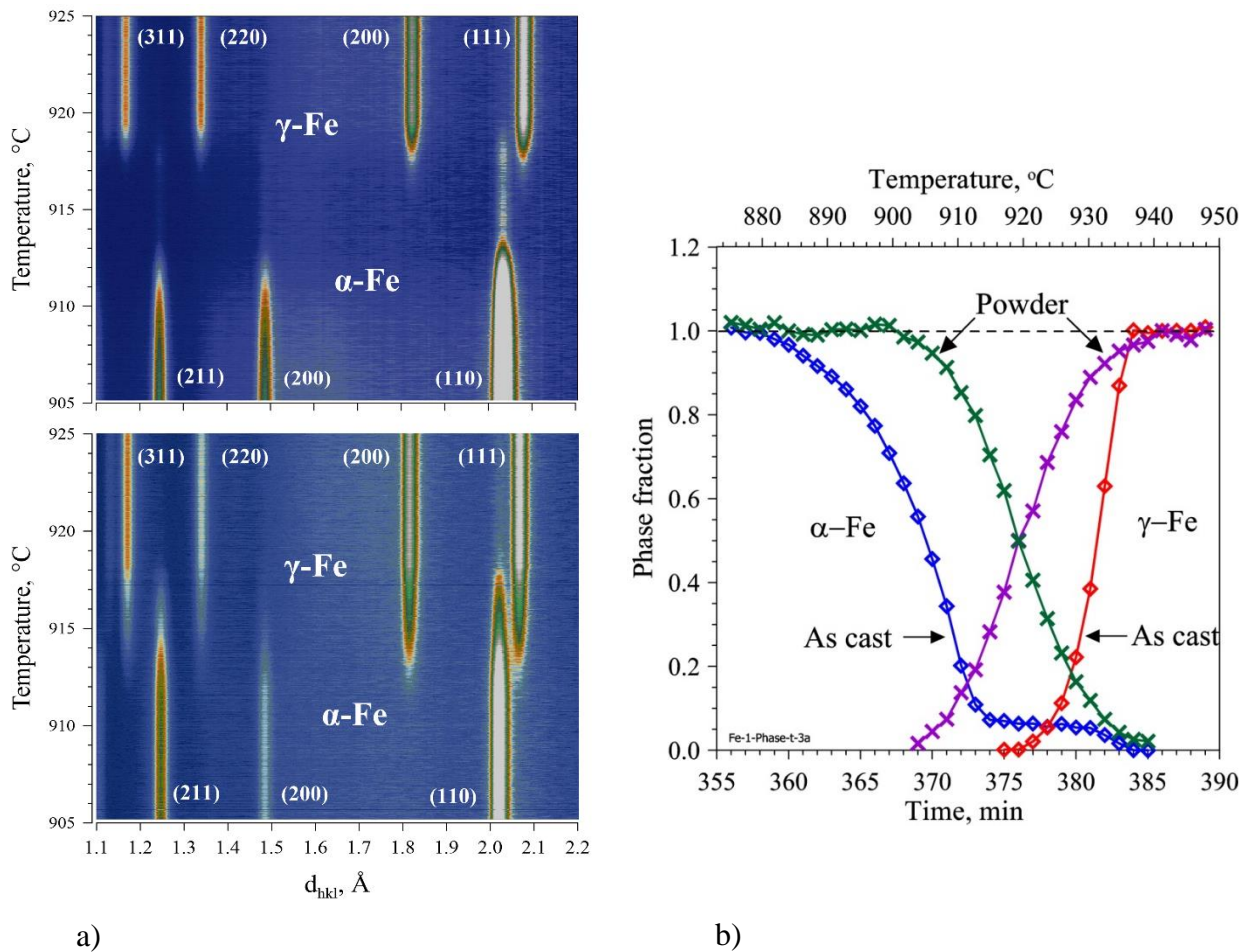


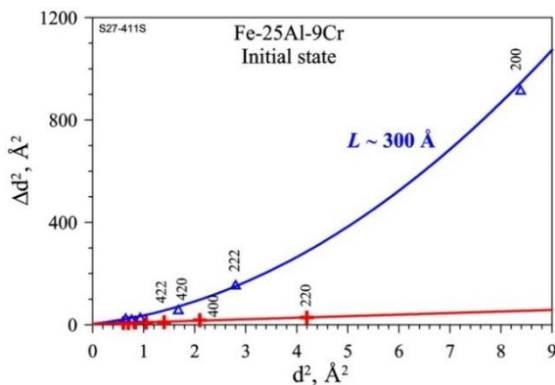
**Fig. 6.** a) 2D representation of diffraction patterns from iron samples of Fe-1 (top) and Fe-2 (bottom) upon heating. The region of  $\alpha \rightarrow \gamma$  transition corresponding to a temperature of  $911^\circ\text{C}$  is shown. The vertical axis corresponds to the temperature (and time), whereas the horizontal axis corresponds to the interplanar distance. The initial state is  $\alpha$ -Fe with indicated (110), (200) and (211) peaks. The final state is  $\gamma$ -Fe, with indicated (111), (200), (220) and (311) peaks. In both cases, the temperature increased linearly at a rate of  $\Delta T/\Delta t \approx 0.5^\circ\text{C}/\text{min}$ . Diffraction patterns were recorded every second. b) Time dependences of  $\alpha$ - and  $\gamma$ -phases in iron samples of Fe-1 (as-cast, diamonds) and Fe-2 (powder, triangles) upon heating at a rate of  $2.2^\circ\text{C}/\text{min}$ . The scales of time (below) and temperature (above) are indicated.

The effect of the disappearance of Bragg diffraction holds after repeated heating the as-cast sample but becomes less pronounced. It can be expected that the scenario of the phase transition is the same in all types of iron samples, but its kinetics varies for some reasons: it is slow during the first heating of as-cast iron and too fast for the existing possibilities for observing it in other

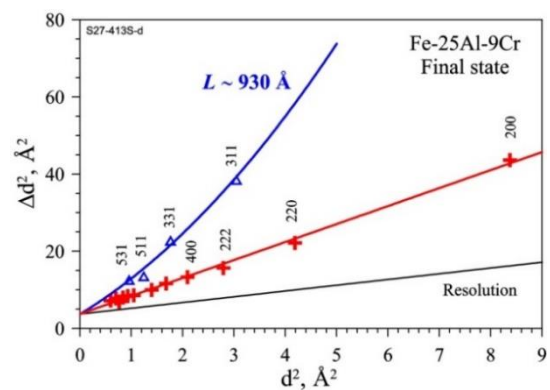
cases. It is known that the retention of the long-range order in the arrangement of atoms (and, correspondingly, the diffraction pattern) is not a necessary condition for structural phase transitions. In particular, there are compounds undergoing solid-phase amorphization under high pressure or temperature. Another possible variant of disappearance of diffraction during a polymorphic phase transition can be the fragmentation of crystallites into small (nano-) clusters with a large dispersion of the unit cell parameters. The disappearance of the long-range order during an allotropic phase transition in a metal with a simple structure is a new effect which was discovered owing to the combination of very high-resolution neutron diffraction and real-time fast thermodiffraction scanning.

On the HRFD diffractometer, the studies of intermetallic Fe- and Al-based compounds with the nominal compositions Fe-27Al-3Cr, Fe-25Al-9Cr and Fe-25Al-15Cr, were continued [5]. For the alloys of Fe-25Al type, three structural states are possible, designated in phase diagrams as A2, B2 and D0<sub>3</sub>. In the disordered A2 phase (sp. gr. *Im3m*), Fe and Al atoms occupy two possible positions with probabilities of 0.75 and 0.25. In the B2 phase with the maximum possible ordering, Fe atoms completely fill one of the two possible positions in the space group *Pm3m*, and in the second position, Fe and Al are in equal amounts. In the D0<sub>3</sub> phase, almost complete ordering is possible in the space group *Fm3m*. The D0<sub>3</sub>, B2, and A2 states can be conditionally referred to as fully ordered, partially ordered, and disordered phases, respectively, and their unit cell parameters are related as  $a_{D03} \leq 2a_{B2} \leq 2a_{A2} \approx 5.80 \text{ \AA}$ . In D0<sub>3</sub> and B2 phases, there are superstructure peaks in the neutron diffraction patterns, whose width is noticeably greater than the width of the fundamental peaks (**Fig. 7**). The explanation for this fact can be given in the framework of two models: antiphase domains (APD) and dispersed clusters, which we had proposed earlier.

When heated, in all compositions with Cr a sequence of phase transitions B2 → D0<sub>3</sub> → B2 → A2 is observed, which manifests itself as a number of effects including the formation of superstructure peaks upon heating, their disappearance at high temperatures with a simultaneous increase in the incoherent background and the successive appearance of superstructure peaks (first 200; then 111 and 311) upon cooling (**Fig. 7**). The analysis of the changes in the intensity and widths of the superstructure peaks (200) and (311) associated both with the changes in the volume occupied by the matrix and clusters, as well as with the ordering process in them, allows one to separate the contributions of these factors and determine how the size of the ordered clusters changes (**Fig. 7**). The observed wide-range variation of the ratio between the widths of the fundamental and superstructure peaks with increasing Cr content is natural in the cluster model, but it is highly unlikely in the case of APD.



a)



b)

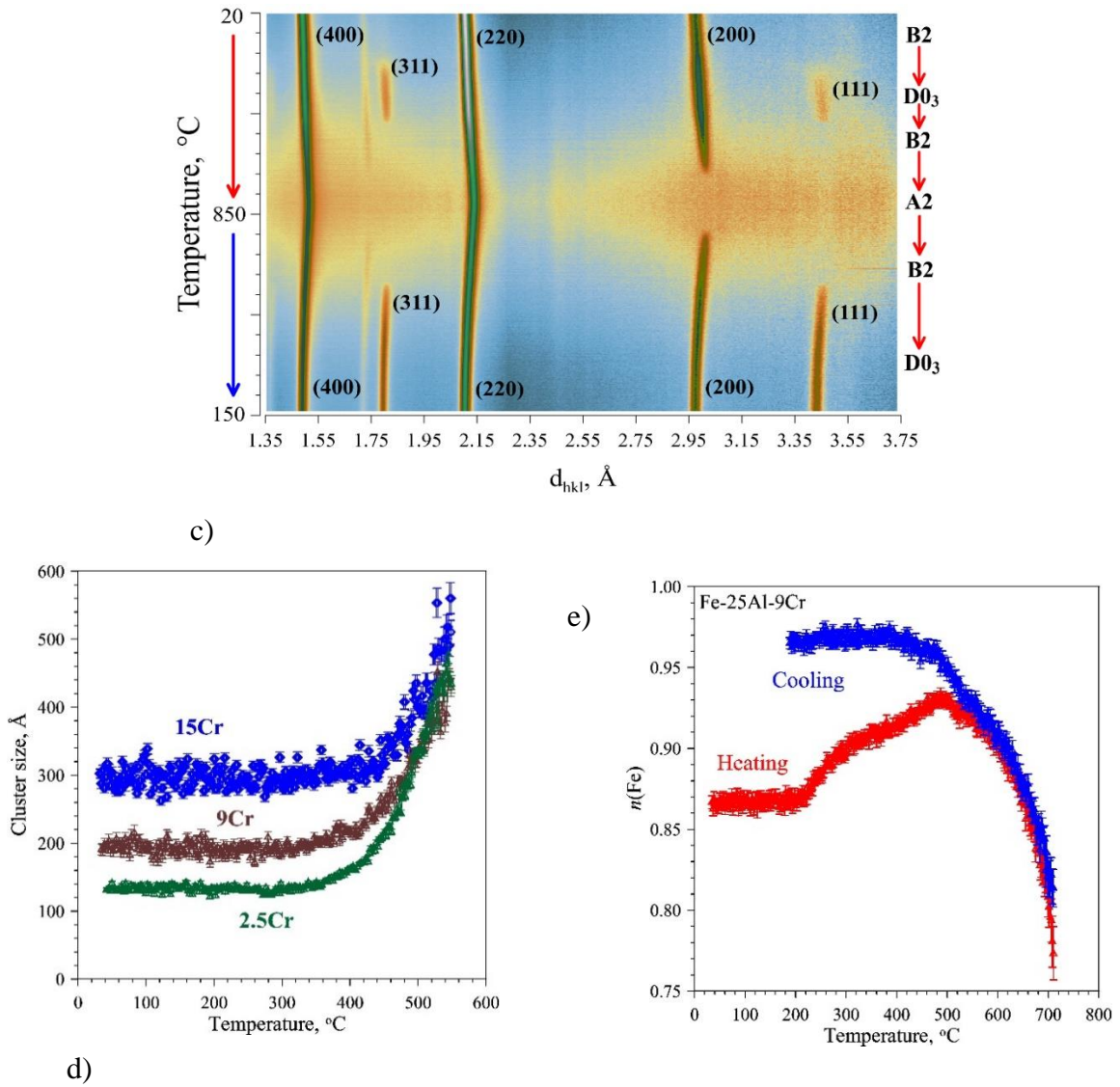


**Fig. 7.** Comparison of dependences of the peak width on the d-spacing for Fe-25Al-9Cr alloy measured in the initial state (a) and after heating up to 850°C and cooling down to 20°C (b). c) 2D representation of diffraction patterns of Fe-25Al-15Cr upon heating up to 850°C and subsequent cooling. Miller indices of the peaks are given for the unit cell of phase D0<sub>3</sub>. d) Temperature dependences of average size of clusters with ordered structure in alloys with a chromium content of 3, 9 and 15 at. % e) Temperature dependence of the occupation factor for one of the crystallographic positions of Fe atoms in Fe-9Cr-25Al alloy during heating and cooling.

Moreover, a regular increase in the cluster size naturally follows from the cluster model. The analysis of the occupation factor for one of the positions of iron atoms in Fe-25Al-9Cr showed that during slow heating from  $T \approx 220^\circ\text{C}$  to  $T \approx 500^\circ\text{C}$  the atomic ordering in the structure occurs up to  $n(\text{Fe}) \approx 0.93$ . During cooling, this parameter increases to  $n(\text{Fe}) \approx 0.97$  approaching the maximum possible value. In the analysis of nonequilibrium states gradually forming in the course of isothermal experiments, the model of dispersed clusters seems to be the most adequate. An important consequence of this is the need to clarify the well-known phase diagrams of Fe-xMe alloys for which regions of coexistence of ordered and disordered phases were found, since the volume in crystallites occupied by ordered phases, as a rule, does not exceed 50%.

Investigations of inhomogeneous phase states and their dependence on the conditions of preparation of terminal electrodes in layered cathode materials for lithium-ion batteries, were continued. Using electron scanning microscopy and X-ray diffraction on a PANalytical Empyrean 2 series diffractometer (**Fig. 8**), positive electrodes based on

$\text{Li}_x\text{Ni}_{0.8}\text{Co}_{0.15}\text{Al}_{0.05}\text{O}_2$  prepared in various ways were studied in special electrochemical cells. In particular, the rolling degree, the amount of binding material, the amount of conductive material, the storage conditions of the active material, and the level of grinding were varied. The studies have allowed us to work out the optimal method of operando experiments, including the arrangement of electrodes for reliable operation in special electrochemical cells. It was established that the complete grinding of a sample in a planetary mill (destruction of framboids to the level of crystallites), as well as charging with ultralow currents, leads to almost total suppression of phase separation during the first cycle, which conclusively confirms the microscopic nature of this phenomenon. The evolution of X-ray diffraction patterns from the ground cathode material during the first cycle is shown in **Fig. 8**. It can be seen that the structure of the cathode behaves as a solid solution during dilithiating/lithiating. It was found that the amount of the binding material has little effect on the two-phase state.

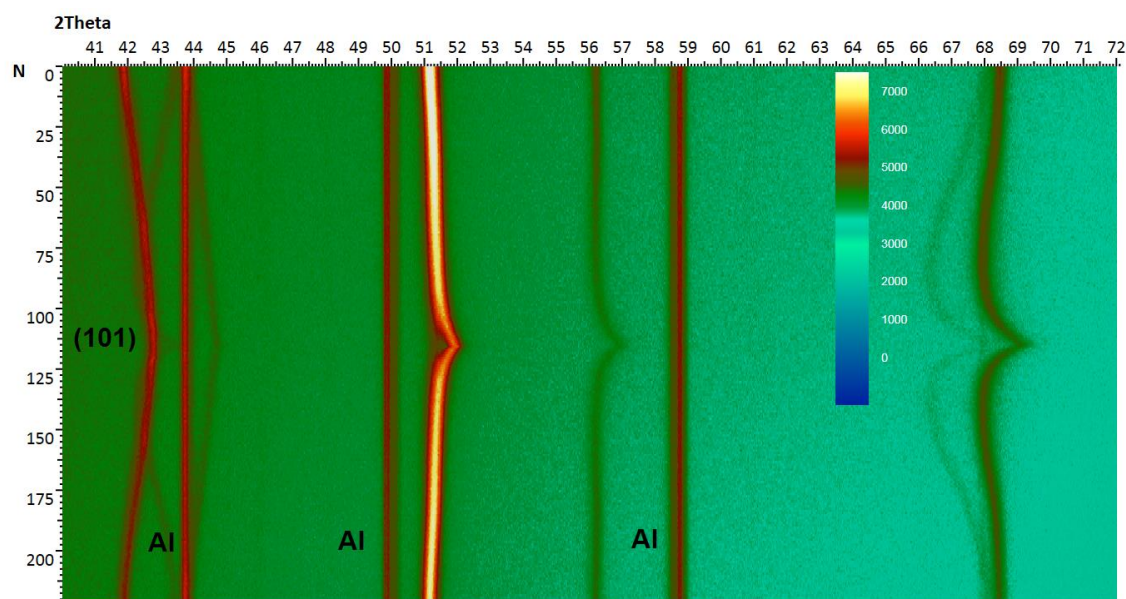


**Fig. 8.** Evolution of X-ray diffraction patterns obtained using an Emyrean diffractometer ( $\text{CoK}\alpha$  radiation) from the ground cathode material during the first charge-discharge cycle.

Work on the investigation of the structural phases and microstructural state of  $\text{Fe-xAl}$  alloys [6] was continued. Neutron diffraction experiments performed using the HRFD diffractometer with a high resolution in the interplanar spacing and employing the continuous temperature scanning mode made it possible to reveal that in cast samples (weakly nonequilibrium state) with the Al content from  $x \approx 23$  at % to  $x \approx 31$  at %, the  $\text{D0}_3$  phase has the form of nanoclusters ( $L \approx 100 \div 800 \text{ \AA}$ ) dispersed within the matrix of disordered (A2) or partially ordered (B2) phase. At the temperature scanning, the transitions  $\text{B2} \rightarrow \text{D0}_3 \rightarrow \text{B2} \rightarrow \text{A2}$  are accompanied by characteristic changes in the temperature dependence of the lattice parameter: its decrease upon ordering, and increase upon disordering (**Fig. 9**). It was found that the lattice parameters of both the matrix and clusters change simultaneously with a high degree of coherence of the crystal lattices of the matrix and clusters.

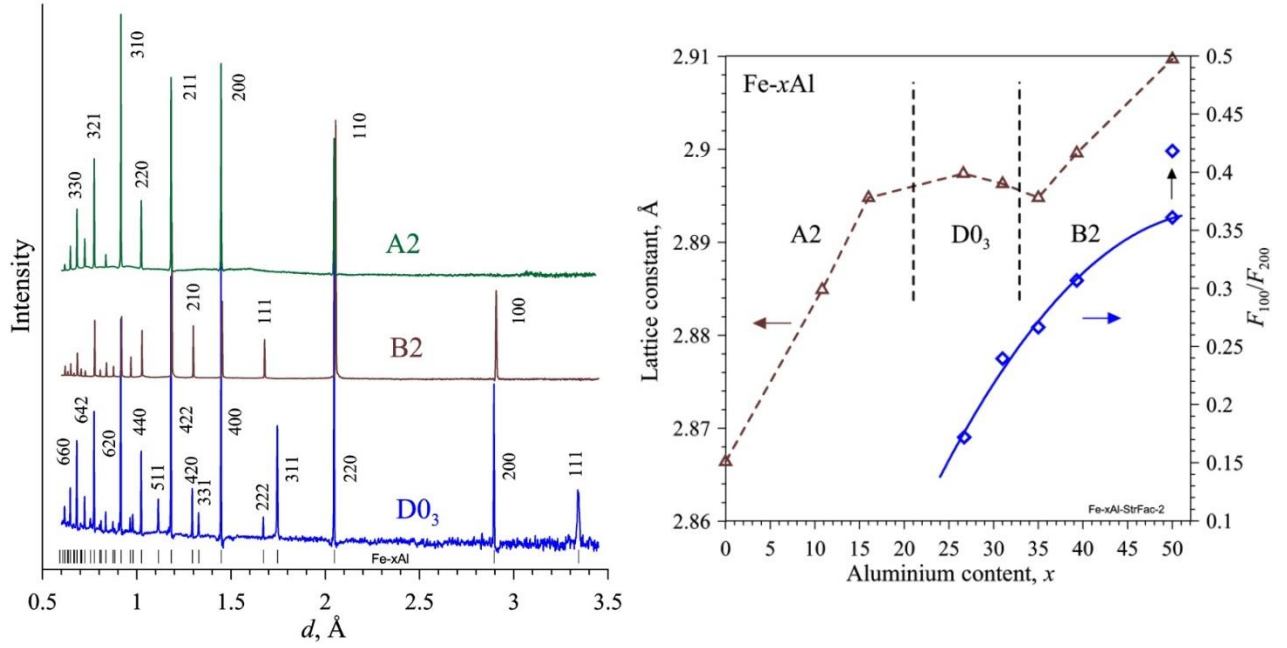


**Fig. 9.** Left: Neutron diffraction patterns of Fe- $x$ Al alloys in D0<sub>3</sub> ( $x = 27$ ), B2 ( $x = 50$ ) and A2 ( $x = 16$ ) phases. Vertical dashes indicate the calculated positions of the peaks in the D0 phase. Right: Lattice parameter (for the D0<sub>3</sub> phase,  $a' = a/2$ ) and the ratio of structure factors for the 100 and 200 reflection orders of the B2 phase as a function of  $x$ . At  $x = 50$ , two points are shown: the lower one – cast sample and the upper one – after its heating and slow cooling (nearly equilibrium state). The vertical lines provisionally divide the regions of existence of the A2, D0<sub>3</sub>, and B2 phases.

Isothermal *in situ* neutron diffraction studies of Fe- $x$ Ga alloys were carried out in the temperature range from 405 to 470 °C [7]. It was found that isothermal annealing of Fe-27.2Ga and Fe-28.0Ga alloys in the D0<sub>3</sub> structural phase at temperatures from 405 to 470 °C leads to the D0<sub>3</sub> → L<sub>12</sub> phase transition. The analysis of time dependences of the intensities of fundamental and superstructure diffraction peaks revealed that the transition between the ordered structures D0<sub>3</sub> and L<sub>12</sub> proceeds through the formation of disordered states in the sequence D0<sub>3</sub> → A2 → A1 → L<sub>12</sub>, where A1 and A2 are disordered *fcc* and *bcc* structures (**Fig. 10**). A comparatively large change in the unit cell volume during the direct transition D0<sub>3</sub> → L<sub>12</sub> with a jump in the atomic volume of about 1% makes structural reorganization through a sequence of intermediate disordered states energetically favorable. During disordering (D0<sub>3</sub> → A2) and ordering (A1 → L<sub>12</sub>) transitions, the lattice deformation is homogeneous and very small ( $\varepsilon \leq 0.001$ ), whereas during the first-order A2 → A1 transition, the linear deformations are heterogeneous and large:  $\varepsilon_c \approx 0.266$ ,  $\varepsilon_{ab} \approx -0.117$ . The rate of the D0<sub>3</sub> → L<sub>12</sub> transition changes significantly with changes in the annealing temperature and Ga content. With an increase in temperature from 405 up to 470 °C, the time needed for the formation of 50% of the L<sub>12</sub> phase decreases by a factor of ~4(5) for Fe-27.2Ga (or Fe-28.0Ga). An increase in the Ga content from 27.2 to 28.0 at.% results in an increase in the characteristic time of the transition by a factor of 1.5 to 2. The kinetics of the nucleation of the equilibrium L<sub>12</sub> phase was analyzed in the framework of the Johnson–Mehl–Avrami–Kolmogorov (JMAK) model, which was done for the first time for these materials. It should be noted that to study the kinetics of the phase transition in Fe- $x$ Ga alloys with the necessary degree of accuracy, we used a combination of high-resolution neutron diffraction and real-time measurement mode (time resolution ~1 min).

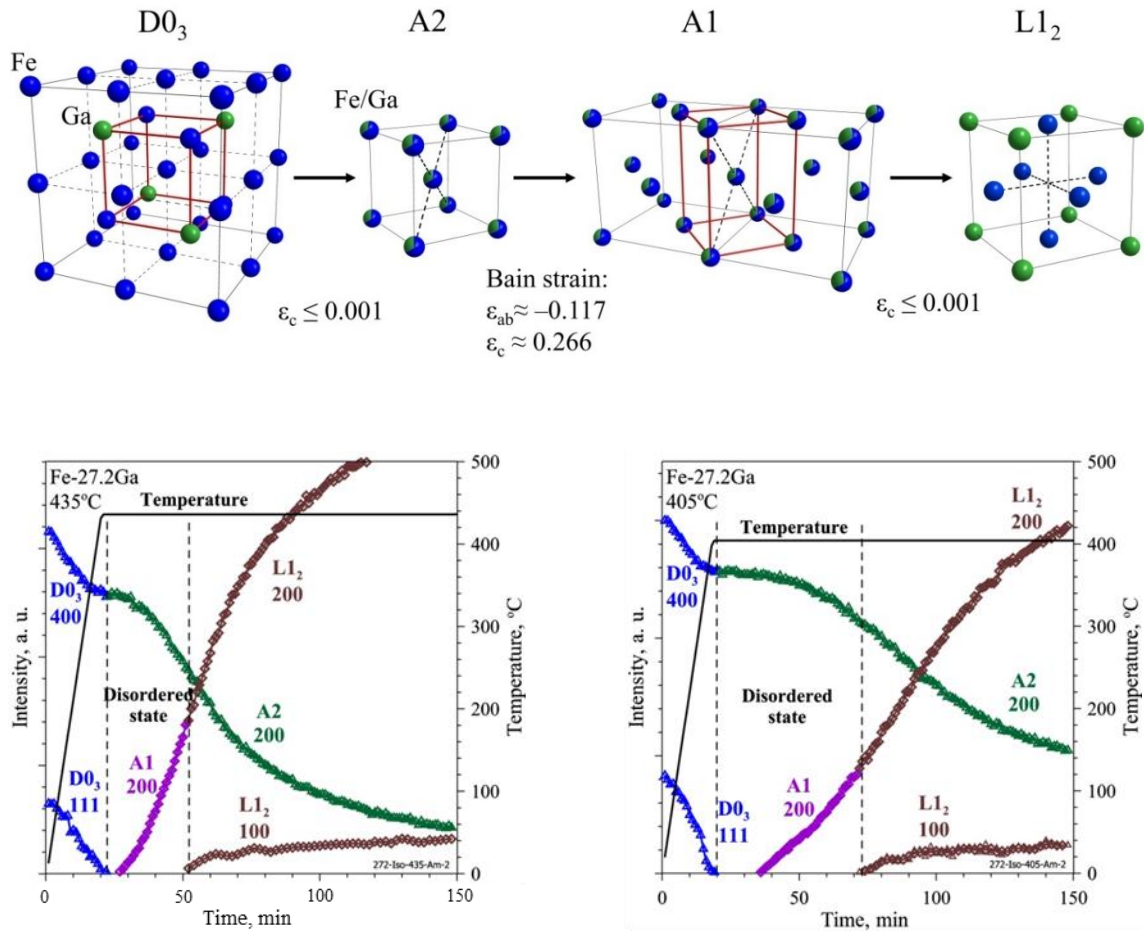


**Fig. 10.** Top: Schematic diagram of  $D0_3 \rightarrow A2 \rightarrow A1 \rightarrow L1_2$  structural transitions in Fe~(27-28)Ga alloys during isothermal annealing from 405 to 470 °C.  $D0_3$  and  $A2$  are *bcc*-based ordered and disordered structures.  $A1$  and  $L1_2$  are *fcc*-based disordered and ordered structures. The lattice deformation is small for  $D0_3 \rightarrow A2$  and  $A1 \rightarrow L1_2$  transitions and large for  $A2 \rightarrow A1$  transition. Bottom: Time evolution of intensities of fundamental ( $D0_3$ , 400 and  $L1_2$ , 200) and superstructure ( $D0_3$ , 111 and  $L1_2$ , 100) diffraction peaks upon rapid heating and subsequent isothermal annealing at 405, 435 °C (left scale). The disappearance of the ( $D0_3$ , 111) peak corresponds to the  $D0_3 \rightarrow A2$  transition, the appearance of the ( $L1_2$ , 100) peak corresponds to the  $A1 \rightarrow L1_2$  transition. The vertical lines mark the time range in which the structure is in a disordered state. The origin of the time scale corresponds to the beginning of the temperature rise.

The crystal and magnetic structures of solid solutions of strontium ferrites  $SrFe_{12-x}In_xO_{19}$  ( $x = 0.1 - 1.2$ ) were studied in a wide temperature range of 4.2-730 K by X-ray and neutron diffraction methods. In strontium ferrite samples, the occurrence of spontaneous electric polarization was detected (**Fig. 11**). To explain the mechanism of its appearance, it was proposed to describe the crystal structure of barium ferrites in the framework of non-centrosymmetric space group  $P63mc$ . The increase in the volume of the unit cell with an increase in  $x$  is explained by the larger ionic radius of In ions replacing Fe ions. In the region of low temperatures, in the range from 10 to 150 K, a region was found in which the coefficient of thermal expansion is almost zero. This behavior is explained by distortions of oxygen polyhedra.

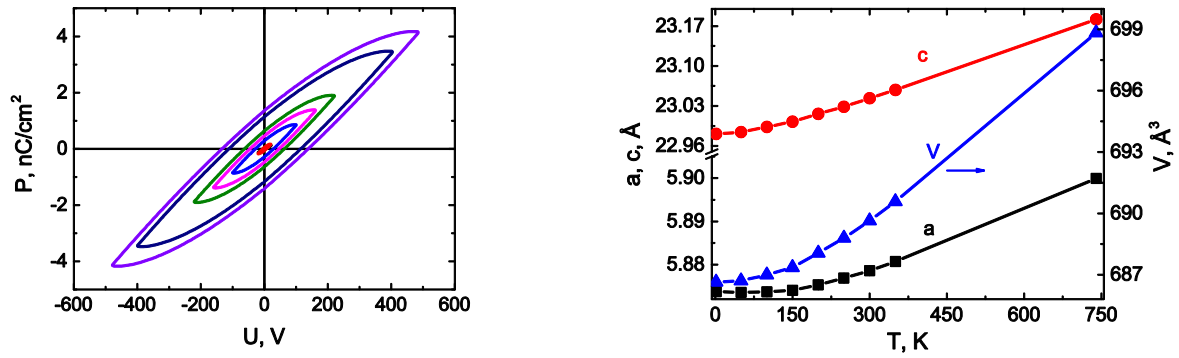


**Fig. 11.** Left: Hysteresis loops of ferroelectric polarization of SrFe<sub>11.9</sub>In<sub>0.1</sub>O<sub>19</sub> ceramics. Right: Temperature dependence of the unit cell parameters for SrFe<sub>11.9</sub>In<sub>0.1</sub>O<sub>19</sub>.

### 3.2. Investigation of magnetic fluids and nanoparticles

On the GRAINS reflectometer, neutron reflectometry experiments were carried out to study the effect of an external non-uniform magnetic field on the adsorption of magnetic nanoparticles from ferrofluids on a flat interface (magnetic fluid based on transformer oil/silicon single crystal). It was shown that the specular reflectivity curves are sensitive to the applied external magnetic field (**Fig. 12**). Thus, at low fields (< 35 mT), this system is described by a simple model with a sharp boundary between two semi-infinite media. However, there is a slight increase in the concentration of magnetic particles in the near-boundary layer. With a further increase in the external magnetic field (35-75 mT), the experimental curves can be described only by a model of several layers at the interface between the media. In this case, the formation of two adsorption layers with different content of the magnetic material in each layer is observed [8].

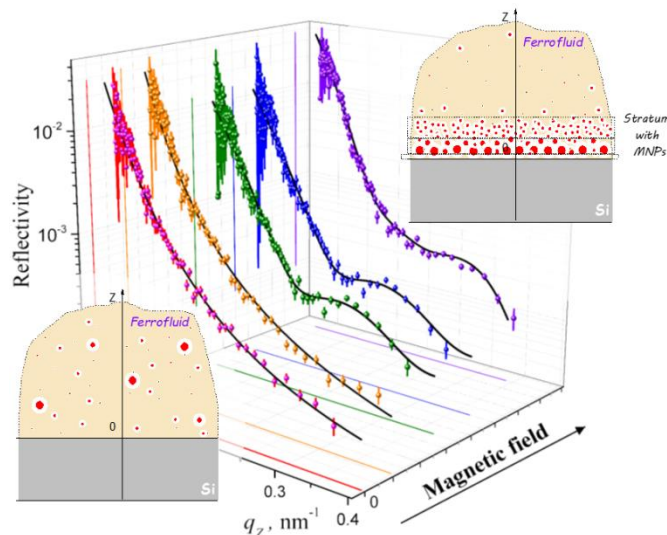


**Fig. 12.** Neutron reflectometry data and the proposed model of adsorption of magnetic particles of the ferrofluid at the interface with a solid with increasing external magnetic field strength.

The work was carried out in cooperation with the Institute of Experimental Physics of the Slovak Academy of Sciences (Košice, Slovakia) and the Faculty of Physics of the Taras Shevchenko National University of Kyiv (Kiev, Ukraine).

In the framework of the study of the effect of external electric and magnetic fields on the structure of magnetic fluids, a theoretical description of inhomogeneity in ferrofluids induced by

an external electric field was given [9]. The obtained theoretical results show that the homogeneous distribution of dielectric particles in a dielectric carrier could become inhomogeneous under an applied electric field. The reason for the development of inhomogeneity is the polarization of particles and their interaction as dipoles. It was shown that the transition to an inhomogeneous distribution has a threshold character. The critical value of the applied field increases with increasing temperature, as well as with a decrease in the number of particles and their radius. The critical value of the applied field also increases with a decrease in the difference between the dielectric permittivity of the particles and the medium. The obtained distribution of the concentration of nanoparticles according to the proposed theoretical approach is in good agreement with the experimentally observed inhomogeneous distribution of ferrofluid particles under an external electric field (**Fig. 13**).

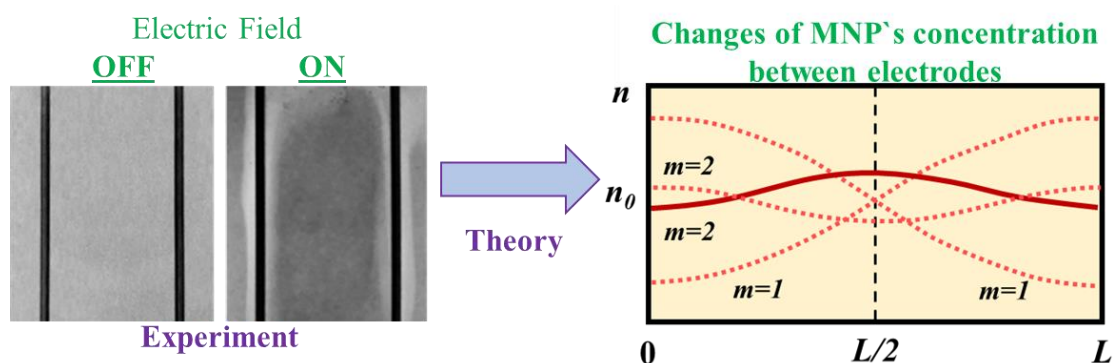


**Fig. 13.** Experimentally observed separation of magnetic particles of ferrofluids and the obtained distribution of concentration of nanoparticles between the surfaces of two electrodes according to the proposed theoretical model.

The study was carried out in collaboration with the Institute of Experimental Physics of the Slovak Academy of Sciences (Košice, Slovakia), University of Pretoria (Pretoria, South Africa) and the Faculty of Physics of Taras Shevchenko National University of Kyiv (Kiev, Ukraine).

### 3.3. Investigations of carbon nanomaterials

As a continuation of studies of fullerene complexes with anticancer drugs, structural diagnostics of fullerene C70 complex with berberine was carried out [10]. According to the data of atomic force microscopy, berberine molecules form 'sea urchin'-type structures up to millimeter sizes. The width of a single fibril is up to 8 microns. When fullerene is added to a berberine solution, the fullerene aggregates are adsorbed on the surface of berberine needles. Small particles of fullerene aggregates are located separately on the surface of the fibrils, while large aggregates form rings, or 'beads', around the fibrils. The height of the 'beads' is different and reaches 120 nm. At the same time, a part of the fullerene aggregates is not adsorbed on the surface of berberine fibers and deposited separately. The results of small-angle scattering indicate that fullerene C70 forms aggregates of the order of 60 nm in size. The scattering curves for the C70-berberine mixture show the presence in the system of larger aggregates with a fractal dimension of 2.6. Thus, it was shown that fullerene is adsorbed on berberine fibrils in water forming a specific complex (**Fig. 14**). The work was carried in cooperation with the Biological and Physical Departments of the Taras Shevchenko Kiev National University (Kiev, Ukraine).

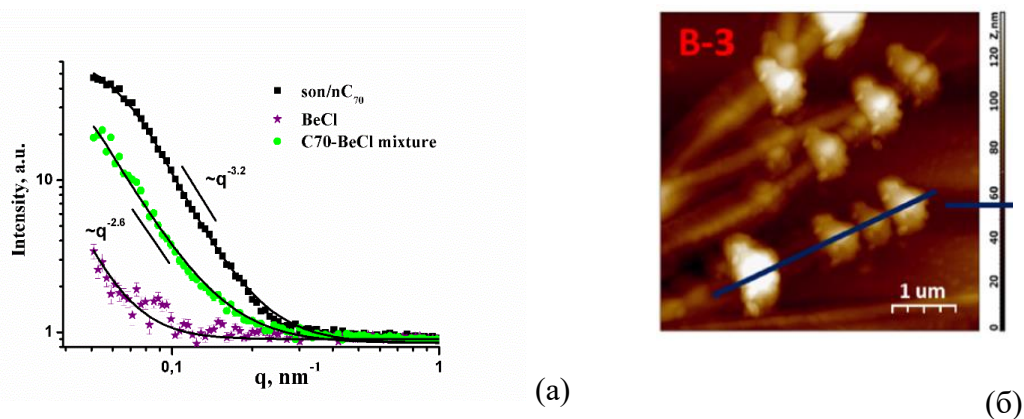


**Fig. 14.** Small-angle X-ray scattering curves from solutions of C70 and berberine in water and their mixtures (a), atomic force microscopy data upon drying of the mixture. (b).

Over the past few decades, colloidal systems based on nematic liquid crystals and nanoparticles have been actively investigated. The studies are related to potential possibilities of varying physicochemical properties of liquid crystal layers for practical applications in data storage and visualization. The features of the aggregation of diamond nanoparticles in composites based on nematic liquid crystals were investigated by small-angle neutron scattering and polarization microscopy [11]. It was shown that similar to the initial aqueous dispersions of nanodiamonds used in the synthesis, the composite system has a multi-level structure (**Fig. 15**). Nanodiamonds are assembled into fractal clusters with a dimension of 2, significantly smaller than in the original dispersions (dimension of 2.3). At the next level, clusters enter into the composition of quasilinear aggregates capable of forming a continuous network at concentrations of above 1 wt. %. Additionally, the effect of the thickness of the liquid crystal suspension layer on the aggregation process was considered. The work was performed in collaboration with the Institute of Nuclear Physics of CAS (Řež, Czech Republic), Institute of Physics of National Academy of Sciences of Ukraine (Kiev, Ukraine), and Taras Shevchenko Kiev National University (Kiev, Ukraine).

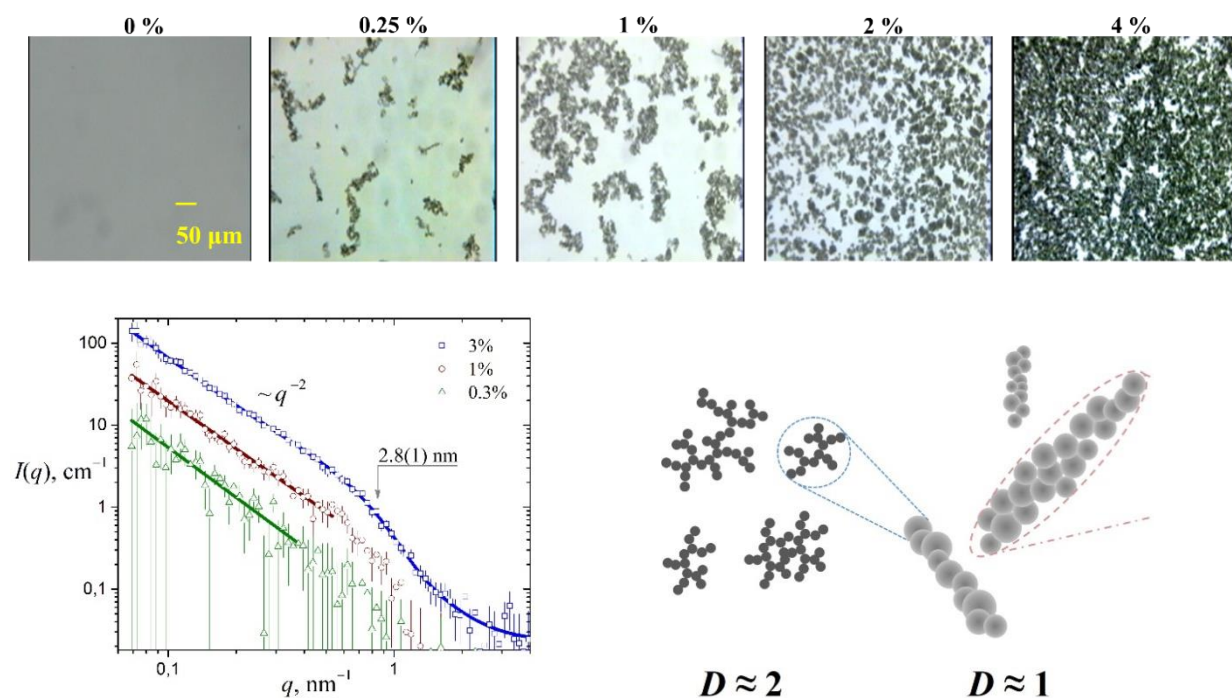


**Fig. 15.** Structural organization of liquid crystal suspension with nanodiamonds.

The investigations of a series of polystyrene/fullerene nanocomposite thin films were performed using X-ray and neutron reflectometry, as well as atomic force microscopy. Their aim was to determine the structural organization of carbon nanoparticles in nanocomposite thin films [12]. In these investigations, the structural organization of C<sub>70</sub> fullerene in polystyrene thin films was studied for the first time. Both X-ray reflectometry measurements at room temperature and variable-temperature neutron reflectometry studies using the GRAINS reflectometer were performed (**Fig. 16**). It was found that for a relative concentration of fullerene of 5 wt. %, a dense near-surface layer on a silicon substrate can be well resolved. It was shown that C<sub>70</sub> fullerenes form a less dense near-surface layer on the substrate than C<sub>60</sub> fullerenes, as a result of deeper penetration into polystyrene. Temperature studies by neutron reflectometry made it possible to determine the temperature dependence of film thickness and to evaluate the glass transition temperature of the system under study, as well as to trace the change in the structural organization of nanoparticles. It was found that the structure of the studied films varies slightly in the temperature range of 15-150 °C. This work was carried out in collaboration with the University of Rostock (Germany).

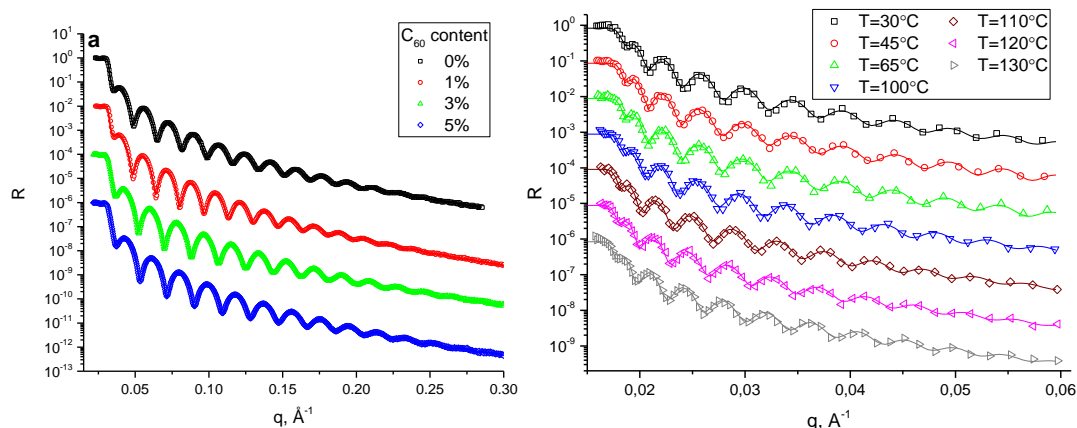


**Fig. 16.** (Left) X-ray reflectometry data for thin films of polystyrene/fullerene nanocomposites with different fullerene content. (Right) Neutron reflectometry data for a thin film of polystyrene/fullerene C<sub>60</sub> nanocomposite at different temperatures.

The dynamic light scattering method was used to measure the kinetics of aggregation of fullerenes C<sub>60</sub> and C<sub>70</sub> in solvents of different polarity. The evolution of the correlation function of light scattering was studied for 20 samples using various solvents (toluene, benzene, chlorobenzene, N-methylpyrrolidone, and pyridine). For weakly polar solvents, preparation conditions were selected to obtain a molecular solution of fullerenes. It was shown that in a hermetically sealed test tube and without exposure to light, this state will last for at least a week. The presence of oxygen and light leads to the aggregation of particles. The evolution of the correlation function of light scattering with time was measured. This work was carried out in cooperation with the Institute of Physics and Technology of the Mongolian Academy of Sciences.

In the framework of the investigation of nanodiamond-containing systems, the features of aggregation in charge-stabilized nanodiamond aqueous hydrosols with thixotropy (a sharp change in viscosity under a relatively small mechanical impact) were studied [13]. In practice, this can be observed when a sufficiently concentrated gel-like system turns into a liquid solution when shaken. Small-angle x-ray scattering experiments (P12 EMBL BioSAXS beamline, DESY, Hamburg, Germany) were supplemented by small-angle neutron scattering measurements in a wide q-range on three diffractometers, including conventional SANS experiments at the YuMO

time-of-flight small-angle diffractometer (JINR, Dubna), VSANS experiments at the FSANS time-of-flight diffractometer (BNC, Budapest, Hungary) and USANS measurements at the MAUD double-bent crystal diffractometer (NPI CAS, Rez, Czech Republic) (**Fig. 17**). Systems with concentrations below and above the threshold concentration of thixotropy were considered. The scattering curves showed that the hydrosol-hydrogel transition is accompanied by the appearance of a network of clusters present in the initial sol state as a result of an increase in the concentration of nanodiamonds in solution. Two stages in this process were revealed, which correspond to the formation of two structural levels with different compactness of cluster associates. The observed difference in the scaling properties of the network at different length scales can explain the reversibility of the sol-gel transition observed in the systems under mechanical impact: the entropy release due to the destruction of low-compact associates increases the relaxation time corresponding to the new gel formation, thus providing a comparatively long staying of the concentrated system in the liquid state.

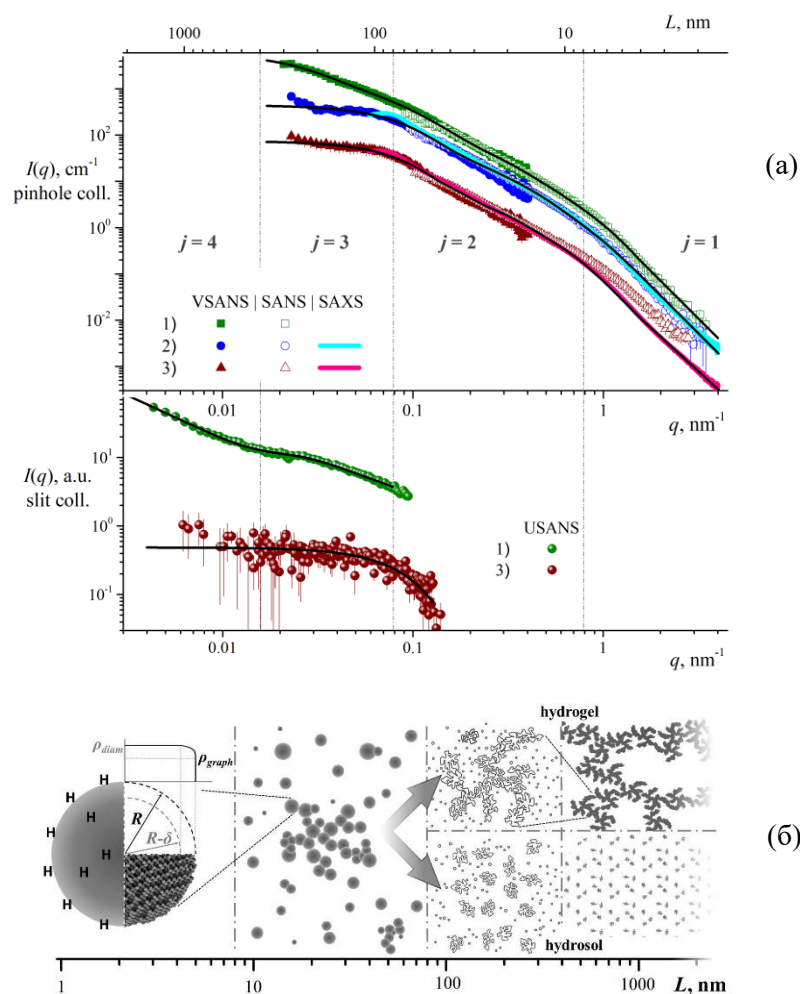


**Fig. 17.** (a) Combined experimental scattering curves for nanodiamond aqueous dispersions, obtained with different diffractometers. (b) Schematic representation of the multilevel structural organization of nanodiamond aqueous dispersions with high (gel) and low (sol) concentrations.

### 3.4. Investigation of layered nanostructures and electrochemical interfaces

In the framework of the study of ways to prevent parasitic structures on electrode surfaces in lithium batteries, a series of neutron reflectometry experiments on model electrochemical interfaces ‘liquid electrolyte/solid electrode’ were performed on the GRAINS reflectometer. The

effect of a non-electroactive additive (tetrabutyl ammonium perchlorate, TBAP) in a lithium-containing electrolyte was studied [14]. From the analysis of specular reflectivity curves obtained in the *operando* mode, it was shown that the formation of a solid-electrolyte interphase (SEI) on the electrode surface, as well as the lithium electrodeposition and growth of parasitic structures are significantly suppressed by adding a non-electroactive component to the electrolyte. The obtained scattering length density profiles perpendicular to the electrode surface (**Fig. 18**) made it possible to analyze in more detail different modes of SEI formation, as well as the formation and growth of nano-sized lithium layers in different conditions. The work was carried out in collaboration with the Chemical Department of Lomonosov Moscow State University (Moscow, Russia).

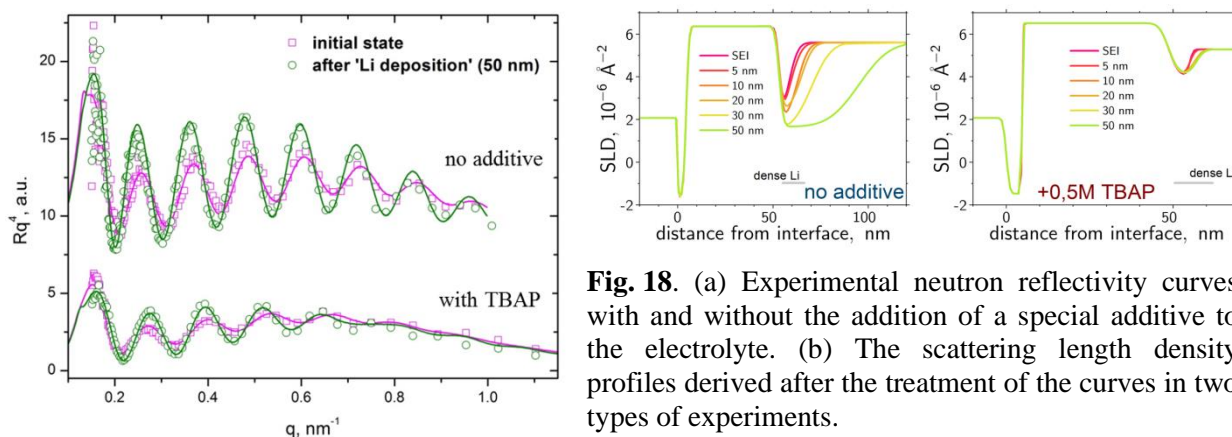


**Fig. 18.** (a) Experimental neutron reflectivity curves with and without the addition of a special additive to the electrolyte. (b) The scattering length density profiles derived after the treatment of the curves in two types of experiments.

In the framework of the study of conditions for the formation and growth of surface structures on electrodes in lithium-ion batteries, the effect of electrolyte concentration on the formation of the solid electrolyte interphase (SEI) and subsequent electrochemical deposition of lithium on a planar metal (copper) electrode was studied using the GRAINS reflectometer in the *in-situ* mode [15]. Specular neutron reflectometry experiments on special electrochemical cells with model solid electrode/liquid electrolyte interfaces were carried out in addition to the electrochemical characterization (measurements of impedance and Coulomb efficiency, optical control). The two-stage character of deposition was confirmed, when, first, a dense near-surface layer consisting of the products of chemical interaction of lithium with the solvent is deposited on the surface of the electrode, and then a transition layer is formed, which corresponds to the beginning of the development of large microscopic inhomogeneities (needlelike structures). In the case of concentrated electrolytes (**Fig. 19**), strong suppression of the growth of the near-surface layer is observed, which is similar to the previously studied effect of non-electroactive additives in the electrolyte, which results in a change in the morphology of needlelike structures. The work was carried out in cooperation with the Department of Chemistry of Lomonosov Moscow State University (Moscow, Russia) and Dubna State University (Dubna, Moscow Region, Russia).

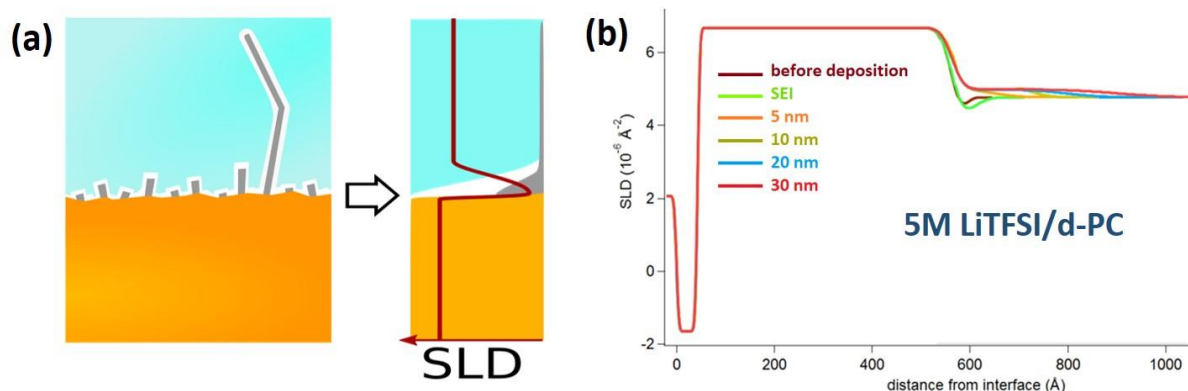


**Fig. 19.** (a) Structure of inhomogeneities on the surface of the metal electrode in contact with the liquid electrolyte from the experimental specular neutron reflectometry data. The specific feature in the scattering length density depth profile at the interface contains information on the two-stage nature of the electrochemically deposited lithium layer: first, a dense near-surface layer with a high lithium content (presumably in the form of oxide) is formed on the electrode surface, and then a transition layer is formed, which corresponds to the beginning of the development of large microscopic inhomogeneities (needlelike structures). (b) Suppression of the growth of the near-surface layer in the case of a concentrated electrolyte from the obtained SLD profiles according to neutron reflectometry data.

Small-angle neutron scattering (YuMO spectrometer) was applied in structural studies of currently-used electrodes and components of electrochemical cells using carbon materials. In particular, we studied the microstructure of ion-conducting ceramic membranes for separators in advanced lithium-air batteries with carbon cathodes for separating active liquid electrolytes and lithium anodes. It was shown that the use of a homogenizing additive (yttrium) in the synthesis of these membranes leads to a significant improvement in their conductive properties, which can be explained by an increase in the number of intergrain contacts. SANS was applied for a detailed description of the modes of nucleation and growth of crystalline grains at different content of the homogenizer and various annealing modes [16] with subsequent optimization of the synthesis procedure. Also, using SANS, the effect of conductive carbon additives (carbon black, graphene, carbon nanotubes) on the porous structure of cathodes based on lithium iron phosphate  $\text{LiFePO}_4$  (LFP) was studied [17]. To separate scattering by closed pores from scattering by open pores, the electrode is soaked with a deuterated electrolyte, which makes it possible to compensate for the scattering by open pores. It was found that the used additives change the electrode porosity to a different extent and affect the wettability of the material both due to different efficiency of incorporation of the initial material into the pores and their effect on the LFP matrix.

Using *ex-situ* SANS experiments (**Fig. 20**), the filling of the pores of a carbon cathode with the final product of the electrochemical reaction (lithium peroxide) during the discharge of lithium-oxygen cells was studied [18]. This type of batteries has a significantly higher capacity compared to the widely used lithium-ion batteries. However, their application meets a number of difficulties associated with the blocking of the diffusion of oxygen in the electrolyte because of the clogging of the pores with lithium peroxide. The SANS data made it possible to link the changes in the cathode at the nanometer scale with the electrochemical characteristics of the cells and helped to clarify the mechanisms that limit their capacity. It was shown that the oxygen transport pathways in the wetted cathode are blocked both by the passivation of the inner surface of the pores inside the carbon grains and because of the growth of supramolecular structures (mesocrystals) in the intergrain space, and the nature of these phenomena significantly depends on the type of the organic solvent in the electrolyte, as well as the content of residual water molecules in it. The work was carried out in cooperation with the Department of Chemistry of

Lomonosov Moscow State University (Moscow, Russia) and Dubna State University (Dubna, Moscow Region, Russia).

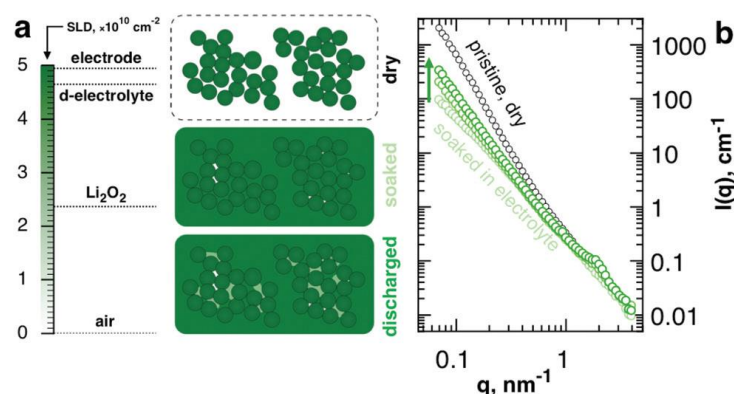


**Fig. 20.** Schematic of the SANS experiment (a) and experimental scattering curves (b) from carbon cathodes for lithium-oxygen batteries. A liquid electrolyte with a deuterated solvent fills open pores in macroscopic grains, compensating for the scattering by a carbon matrix. During discharge, lithium peroxide is formed in these pores. Due to the sufficient contrast with the matrix, the scattering is again enhanced, which is analyzed in the course of the experiment.

On the REMUR reflectometer, studies of ferromagnetic-superconducting structures were continued [19]. A feature of the layered structures with thin layers is the simultaneous presence of magnetic clusters and domains. These magnetic systems interact with each other. An unusual magnetic state has been discovered. It appears in a thin magnetic layer, which is in contact with the superconducting layer, in a narrow temperature range below the superconductivity critical temperature. A characteristic feature of this state is that in the pre-magnetized magnetic layer the magnetic moments of the clusters start to orient themselves opposite to the applied magnetic field, so that the magnetic induction becomes zero. A state with zero magnetic induction is favourable for establishing superconductivity. The formation of the superconducting state in the magnetic layer at a certain “resonant” temperature is indirectly indicative of a resonant nature due to the interference of different multiplicity of reflection of a superconducting pair in a magnetic layer.

**Figure 21** shows a magnetic structure and superconducting state for pre-magnetized nanostructure Nb(70nm)/Ni<sub>0.65</sub>Cu<sub>0.35</sub>(6.5 nm) at non-“resonant” (left) and “resonant” (right) temperatures. In the first case, at a temperature below the critical one for niobium, in the magnetic layer there is a superconducting layer (about 1-2 nm thick) adjacent to niobium, which is reflected in a decreasing density of superconducting pairs  $n_p$  over magnetic layer depth and non-zero magnetic induction in the magnetic layer.

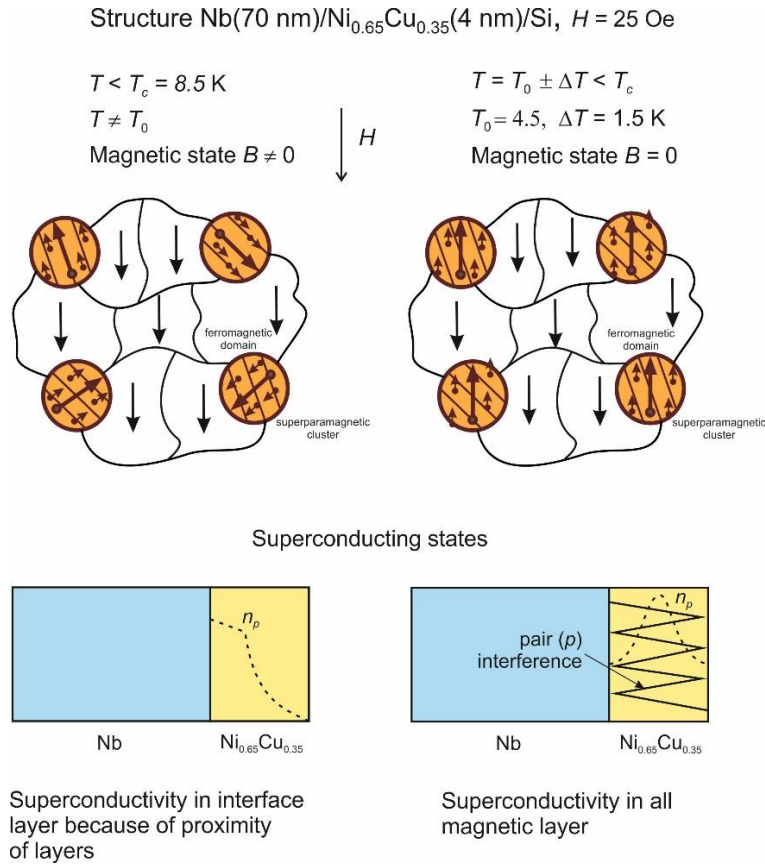


**Fig. 21.** Magnetic structure and superconducting state for pre-magnetized structure Nb(70nm)/Ni<sub>0.65</sub>Cu<sub>0.35</sub>(6.5nm) at non-“resonant” (left) and “resonant” (right) temperatures.

In the case of the “resonant” temperature, due to the interference of the waves of the superconducting pair, reflected from the boundaries of the magnetic layer, the density of the pairs increases, and the magnetic layer undergoes a transition to a superconducting state. In this case, the clusters are oriented against the magnetization of the surrounding ferromagnetic medium so that the magnetic induction becomes zero. Thus, the “resonant” superconductivity in the magnetic layer is accompanied by the establishment of zero magnetic field induction. This happens due to the interference amplification of the superconducting state.

In the framework of the study of coatings based on transition metal oxides (TMO) aimed at improving the mechanical and optical properties of materials, as well as increasing their wear resistance, X-ray reflectometry studies of thin films of titanium oxides (TiO<sub>2</sub>) and tantalum (TaO) were carried out. TiO<sub>2</sub> coatings are widely used in applications where biocompatibility is required (for example, dental implants), in optical filters, and in humidity sensors (changes in electronic characteristics due to water sorption). TaO coatings significantly improve the corrosion resistance of metals at high temperatures. It is important that the parameters of films (thickness, roughness, density) directly affect their functional properties. At the first stage, in reflectometry experiments (**Fig. 22**), we determined the quality of TiO<sub>2</sub> and TaO nanolayers deposited on a glass substrate, as well as evaluated the efficiency of the magnetron sputtering technology used in the synthesis of samples.

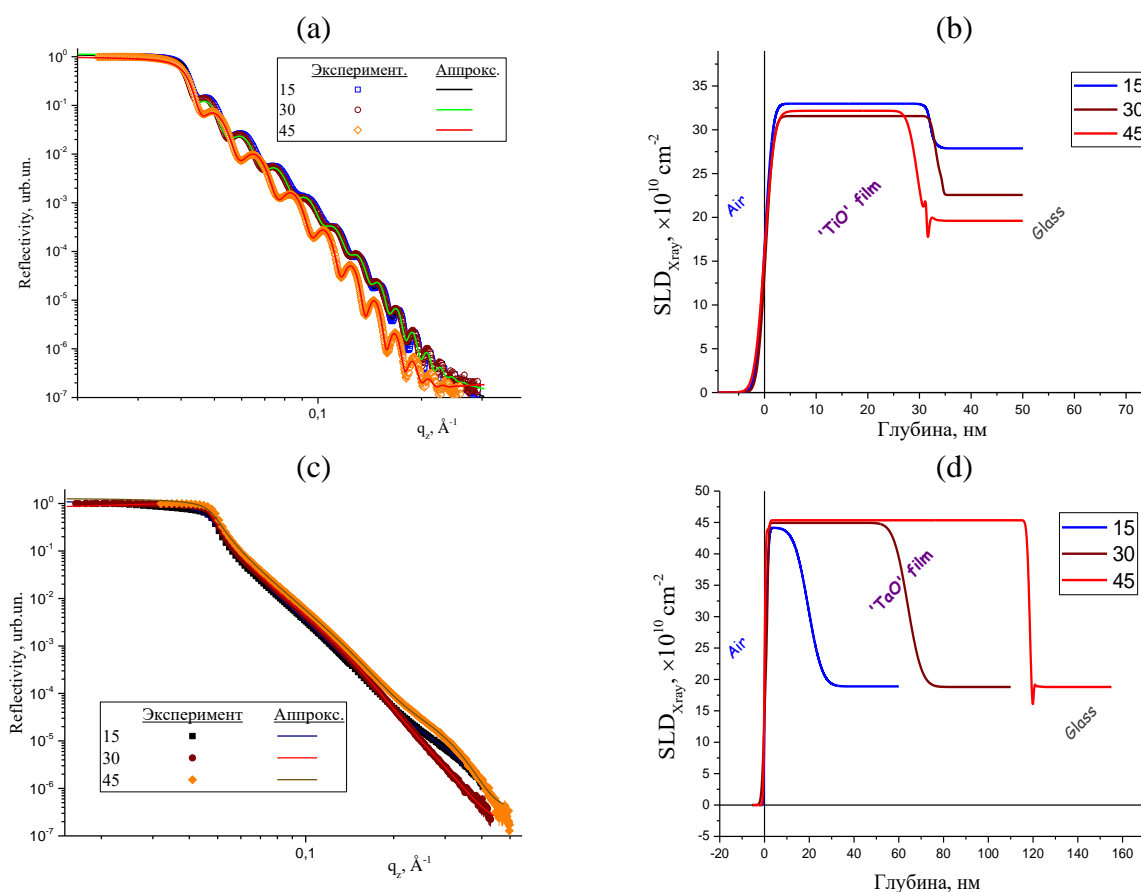


**Fig. 22.** Experimental X-ray reflectometry curves (symbols) and their model approximations (lines) for a series of TiO<sub>2</sub> (a) and TaO (c) films on glass substrates for various values of the geometric parameter related to the location in the deposition chamber. The obtained scattering length density profiles for TiO<sub>2</sub> (b) and TaO (d) films.

From the analysis of the experimental data for TiO<sub>2</sub>, it follows that depending on the modes set during sputtering (potential differences between electrodes, currents, and vacuum conditions), TiO<sub>2</sub> coating is deposited on the substrates with a thickness in the range of 29-35 nm and a high roughness index (up to 2.5 nm), as well as transition (diffuse) layers of considerable thickness. There is a clear dependence of the thickness of the useful layer on the external parameter (tilt angle of the substrate in respect to the sputtering source): the most significant changes are observed for the case with the largest tilt angle of the sample in the deposition chamber. At the same time, the highest density of the substance of the useful layer of TiO<sub>2</sub> is realized in the mode with the least tilt angle of the sample. In the case of TaO deposition, there is a regular tilt angle dependence of the layer thickness. With an increase in the tilt angle of the substrate, the thickness of the TaO layer increases in the range of 18-140 nm. A characteristic feature is the constancy of the optical density of the substance (SLD) of the useful layer, the value of which is significantly less than the calculated value for the close-packed crystalline structure of TaO. This fact is indicative of the possible formation of an amorphous phase of TaO in films.

### 3.5 Investigation of biological nanosystems, lipid membranes and lipid complexes

Poly(2-oxazoline)s are a universal material for designing polymer objects with complex architecture and adjustable physicochemical properties. High biocompatibility and the possibility of replacing polyethylene glycol (PEG) with these polymers in medical applications attract great interest in their research. Besides, as compared with PEG, poly(2-oxazoline)s possess additional

useful physicochemical properties, such as low viscosity and high stability. Furthermore, it has recently been demonstrated that an immune system may produce anti-PEG antibodies, which results in accelerated blood clearance of PEG-containing medicinal preparations. This fact arouses additional interest in the studies of poly(2-oxazoline)s as PEG substitutes.

SANS was used for studying the structure of star-shaped poly(2-ethyl-2-oxazoline) and poly(2-isopropyl-2-oxazoline) with “arms” grafted to the lower rim of thiacalix[4]arene, hereinafter star-ETOX and star-PIPOX, in aqueous medium, 6 mg/ml in D<sub>2</sub>O [20]. On the basis of the SANS analysis, a model of supramolecular organization was proposed for star-PETOX and star-PIPOX (**Fig. 23**). The shape parameter,  $\varrho = R_g/R_H$ , where  $R_g$  is the radius of gyration derived from the SANS data and  $R_H$  is the hydrodynamic radius obtained by the dynamic light scattering method (DLS), was found to be 1.6 and 1.5 for the second structural level for star-PETOX and star- PIPOX in D<sub>2</sub>O, respectively. The obtained  $\varrho$ -values correspond to the range of 1.4-1.8, evidencing the formation of molecular-dispersity stars. The number of clusters forming an aggregate of the second structural level was estimated to be 12 clusters for star-PETOX and 19 clusters for star-PIPOX. Using atomic-force microscopy (AFM) and ultra small-angle neutron scattering (USANS), it was shown that these aggregates can then be assembled into agglomerates (**Fig. 23**).

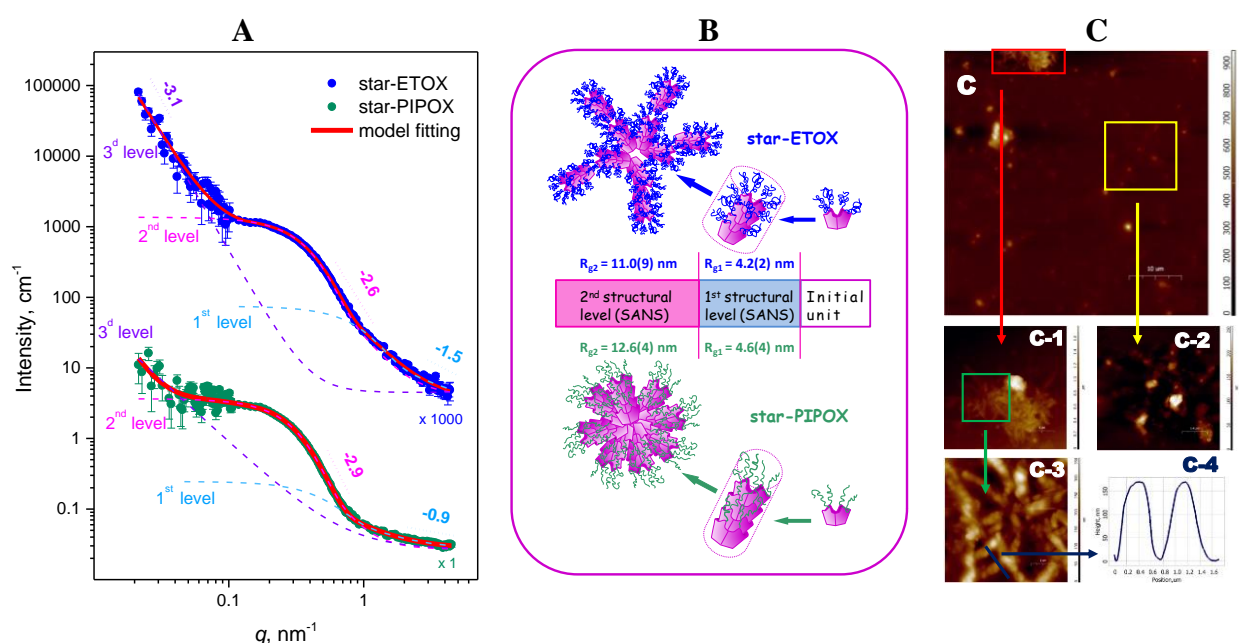


**Fig. 23.** Combination of USANS and SANS curves for star-PETOX (blue dots) and star-PIPOX (green dots) with approximations (red lines) obtained using a model developed by G. Beaucage (A); contribution from each structural level is shown by dashed lines; scheme of supramolecular organization for star-PETOX and star-PIPOX based on SANS analysis (B); AFM: star-PETOX agglomerates (C).

The location of n-decane molecules within the model biological membrane consisting of dioleoylphosphocholine (DOPC) bilayers was studied by small-angle neutron diffraction (SAND) and molecular dynamics (MD) [21]. Diffraction patterns of the samples containing different amounts of labeled and unlabeled n-decane were obtained at various H<sub>2</sub>O:D<sub>2</sub>O scattering contrasts and used to derive their neutron scattering length density (NSLD) profiles. The experimental data analysis based on the comparison of contrast varied NSLD profiles, revealed unambiguously the location of n-decane molecules in the complex liquid system. They are distributed mostly in the center of the lipid bilayer being oriented both perpendicularly to the lipid chains and parallel to the lipid chains. At the same time, the way of n-decane incorporation into the layer differs very little for the different concentrations studied (1:1 and 2:1 for n-

decane:DOPC molar ratios). The results of MD simulations (**Fig. 24**) qualitatively confirm the experimental observations and provide an explanation for the persistence of the n-decane incorporation mode. The work was performed in collaboration with Comenius University (Bratislava, Slovakia) and LRB JINR.

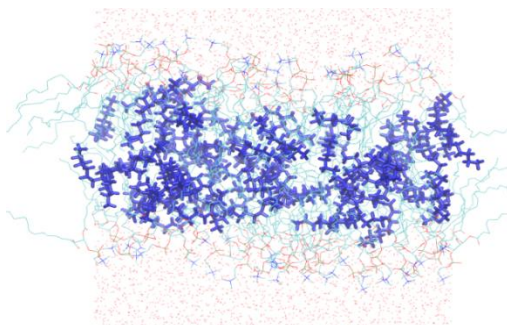


**Fig. 24.** Configuration of n-decane DOPC bilayers loaded for MD simulations.

Structural characteristics of nanocomposite series consisting of iron oxide nanoparticles embedded in the regular pores of amorphous silica matrix (SBA-15) were studied using small-angle neutron scattering (**Fig. 25**). Basing on the experimental data, a fundamental model describing the neutron scattering intensity distribution was proposed by assuming general composite structural features. The application of the model to SANS data confirmed the presence of iron oxide nanoparticles in the matrices under study, providing additional information on their shape, concentration, and size distribution [22].

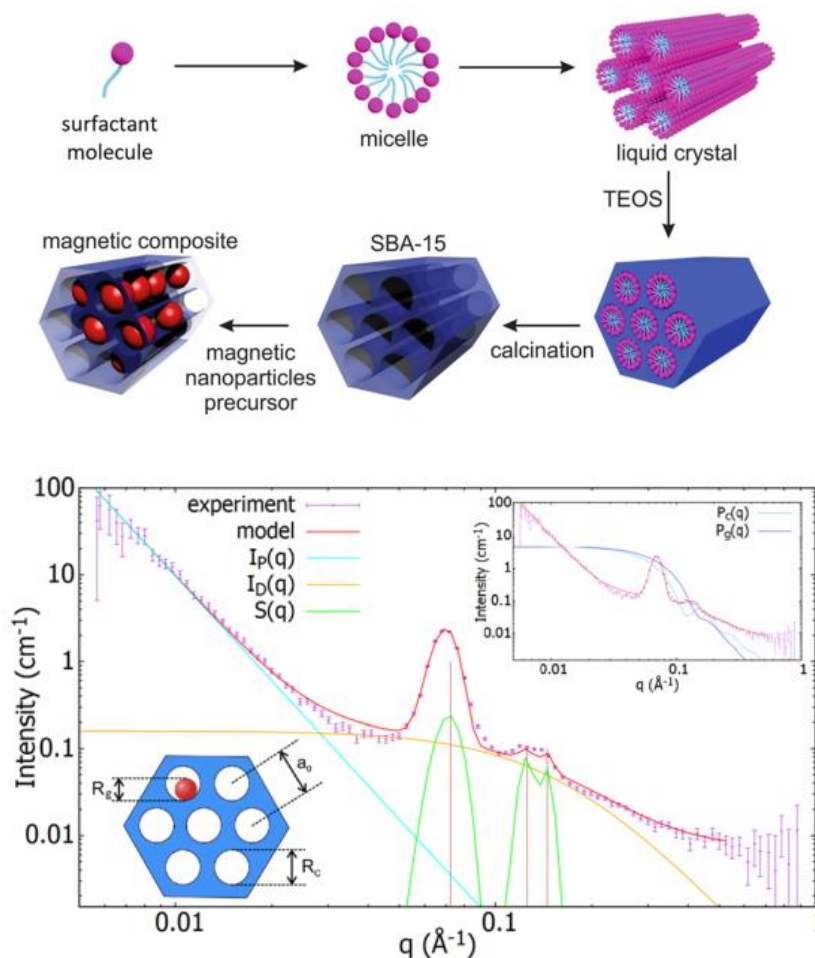


**Fig. 25.** Top: a hierarchical model of the structure organization of magnetic nanoparticles through micellar organization, liquid crystal, process of calcination and embedding. Bottom: small-angle scattering curves with diffraction peaks, fitting functions, and model structural diagram corresponding to the obtained experimental data.

Neutron reflectometry (specular reflection mode) was used (GRAINS reflectometer) in the structural studies of biorelevant solutions of current interest for medicines containing maltose (Phospholipovit). Using the contrast variation method for an aqueous solution of maltose at the interface with oxidized silicon, the scattering length density of the system was determined depending on the content of disaccharide. The results of the experiment were used for characterization of vesicular solutions of Phospholipovit using small-angle neutron scattering [23].

### 3.6. Investigations of polymer materials

The structural properties of HDPE+ZrO<sub>2</sub> polymer nanocomposite thin films with a thickness of 80-100 μm and a mass fraction of the filler of 1, 3, 5, 10, and 20% were studied by small-angle neutron scattering and Raman spectroscopy [24]. It was found that ZrO<sub>2</sub> nanoparticles do not change the basic crystal structure and chemical composition of HDPE, but the degree of crystallinity of the polymer decreases with increasing concentration of ZrO<sub>2</sub>. The results of SANS experiments (**Fig. 26**) showed that under ambient conditions ZrO<sub>2</sub> is distributed as monoparticles in the polymer matrix at all studied concentrations of the filler. At concentrations of 1-3%, the structure of HDPE+ZrO<sub>2</sub> does not change in the temperature range of up to 132°C, except for changes in the polymer structure at T > 82°C. At higher concentrations of the filler of 10–20%, the aggregation of ZrO<sub>2</sub> nanoparticles occurs with the formation of domains with a characteristic size of 2.5 μm. According to the data of Raman spectroscopy (**Fig. 26**), the formation of additional chemical bonds between the filler and the polymer matrix was not observed. The obtained results suggest that there is no core-shell structure in the polymer nanocomposite system under study.

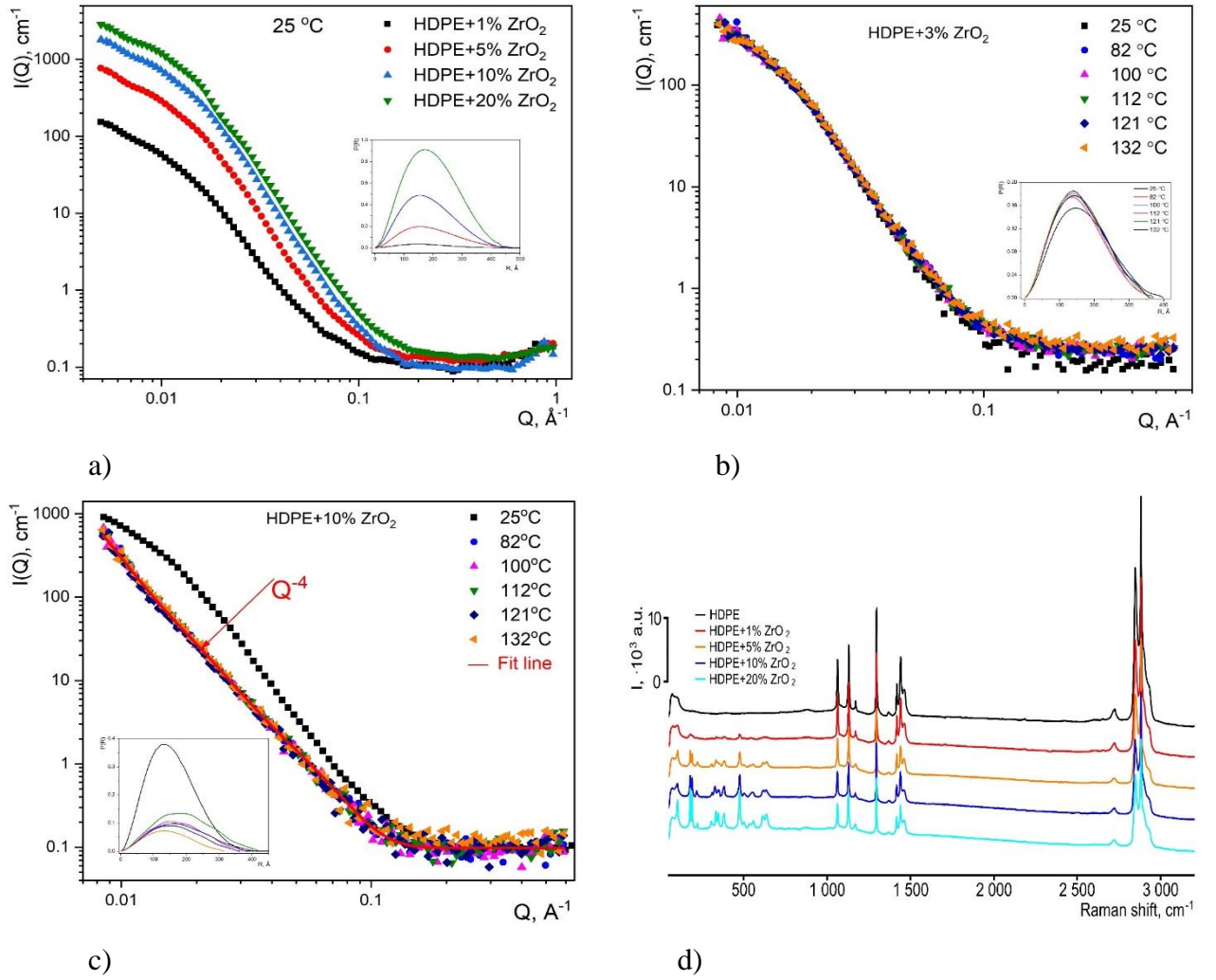


**Fig. 26.** Small-angle neutron scattering curves for HDPE+ZrO<sub>2</sub> polymer nanocomposite thin films at various ZrO<sub>2</sub> concentrations and temperatures (a-c). Raman spectra of HDPE+ZrO<sub>2</sub> system (d).

Work continued on the description of the glass transition kinetics of polymers (polystyrene) in a wide range of cooling rates [25, 26]. Two new measurements were considered: cooling rates in the range of 0.1 K/s - 5000 K/s at a heating rate of 5000 K/s and cooling rates in the range of 1-300000 K/s at a heating rate of 300000 K/s. It was previously shown that simultaneous simulation of the entire data spectrum with one set of parameters is impossible. Basing on this result, a simulation was performed with varying the parameters of nonlinearity  $x$  and non-exponentiality  $\beta$  for different cooling rates. It was shown that the range of the obtained values for these parameters does not correspond to the physical properties of polystyrene.

Model computations of isothermal glass transition of a glass-forming liquid with increasing pressure were performed. Basing on nonequilibrium thermodynamics, analytical expressions were obtained for the pressure dependence of the melting temperature:

$$\frac{T_m(p)}{T_m(p_m)} = \left\{ 1 + \frac{1}{\gamma_T} \left\{ \left[ 1 + \gamma_T \frac{p_m \Delta v_m}{\Delta h_m} \left( \frac{p}{p_m} - 1 \right) \times \left[ 1 - \frac{\gamma_p}{2} \left( \frac{p}{p_m} - 1 \right) \right] \right]^{1/2} - 1 \right\} \right\},$$

which directly affect the liquid-glass transition with increasing pressure due to changes in the relaxation time. The pressure dependence of the structural parameter at different rates of pressure change  $q_p$  as well as the dependence of pressure  $p_g$  (at which the liquid-glass transition occurs)

on  $q_p$ , are shown in **Fig. 27**. The work was carried out in collaboration with the University of Rostock (Rostock, Germany).

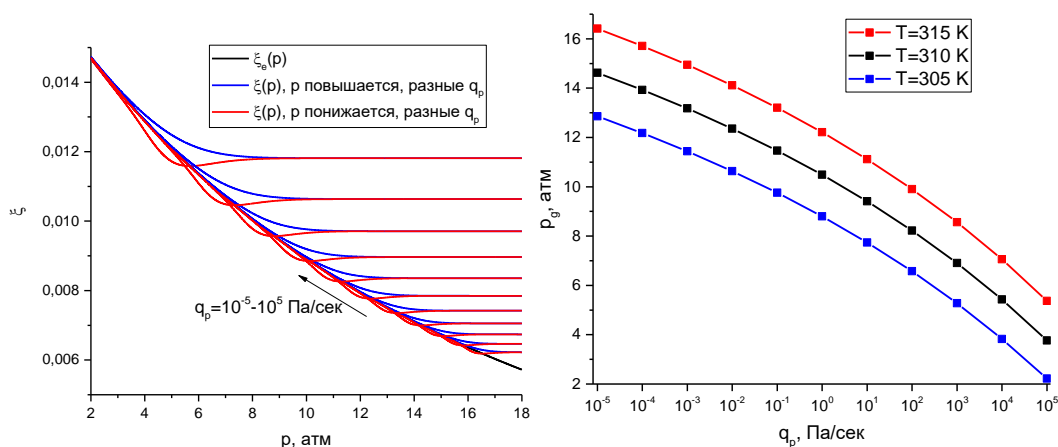


**Fig. 27.** (a) Pressure dependence of the structural parameter of the system,  $\xi = \xi(p)$ , during the liquid-glass transition for different values of the rate of pressure change in the range  $10^{-5} \leq |q_p| \leq 10^5$  Pa/s. Blue curves – pressure increase, red curves – pressure decrease. (b) Glass transition pressure  $p_g$  as a function of the rate of pressure change at the liquid-glass transition.

In the framework of research of application-oriented surfactant solutions, the effect of polymer polyethylene glycol (PEG) on the structure of aqueous surfactant micellar systems was studied [27]. The analysis of the small-angle neutron scattering data (YuMO spectrometer) provided the information on the structure and interaction parameters of micelles (micelle aggregation number, degree of ionization, anisotropy parameter, average diameter, charge, inverse screening length and surface potential) in solutions with and without the addition of the polymer. Using the concentration dependences of the experimental surface tension data, the parameters such as a critical micelle concentration, area per molecule, surface activity, surface excess and critical aggregation concentration were determined. Compared with surfactant solutions without polymers, the experimental surface tension curves for surfactant solutions with the addition of PEG have an additional break point (critical aggregation concentration), which corresponds to the initiation of the formation of the surfactant-polymer complex. The observed qualitative changes (**Fig. 28**) correspond to the specific interaction between anionic surfactants and the polymer. From a comparison with the previous experimental data, it was concluded that the molecular weight of the polymer significantly affects the structural properties of mixed solutions of surfactants and polyethylene glycol. The work was carried out in cooperation with the Faculty of Physics of Taras Shevchenko National University of Kyiv (Kyiv, Ukraine).

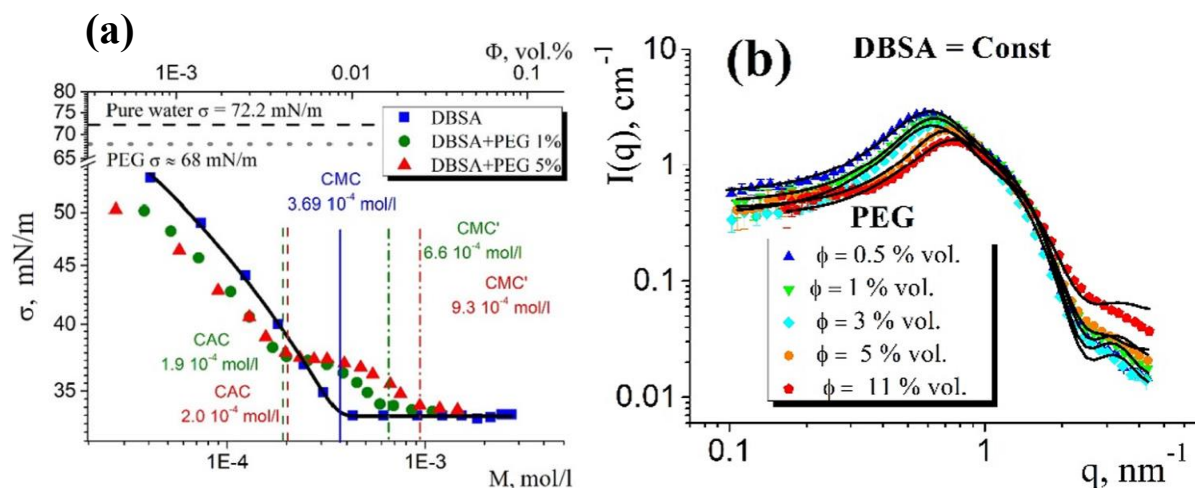


**Fig. 28.** Surface tension data for surfactant solutions with various concentrations of PEG (a). SANS data for a fixed concentration of surfactants and various concentrations of PEG (b).

The influence of the concentration of components in a tetraethyl orthosilicate (TEOS)–water–ethanol mixture on the growth of silicate aggregates in a basic environment (**Fig. 29**) was studied using small-angle neutron scattering [28]. A general tendency toward an increase in the size of aggregates was observed with an increase in the content of both water and TEOS. At the same time, when the H<sub>2</sub>O:TEOS molar ratio is 2:1, the structure of the aggregates repeats, regardless of the TEOS concentration in the system. The scattering length density of the aggregates was found via hydrogen/deuterium isotopic substitution and contrast variation to analyze the possible inclusion of residual ethyl and hydroxyl groups into their structure. The dependence of the structure of silicate aggregates in the tetraethyl orthosilicate–water–ethanol system on the synthesis parameters was studied using small-angle neutron scattering. It was shown that the aggregation process is critically dependent on the amount of water and TEOS in the system and that the most stable structural parameters relative to variations in the concentration of system components can be achieved by keeping the molar ratio of H<sub>2</sub>O:TEOS at 2:1. In addition, the experimental results on contrast variation refute the concept of “poisoned” bonds, which states that there are residual ethyl and hydroxyl groups in the aggregates.

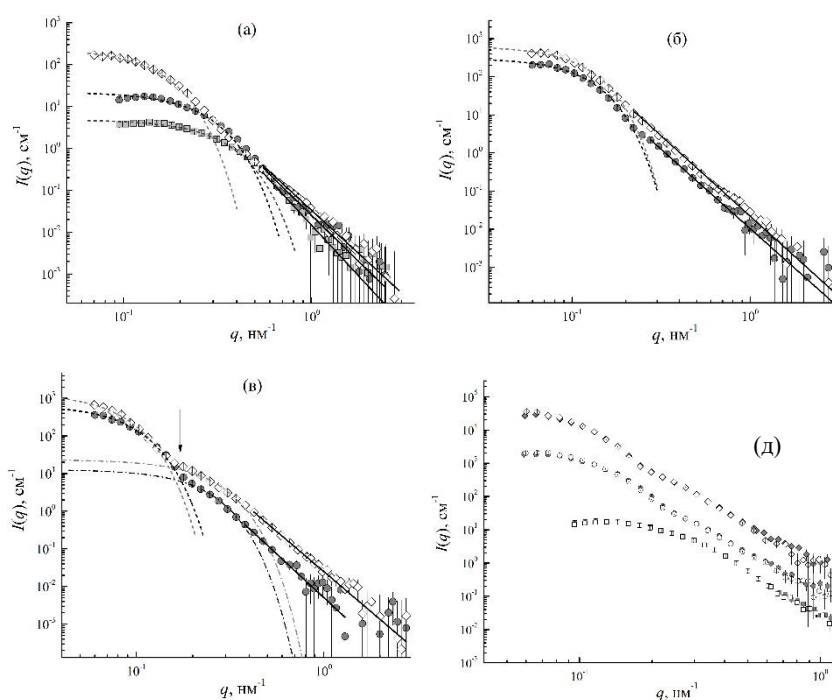


**Fig. 29.** Experimental SANS curves for three series of samples with different initial TEOS concentrations – 5 wt.% (squares), 10 wt.% (circles) and 20 wt.% (diamonds) corresponding to different molar ratios between water and TEOS  $w=1$  (a),  $w=2$  (b),  $w=10$  (c). Inner contrast variation in small-angle neutron scattering from silicate aggregates obtained via hydrolysis of TEOS in H<sub>2</sub>O/C<sub>2</sub>H<sub>5</sub>OH (empty symbols) and D<sub>2</sub>O/C<sub>2</sub>H<sub>5</sub>OH (filled symbols) basic solutions with different molar ratios between water and TEOS (d).

Work continued on the theoretical description of the glass transition kinetics of polystyrene in a wide range of cooling rates ( $5 \cdot 10^{-6}$  K/s –  $10^4$  K/s, three different heating modes). The behavior of excess heat capacity master curves in the given coordinates was found. To obtain these dependencies, the positions and the maximum value of each curve were determined. Using simulation, it was shown that this behavior closely corresponds to the glass transition kinetics in

the linear mode (weak dependence on the structural parameter). The results of these studies can be used to determine the deviation of the nonlinearity factor of glass transition,  $X$ , from unity. The dependence of the nonlinearity and nonexponentiality factors of glass transition,  $X$  and  $\beta$ , on the temperature and structural parameter was investigated as well. It was preliminarily shown that the linear dependences  $X$  and  $\beta$  are not sufficient to describe the experimental data in a wide range of cooling rates. The work was carried out in collaboration with the Institute of Physics, University of Rostock (Rostock, Germany).

### 3.7. Investigations of atomic and molecular dynamics

The effects of the crystalline electric field (CEF) in rare-earth dodecaborides  $R^{11}B_{12}$  ( $R = Tb, Dy, Ho, Er, Tm$ ) were studied by inelastic neutron scattering on the NERA and DIN-2PI spectrometers. The complementary possibilities of these spectrometers allowed us to reliably determine the parameters of the phenomenological model of the CEP potential. Examples of spectra showing excitation peaks associated with the CEF effects in the magnetically ordered state of the  $Ho^{11}B_{12}$  system at  $T = 3.5$  K are shown in **Fig. 30**. Measurements carried out on DIN-2PI with an initial energy of incident neutrons of 5 meV and energy resolution in the region of the elastic line of 0.23 meV made it possible to detect the triplet splitting of the ground state  $\Gamma_5^{(1)}$  in the internal molecular field. In the spectra measured on NERA in a wide range of transferred energies, two well-separated peaks corresponding to transitions between CEF levels were observed. Their energies and intensities were renormalized under the influence of a mean field associated with the presence of AFM ordering. The energy resolution of NERA in the elastic line region (0.9 meV) is insufficient for observing low-energy excitations associated with the splitting of the ground state. Consequently, the combination of experimental data measured on the two spectrometers was crucial for accurate determination of the parameters of the model. Calculations of the scattering law based on the phenomenological Hamiltonian of CEF and the mean molecular field provide a good description of the experimental spectra measured on both spectrometers.

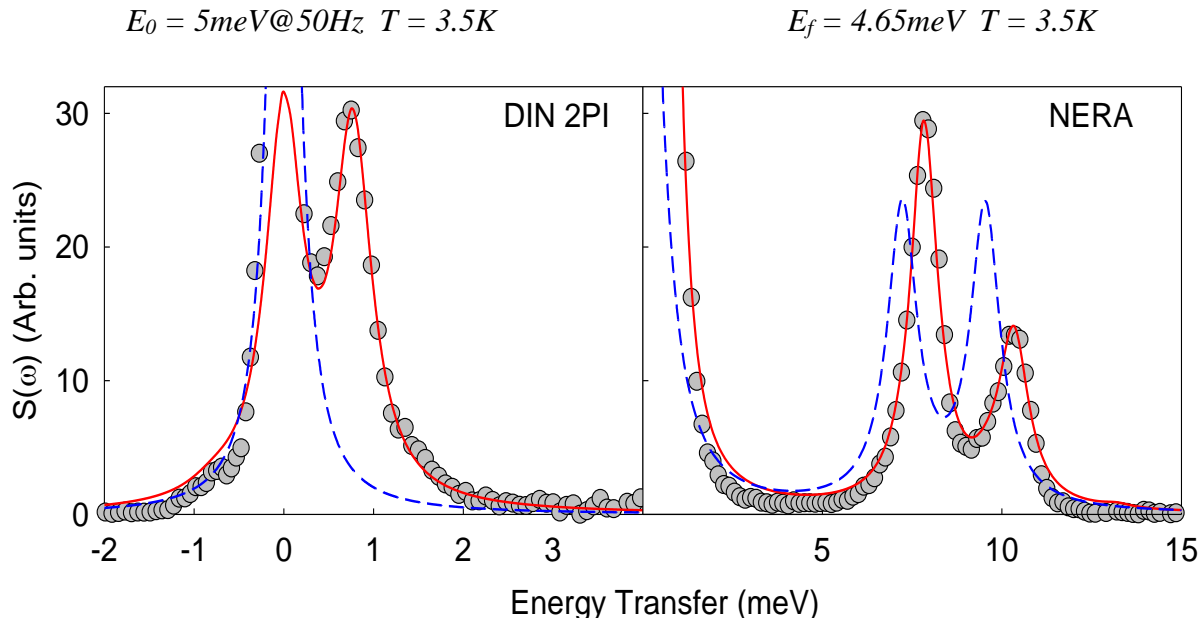


**Fig. 30.** Inelastic neutron scattering spectra for  $Ho^{11}B_{12}$  (grey circles) measured on DIN-2PI (initial energy  $E_0 = 5$  meV) and NERA (final energy  $E_f = 4.85$  meV) at  $T = 3.5$  K. The red line corresponds to the scattering law  $S(\omega)$  calculated in the model, which includes both the effects of the CEF and mean molecular field. The blue dashed line corresponds to the calculation taking into account only CEF effects without the influence of magnetic order.

The vibrational spectra of *Trans*-1,3-cyclohexanediol, *Cis*-1,3-cyclohexanediol, *Trans*-1,2-cyclohexanediol and *Cis*-1,2-cyclohexanediol compounds with a general chemical formula  $C_6H_{12}O_2$  were studied using inelastic incoherent neutron scattering on the NERA spectrometer (**Fig. 31**).

The presence of a plastic crystal phase was found only in *trans* isomers. An additional phonon density of states in the disordered glass phase was considered and a comparison with  $G(\nu)$  of rotational *I*-ordered crystal phases in these conformers was performed. At the temperature of liquid helium, the vibrational motions of protons involved in the formation of hydrogen bonds between molecules and molecular backbones were presumably observed. A comparison of the experimental data with the results of BDS and FT-IR studies and the results of studies for analogous compounds in the glassy state of the rotational phase and crystal phases is in progress. We expect to determine the effect of the  $\pi$ - $\pi$  interaction between neighboring molecules on the vibrational dynamics, as well as to analyze the effects associated with O-H ... O hydrogen bonds.

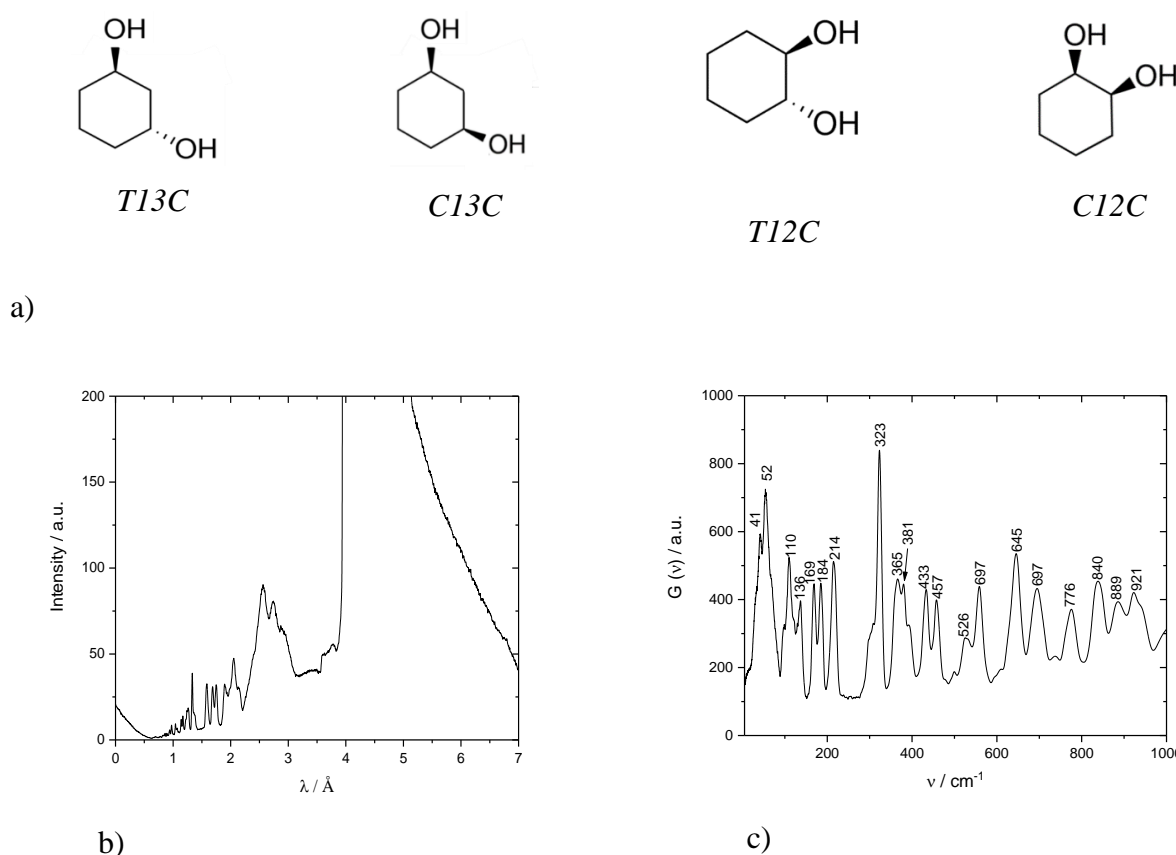


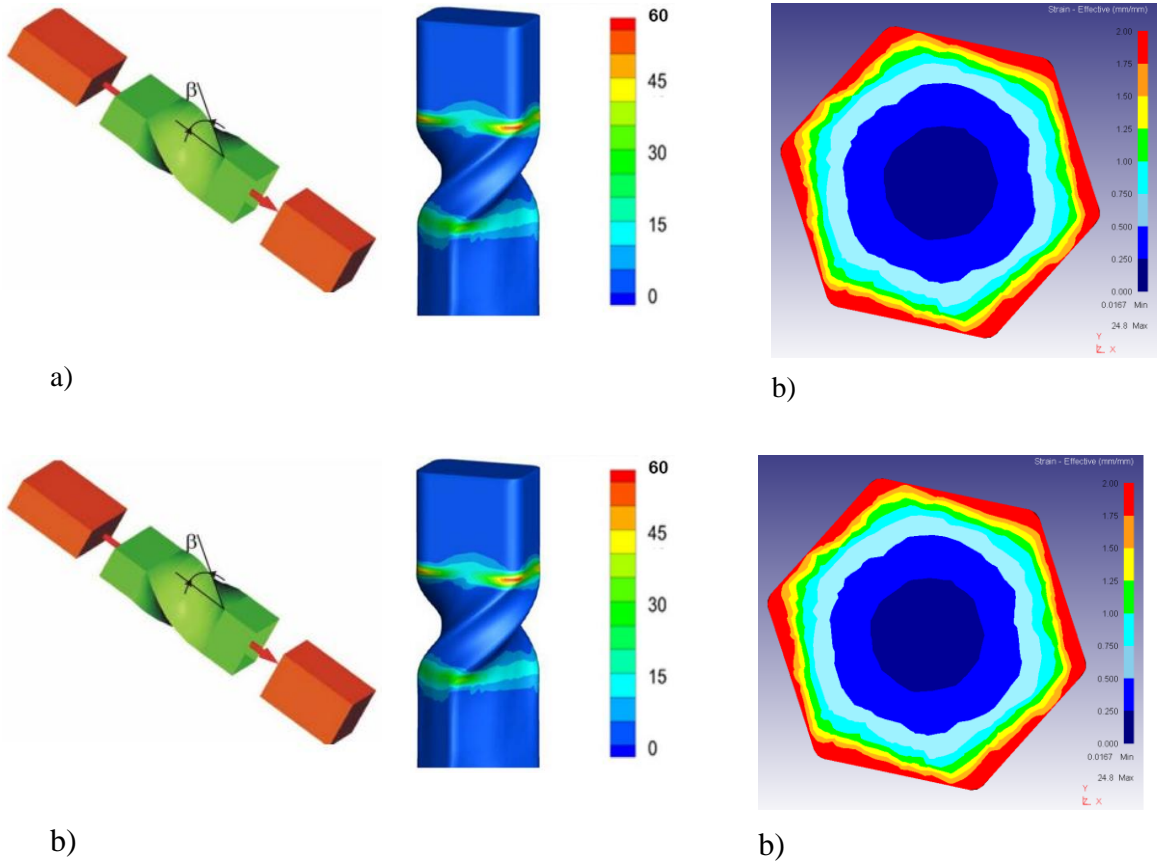
**Fig. 31.** Schematic representation of the molecular structure of the studied compounds (a). Inelastic incoherent neutron scattering spectra (b) and phonon density of states spectra (c) for *trans*-1,2-cyclohexanediol at 5 K.

### 3.8 Applied research

The mechanical properties and microstructure of a heterogeneous hybrid material, which is a composite of a soft coarse-grained (CG) core and a hard submicrocrystalline shell (SMC, size of the structural element of 0.1-1  $\mu\text{m}$ ) were studied. Such a composite structure is characterized by an increase in the uniform elongation parameter until the formation of a neck under tension (SMC materials are characterized by its small values), while maintaining high strength properties inherent to SMC metals. Such architectural materials can be used in the fields of industry where

rod-type products are in demand and weight reduction is critical while maintaining the strength properties of structural elements. Using computer simulation, we demonstrated the possibility of forming a coaxial two-component shell-core structure that combines regions with CG and SMC structures in metallic materials by the method of helical extrusion (HE) (**Fig. 32**). The HE process consists in forcing a prismatic workpiece through a matrix with a channel containing two prismatic sections separated by a screw-shaped section. The necessary conditions of the HE deformation processing were determined. The most significant of them are the geometric parameters of the helical matrices. These calculations were confirmed by the Vickers microhardness test along the diameter of a hexagonal workpiece, which showed the presence of a shell–core structure formed as a result of HE (**Fig. 32**).

To study the characteristics of the microstructure, mechanical residual deformations, as well as the crystallographic texture of the obtained material, a sample with a height  $H = 10\text{ mm}$  and diameter  $D = 41\text{ mm}$ , cut from a hexagonal workpiece after HE was applied for four times, was studied on the neutron Fourier stress-diffractometer FSD (**Fig. 32**). By scanning along the sample diameter and using a small scattering volume of  $2 \times 2 \times 7\text{ mm}$ , diffraction patterns were obtained at different values of the X-coordinate (scans along the lines L1 and L2, **Fig. 32**).



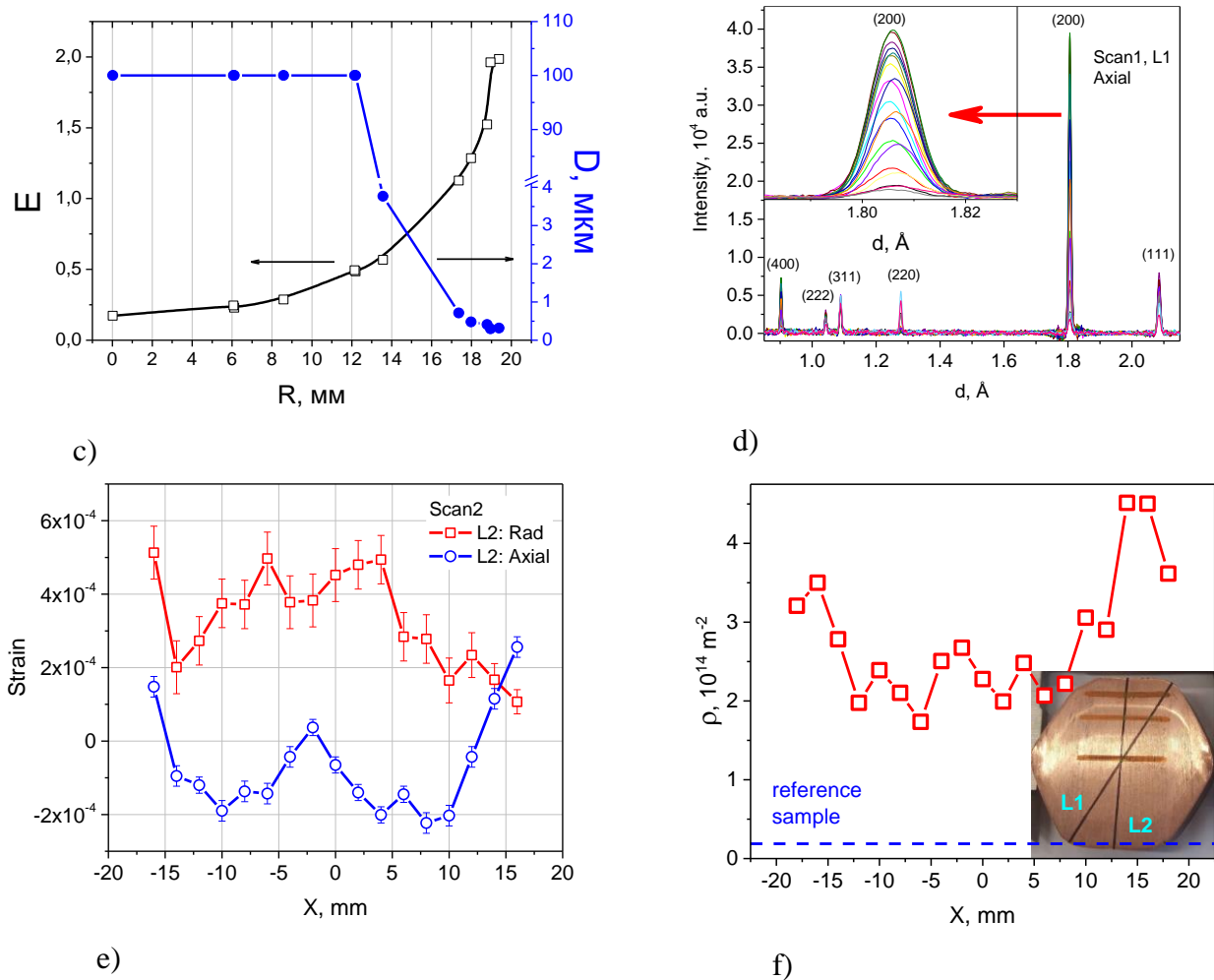


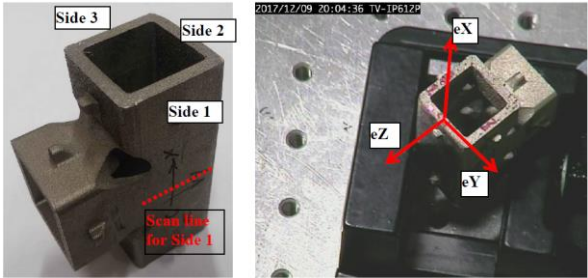
**Fig. 32.** a) Diagram of the helical extrusion process and the results of computer simulation of the deformation rate during HE in the deformed sample (after first application of HE). b) Map of Mises cumulative stress distribution over the sample cross-section. c) Results of computer simulation of the change in the accumulated stress and grain size along the sample radius (after first application of HE). d) Diffraction patterns obtained at various values of the X-coordinate along the sample diameter (scan along the L1 line). The inset shows the change in position and amplitude of the peak (200) as a function of the X coordinate. e) Radial and axial deformations of the copper crystal lattice as a function of the X-coordinate (scans along the L2 line). f) Dependence of the dislocation density in the sample on the X-coordinate in the direction from the center to the edge of the section (scan along the L1 line).

The analysis of the intensities of the diffraction peaks in the obtained spectra revealed the presence of a strong axial texture in the sample. The texture is the strongest in the center of the sample ( $X = 0$ ), as can be seen from the change in the intensities of the peaks (200) and (400) with the coordinate (**Fig. 32**). The study of the magnitude and character of the distribution of lattice deformations in the sample cross section made it possible to conclude that the level of residual stresses is low (does not exceed the conditional yield strength of the material, equal to 250 MPa in the initial state); residual stresses show a slightly pronounced gradient (**Fig. 32**). Also, from the broadening of the diffraction peaks, the dislocation density in the material under study was estimated (**Fig. 32**). The revealed gradient of the dislocation density in the direction from the center to the edge of the cross section confirms the presence of an internal architecture formed in the workpiece. The work was carried out in the framework of cooperation with the A.A.Galkin Donetsk Institute for Physics and Engineering, NAS of Ukraine.

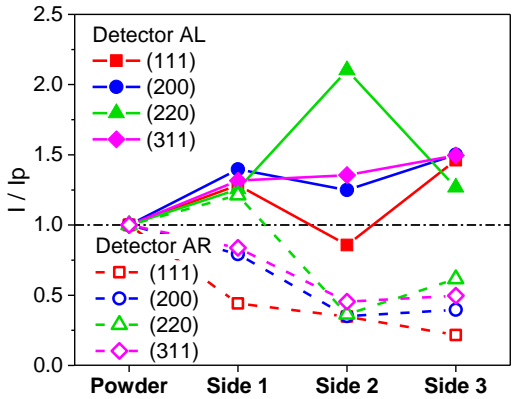
One of the promising methods of modern additive manufacturing (3D printing) is selective laser melting (SLM). The essence of the method consists in melting a fine powder material (most

often metal) with the help of a laser according to a previously created 3D model. The product is manufactured by sequential laser melting of thin layers of a powder material in the areas that coincide with the cross section of the 3D model, which allows one to produce constructions with a rather complex internal structure. A rather wide range of modern materials can be used as a powder material: polymers, ceramics, glass, metals (including steel and alloys), composite materials, etc. Due to a wide potential in practical applications of SLM-technology for manufacturing various industrial products the problem of the level of residual stresses and microstrains in these materials is of current interest. For this purpose, first experiments to study residual stresses and textures in a 3D sample made of powder of austenitic 304 steel by the SLM method (**Fig. 33**) were performed on the FSD diffractometer. The work was carried out in collaboration with the Institute of Electronics, BAS (Sofia, Bulgaria) and Technical University of Brandenburg (Cottbus, Germany).

The results of the experiments revealed the presence of a noticeable crystallographic texture in the material (**Fig. 33**) due to the recrystallization process upon cooling from the molten state. What is more, within the limits of one face of the sample, the texture practically did not change, but there was a strong difference in the ratio of intensities of the diffraction peaks (texture) between various faces of the product. The analysis of the peak widths from the material under study revealed no significant broadening of the diffraction lines in comparison with a standard sample, which points to a low dislocation density in the material and a large size of coherent scattering regions (crystallites). The level of residual stresses is relatively low and varies within  $\pm 200$  MPa, which does not exceed the yield strength of the material (**Fig. 33**). Along with it, one can observe both a stress gradient within one face of the sample and a noticeable difference in the level of stresses between the faces. Apparently, the main reason for this distribution of stresses is the choice of specific technological parameters of the process (laser speed, laser spot focusing, single layer thickness, etc.), as well as the non-equilibrium cooling of the product. In the future, it is planned to conduct experiments to study the mechanical characteristics of these materials under an external load in relation to various technological parameters of the SLM process.



a)



b)

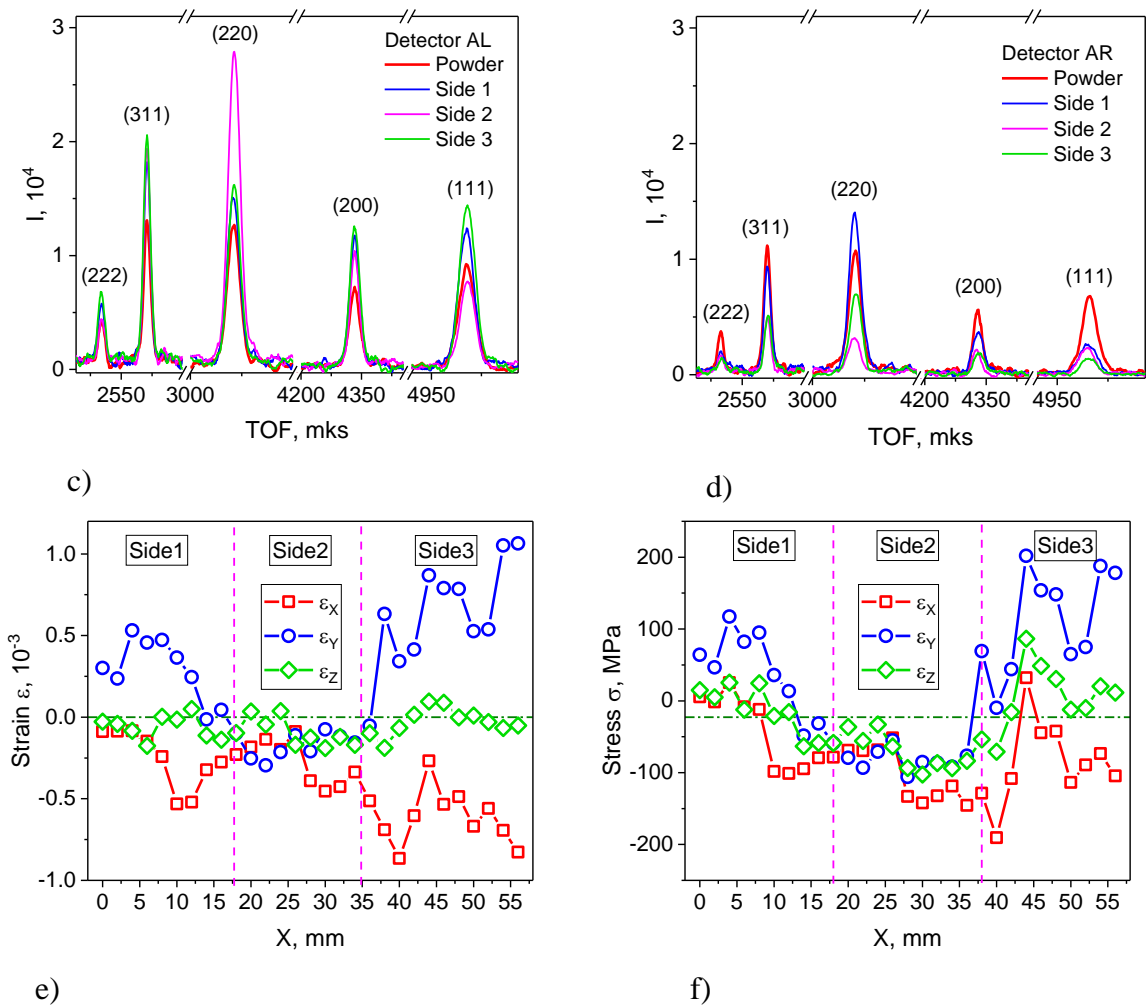


**Fig. 33.** a) Manufactured SLM sample. The measurements were carried out in the middle of the height of the sample on three faces (see the red dashed line of the scan). The right part shows the direction of the deformation components ( $\epsilon_x$ ,  $\epsilon_y$  and  $\epsilon_z$ ) of the sample mounted on FSD. b) Texture effects manifested in the relative intensities  $I/I_p$  of the diffraction peaks for different reflections ( $hkl$ ), where  $I_p$  is the corresponding peak intensity for a powder sample without texture. c), d) variation of peak amplitudes in the diffraction spectra measured on different faces of the sample in comparison with the powder sample and related to the texture effects. e), f) Residual deformations and stresses in the SLM sample measured on FSD.

In recent years, processes taking place in subduction zones have been the object of intensive research and discussion. There are a number of models on a tectonic scale, but information on deformation at the microscopic level is essential for an understanding of the processes involved. The study of the preferred crystallographic orientation of minerals in eclogites allows one to conclude about deformation processes in the crystalline part of the subducted oceanic lithosphere, as well as subducted continental units containing basic intrusions, which are frequently exhumed during continental collisions. The texture of omphacite, granite and other mineral constituents in eclogites was studied on the SKAT diffractometer [29]. The characteristic features of the pole figures (**Fig. 34**) made it possible to analyze the stress-strain states in the depth of the existing subduction zones, thermodynamic conditions (temperatures, pressures) and stress states in the process of exhumation of rocks.

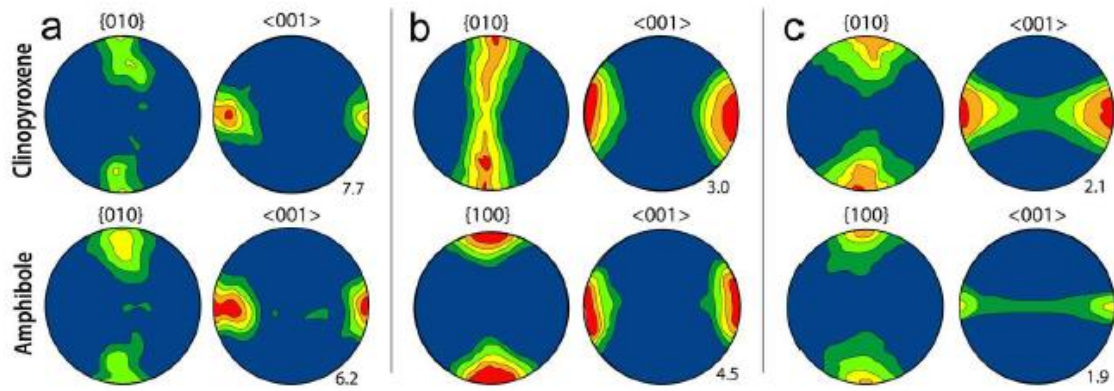
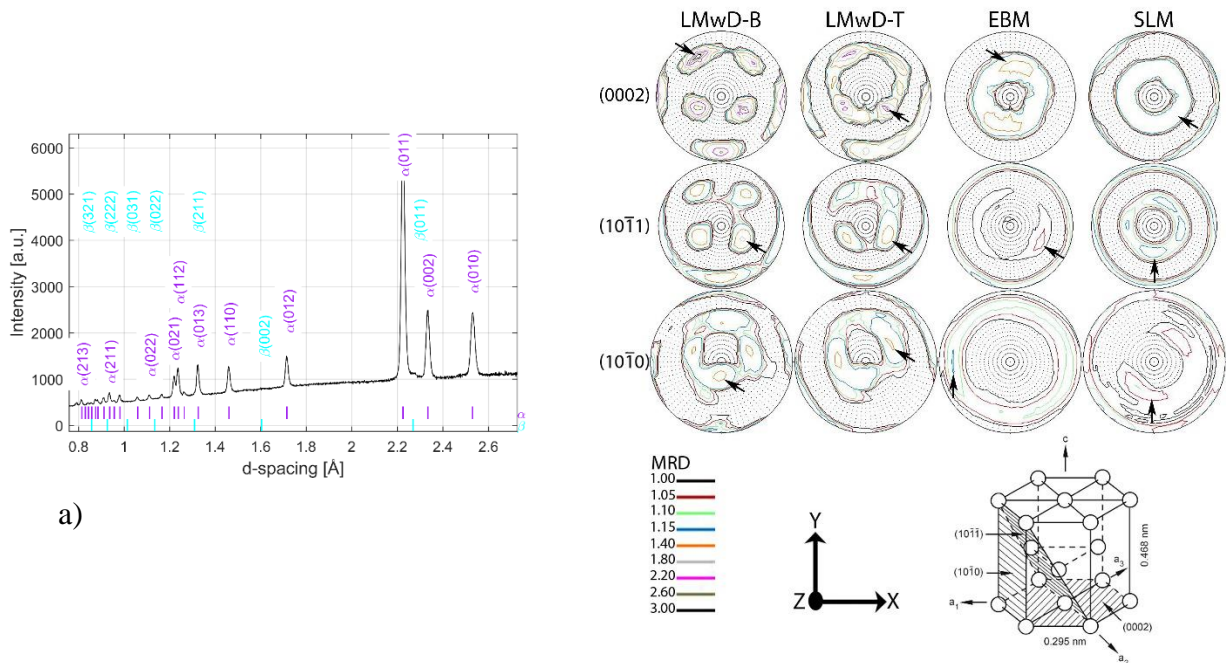


**Fig. 34.** a) Pole figures  $\langle 001 \rangle$  and  $\{010\}$  for clinopyroxene and amphibole (according to Heidelberg and Terry, 2013). Amphibole shows an unusual alignment of  $\{010\}$  with foliation normal. (b and c) Pole figures of retrogressive amphibole formed by dislocation creep at a later stage during exhumation independently from omphacite.

The variation of texture in Ti-6Al-4V samples produced by three different additive manufacturing processes (electron beam melting (EBM), selective laser melting (SLM) and laser metal wire deposition (LMwD)) was studied by neutron time-of-flight diffraction and back-scattering electron diffraction [30]. For an LMwD specimen, additional measurements of the top and bottom parts were also carried out to detect potential texture variations between areas close to and distant from the supporting substrate in the manufacturing process. It was found that the strongest texture is formed in the sample obtained by the LMwD process, and the textures of the samples obtained using the EBM and SLM processes are weaker and of the same order of magnitude, which is consistent with previous microstructural studies (**Fig. 35**). Texture variations were found in the LMwD sample, where the part closest to the substrate featured stronger texture than the corresponding top part. The crystal direction of the  $\alpha$  phase with the strongest texture component was  $[11\bar{2}3]$ .



b)

**Fig. 35.** a) A typical neutron diffraction pattern of an EBM Ti-6Al-4V sample. Estimated diffraction peak positions and Miller indices of  $\alpha$ -Ti and  $\beta$ -Ti phases are shown. b) Pole figures of  $\alpha$ -phase for four samples. The arrows indicate the areas with the highest intensity. The corresponding slip planes in the HCP structure are also shown.

The size, morphology, phase composition and volume fraction of dispersed precipitates in high-strength medium-carbon steel subjected to various tempering in the temperature range of up to 600°C were studied by small-angle neutron scattering, X-ray and neutron diffraction [31]. The combined use of complementary techniques made it possible to determine the kinetics of structural changes in the dispersed precipitates during tempering of steel. The increase in the tempering temperature up to 300°C results in a decrease in the amount of retained austenite. At the tempering temperature of 300°C the growth of Fe<sub>3</sub>C particles (instead of retained austenite) starts and continues up to 600°C. The phases of retained austenite and cementite were identified by neutron diffraction, while changes in sizes of dispersed particles of the phases were determined by small-angle neutron scattering. The results do not contradict the previously obtained transmission electron microscopy data. The comprehensive study carried out using the methods of diffraction and scattering of X-rays and neutrons made it possible to obtain sufficiently complete information about dispersed precipitates in steels.

The transformations of retained austenite during quenching and tempering of structural high-strength medium-carbon Cr-Ni-Mo-V steel (38XH3MFA) were investigated using X-ray phase analysis and neutron diffraction method [32]. The amount of retained austenite after quenching and quenching and high tempering (including double tempering) of products of small cross section (less than 25 mm) was determined. In the samples after quenching, the amount of retained austenite is ~3%, in the samples after quenching and high tempering it is less than 0.5%. The character of the distribution of retained austenite and morphology of martensite after quenching as well as quenching and high tempering were studied by transmission electron microscopy. The structure of the quenched steel is dominated by the martensite of the lath morphology, the amount of which is 90-95%, the amount of self-tempered martensite is small and amounts to 5-10%. The transformation of retained austenite during high tempering of steel was studied using a high-speed dilatometer. It was shown that in some cases retained austenite transforms into a mixture of carbides and  $\alpha$ -phase during heating for tempering, and in other samples from the same workpiece the transformation of retained austenite into secondary martensite occurs upon cooling from the tempering temperature. The double tempering has little effect on the amount of the retained austenite and on the level of dislocation density, contributing to a change in the shape of carbides from lamellar to globular and diminishing their dimensions.

A new method for quantitative analysis of retained austenite in textured steels using neutron diffraction was proposed. It is based on complete orientation averaging and calibration with reference samples for reliable evaluation of small austenite fractions, **Fig. 36** [33]. Unlike this method, conventional procedures ignore the effect of crystallographic texture and rely on a priori parameters. The new method allows one to determine the content of retained austenite down to 0.1 vol. %. The method was used to determine retained austenite fractions within 0.13-2.9% in samples of medium-carbon martensitic steel tempered at various temperatures.

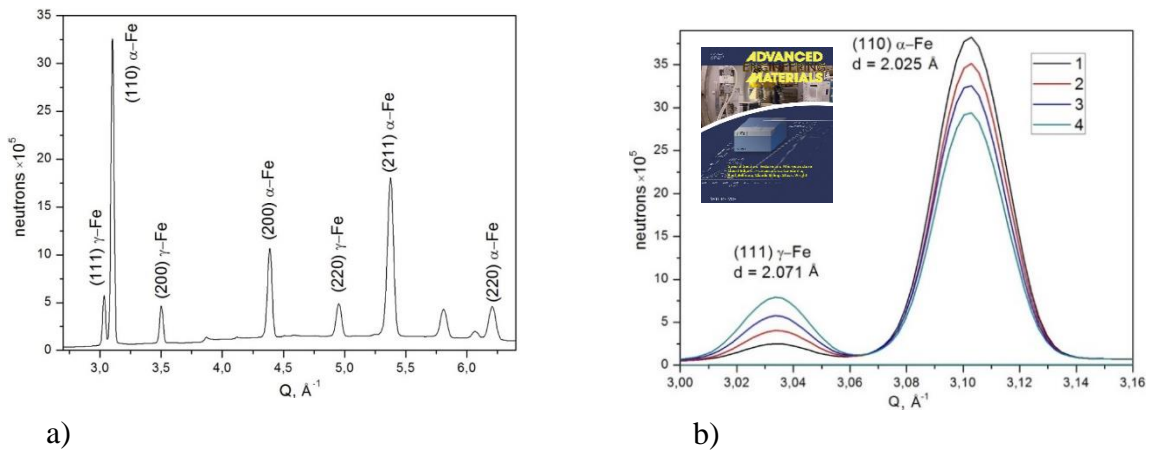


**Fig. 36.** a) Neutron diffraction pattern measured at SKAT diffractometer for a sandwich-like reference sample containing 10.58 wt. % of austenite. b) Neighboring diffraction peaks of  $\alpha$ - and  $\gamma$ -phases as obtained by the time-of-flight neutron diffraction technique on sandwich-like samples with different numbers of austenite ( $\gamma$ -Fe) parts placed on an Armco-iron ( $\alpha$ -Fe) substrate.

On the EPSILON diffractometer, the residual deformation of a sample of onyx from the Noyon Mountain (Mongolia) was studied by neutron diffraction [34]. The territory of the Noyon Mountain in southern Mongolia underwent strong tectonic disturbances in the Jurassic period and still is in the zone of active seismic activity. The residual strain was measured in six positions around the cylindrical axis of the sample with  $30^\circ$  increment. Five different planes of quartz crystallographic lattice ((10-10), (01-11), (11-20), (01-12), (11-21)) were analyzed. Almost sinusoidal behavior of the residual strain around the cylindrical axis of the sample in the radial direction was found.

On the spectrometer of neutron radiography and tomography, an ancient Slavic axe dating from the 10th century AD was examined. At present, the specialists of the Institute of Archeology of RAS are studying the manufacturing technology of this axe and determining the degree of deterioration of the object. This is connected with the clarification of the cultural origin of the axe: either the Norman group (Vikings) or the local, Old Russian origin. Neutron tomography showed the process of the distribution of defects in the depth of the axe, which is indicative of mechanical damage (**Fig. 37**).

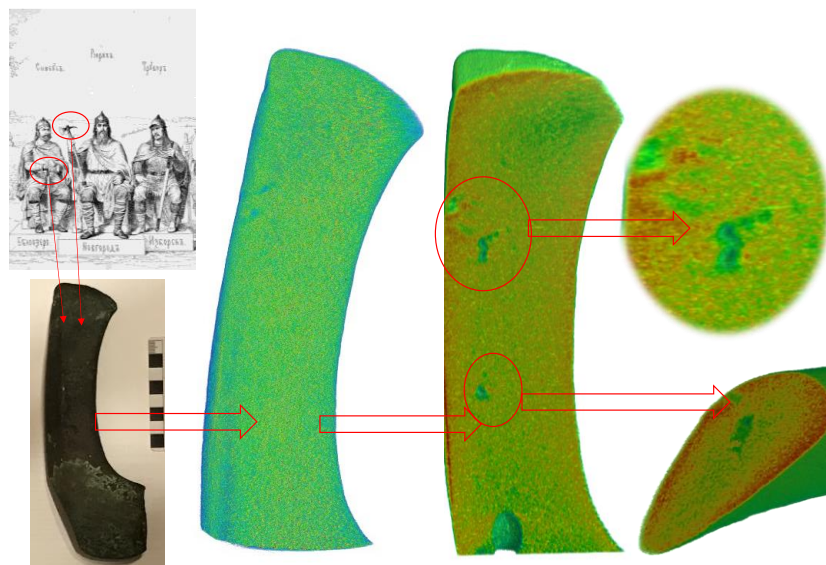
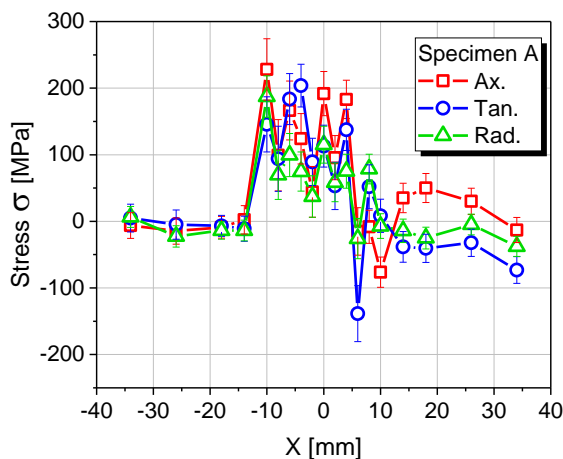


**Fig. 37.** Photo (left) and 3D reconstruction based on neutron tomography (right) of the old Slavic axe.

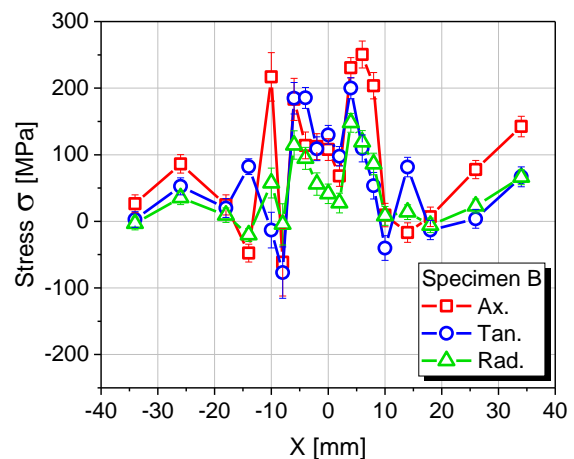
To study the effect of different heat treatment modes on the distribution of residual stresses and microstrains in welds, a series of cylindrical specimens (pipe segments) made of T24 steel was investigated using the FSD diffractometer. The study was carried out in cooperation with the Technical University of Ostrava (Czech Republic). T24 heat-resistant steel (7CrMoVTiB10-10) was developed in Germany for welding without heat treatment. Pipes made of this steel are often used for the construction of membrane walls of evaporators in boilers of modern thermal power plants. At the same time, the start-up procedures of many factory facilities were accompanied by the formation of cracks in homogeneous welded joints from T24 steel, which is associated with corrosion cracking due to internal stresses caused by the presence of atomic hydrogen that enters the molten metal and remains in it after solidification. To reduce the risk of cracking of T24 steel welds, special measures were developed and implemented, including annealing of boilers, etc.

In the experiments, scanning across the welds of specimens was performed over a wide range of X-coordinate using a small scattering volume of  $2 \times 2 \times 10 \text{ mm}^3$ , which was defined by radial collimators. The obtained experimental data of lattice parameters and diffraction peak width coefficients as a factor of interplanar spacing  $d_{hkl}$  were used to determine the components of the tensors of residual stresses and strains, as well as microstrains in the specimens under study in the weld area. The level of residual stresses in the studied specimens is quite moderate and reaches the maximum values in amplitude (in the range from  $-235$  to  $250 \text{ MPa}$ ) in the weld area and surrounding heat-affected zone (HAZ). This relatively low level of residual stresses can be explained by the correct selection of parameters for the welding process, in which the optimal amount of heat is transferred to the material, sufficient for welding the parts of the sample, but not causing strong stresses. It should be noted that the profile of the residual stress distribution along the X-direction is quite different for specimens with different heat treatments (**Fig. 38**).

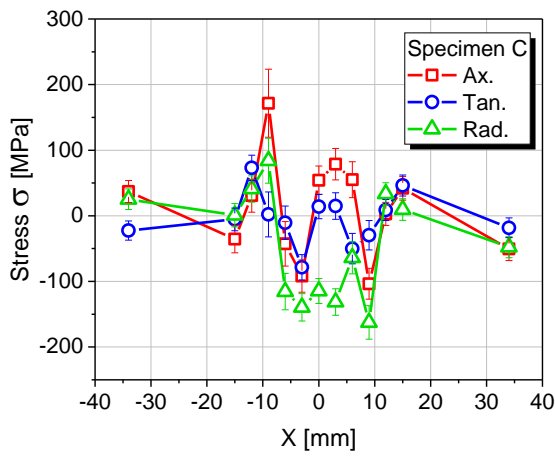
For specimens A, B, and C, the maximum level of dislocation density was observed in the HAZ regions, reaching significant values of  $1.9 \div 2.5 \cdot 10^{15} \text{ m}^{-2}$ , while a slight decrease (local minimum) in the dislocation density was observed in the very center of the weld (**Fig. 38**). It is noteworthy that for specimen D, as a result of post-weld heat treatment ( $740 \text{ }^\circ\text{C}/2 \text{ h}$ ), the dislocation density is decreased to very low values at the level of the base metal. A high level of dislocation density in the HAZ regions is also accompanied by a noticeable decrease in intensities and broadening of peak profiles. At the same time, the position of the maxima of the dislocation density coincides quite well with the dips in the peak intensity profiles. The former can be caused by the formation of a bainitic structure and the precipitation of phases of solid carbides and nitrides, which prevent the movement of dislocations. To clarify the composition and morphology of the secondary phases, it is planned to carry out a series of experiments on electron diffraction and transmission electron microscopy.



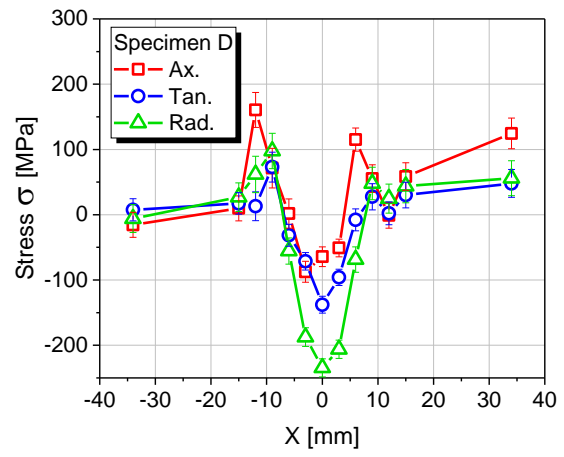
(a)



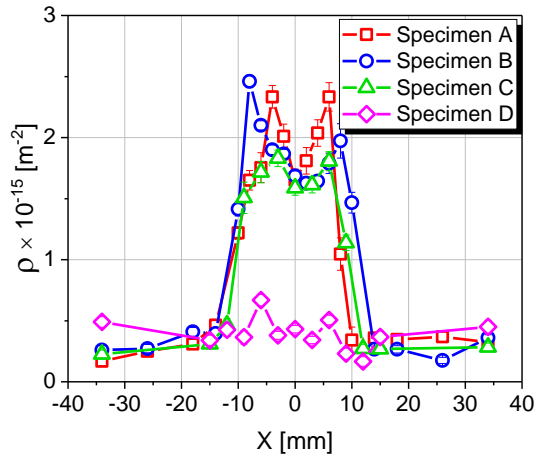
(b)



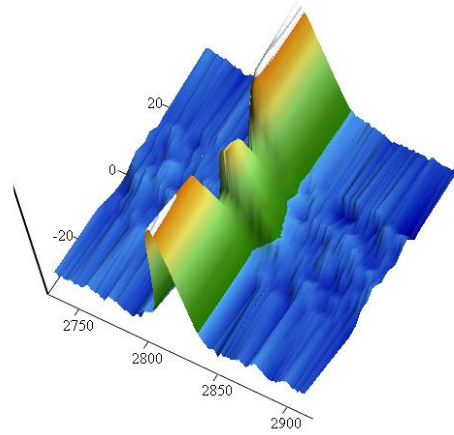
(c)



(d)



(e)



(f)

**Fig. 38.** Distributions of residual stresses obtained by scanning across the weld for a series of specimens of T24 heat-resistant steel with different heat treatment (a-d). Sample labeling: Specimen A – as welded; Specimen B – annealing at 450 °C / 48 h; Specimen C – annealing at 450 °C / 48 h + – annealing at 530 °C / 48 h; Specimen D: PWHT at 740 °C / 2 h. Dislocation density distributions obtained from diffraction data depending on the X coordinate for a series of T24 heat-resistant steel specimens with different heat treatments (e). Intensity map for diffraction peak (211) when scanning across the weld for Specimen C (f).

The first neutron experiments to study the evolution of the lattice deformation of AZ31 magnesium alloy at room temperature as a function of the applied load, as well as experiments to study the dependences of macroscopic deformation on the applied stress at room and elevated temperatures (150 °C) were performed at the FSD diffractometer. Cylindrical specimens were cut from a workpiece in longitudinal (RD) and transverse (TD) rolling directions of the initial material. Magnesium alloys belong to the group of lightweight structural materials and have unique properties such as high specific strength (yield strength-to-density ratio), excellent damping capacity and high thermal conductivity. These properties predetermine their wide industrial application, for example, in the automotive and aerospace industries. The main limitation for a wider use of magnesium alloys is their low ductility and poor formability at room temperature. The forming processes usually require different deformation paths, so it is very important to study the mechanical behavior of magnesium alloys, in which the deformation path changes at room temperature.

For the samples under study, different behavior of macroscopic deformation was observed at room and elevated temperatures. This behavior, apparently, results from the fact that plastic deformation occurs through the glide of dislocations and formation of twins, which are activated at elevated temperatures. During the neutron experiment, the samples of magnesium alloy AZ31 were subjected to uniaxial compression followed by uniaxial tension. Diffraction spectra were recorded simultaneously by two 90°-detectors for two directions of the scattering vector: parallel to the applied load (detector AL) and perpendicular to the applied load (detector AR). In addition, for the TD sample, the experiment was carried out for two orientations of the sample: the initial one (“Orientation 1”) and after the sample was rotated by 90° around the axial axis (“Orientation 2”). The experimental results showed that the diffraction patterns exhibit significant changes in the intensity of some reflections under loading, caused by the twinning process (**Fig. 39**). So, in the first part of the deformation path (compression), the twinning process was observed, which resulted in the appearance of (002) reflections, representing the orientation of extension twins. With a change in the deformation path to tension, the (002) reflection almost completely disappears, which is associated with the activation of the opposite process – detwinning. The lattice parameters  $a$  and  $c$  and microdeformation estimated from the broadening of diffraction peaks exhibit a similar rather complex deformation behavior for the specimens cut in the RD and TD directions (**Fig. 39**).

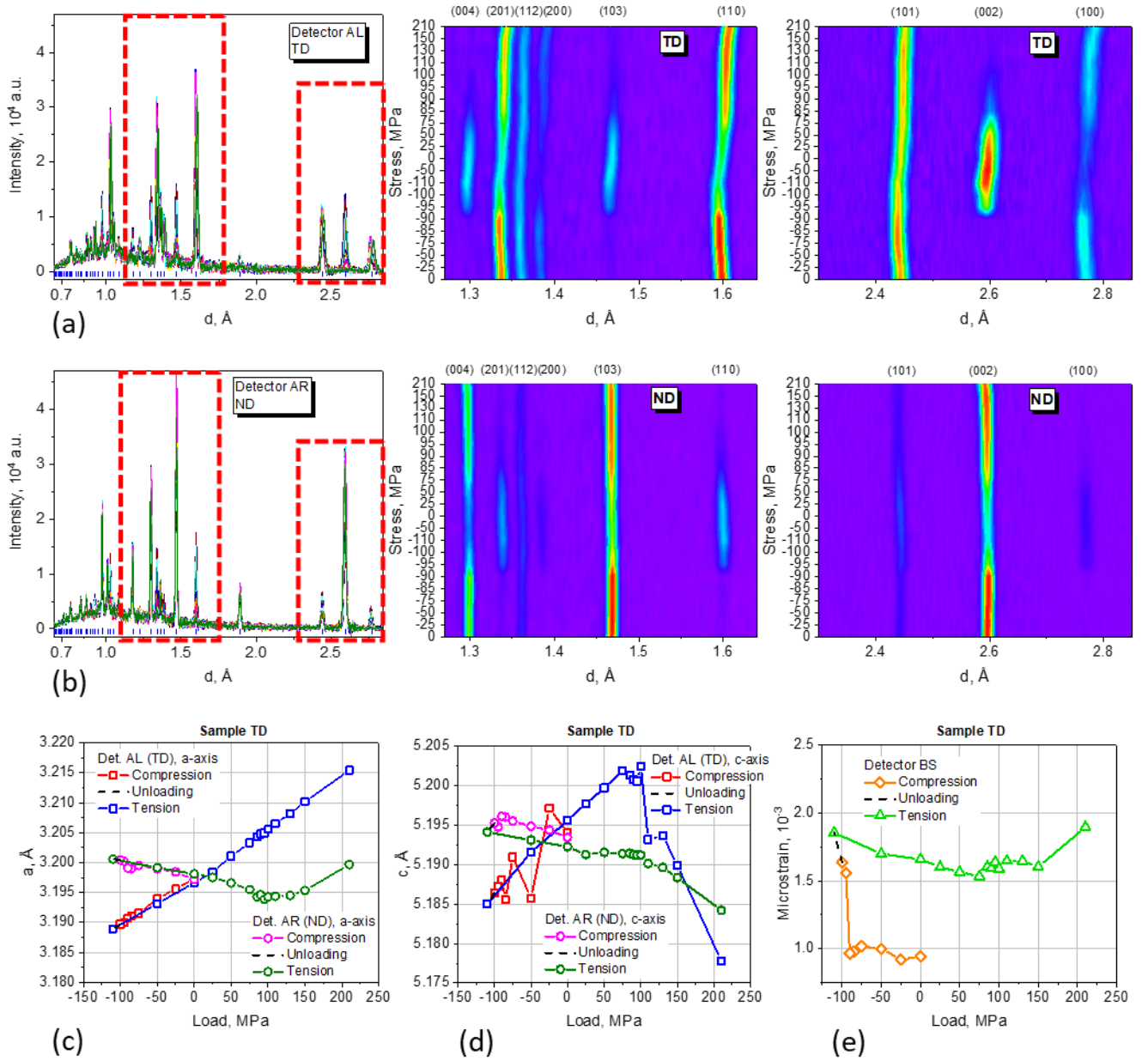


**Fig. 39.** Changes in the diffraction patterns and intensity maps (1.27-1.64 Å and 2.3-2.85 Å sections) as a function of the applied load for the TD sample, orientation 1, detector AL ( $\vec{Q} \parallel TD$ ) (a) and detector AR ( $\vec{Q} \parallel ND$ ) (b). Crystal lattice parameters  $a$  (c) and  $c$  (d), averaged microdeformation estimated from the broadening of diffraction peaks (e).

On the Epsilon and FSD diffractometers, the studies of internal stresses and strains in Al/SiC<sub>p</sub> composites were performed *in situ* during a tensile test up to sample fracture (**Fig. 40**). The experimental results were compared with the calculations in the framework of the elastic-plastic self-consistent model. It was found that phase stresses of thermal origin relax at the beginning of plastic deformation of Al/SiC<sub>p</sub> composite. The evolution of lattice strains can be correctly described using the elastic-plastic self-consistent model, taking into account the relaxation of initial stresses. A major role in the strengthening of the studied composites is played by the transfer of stresses to the SiC<sub>p</sub> phase, as well as the hardness of the Al matrix [35].

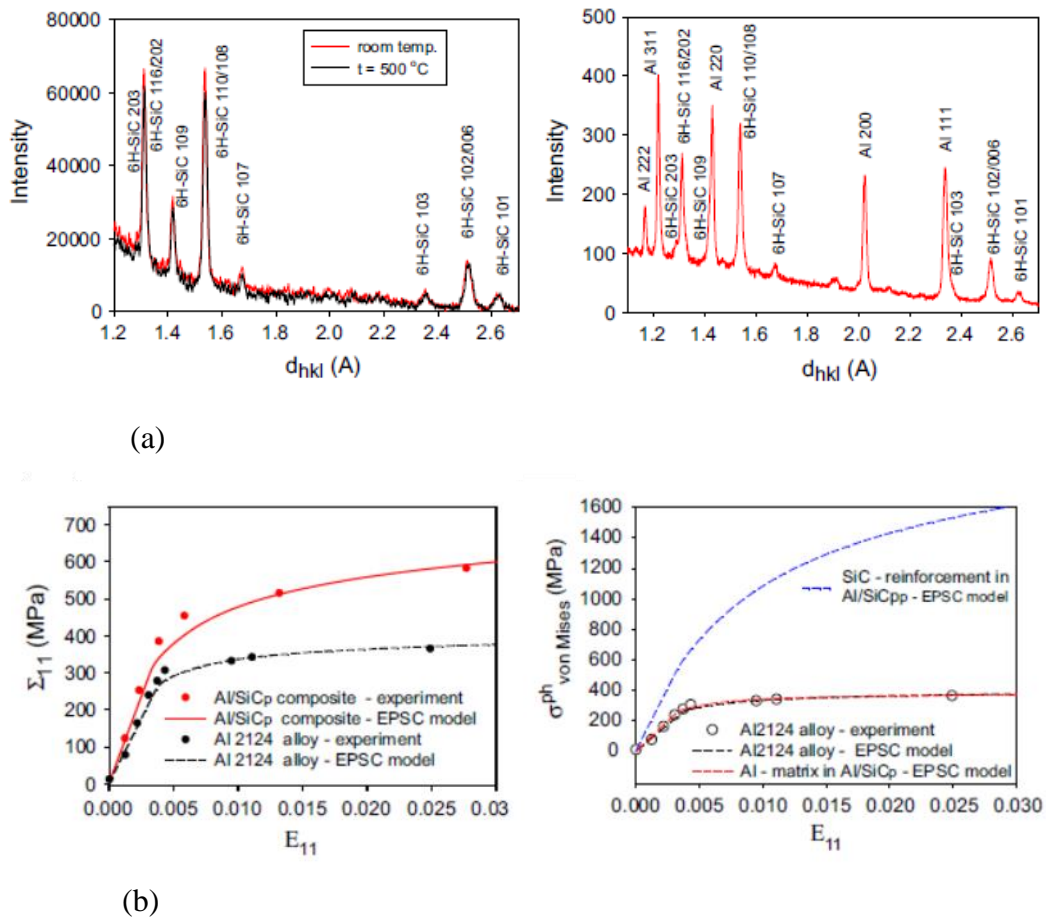


**Fig. 40.** Neutron diffraction patterns of SiC powder at two temperatures, obtained using the FSD diffractometer and of Al/SiC<sub>p</sub> composite at room temperature, measured with the Epsilon diffractometer (a). Experimental and calculated dependences of the total stress and von Mises stress on strain (b).

Also, the evolution of stresses in both phases of Al/SiC<sub>p</sub> composite subjected to thermal cycling during *in situ* compression test was studied using the Epsilon diffractometer. It was confirmed that interphase stresses can be caused by the difference in the thermal expansion coefficients of the reinforcement and the matrix, which leads to different behavior of phase volumes during heating or cooling. It was shown that the experimental results can be described using the thermomechanical self-consistent model. Also, a study of elastic-plastic deformation was carried out, which made it possible to analyze the evolution of the total stress tensor in both phases of the composite and consider its decomposition into deviatoric and hydrostatic components. Using a new thermomechanical self-consistent model, it was shown that the strengthening of Al/SiC<sub>p</sub> composites is caused by the stress transfer from the plastically deformed Al2124 matrix to the elastic SiC<sub>p</sub> reinforcement, while thermal stress relaxation does not significantly affect the general properties of the composite [36].

Biomineral composites, among which are mollusk shells, are promising prototypes for the development of new lightweight materials with improved mechanical properties and environmentally friendly characteristics. The investigation of the global crystallographic texture and phase composition of bivalve mollusk shells was carried out with the SKAT diffractometer [37]. It was found that the shells of mollusk species of the genus *Mytilus* consist of two phases – calcite and aragonite. The texture of the calcite phase is very sharp for mollusks of the species *Mytilus galloprovincialis*, *Mytilus trossulus*, *Mytilus edulis*. The crystallographic texture of bivalve shells has a different character for different phases (calcite, aragonite), **Fig. 41**. The texture and phase composition of *Ostrea edulis* and *Mya arenaria* shells were studied as well. It

was found that the shells of *Ostrea edulis* consist mainly of calcite, whereas *Mya arenaria* shells consist of aragonite. Measurements of the texture of other *Mytilus* shell samples show good reproducibility of the results. The crystallographic texture may be a new feature for the classification of bivalve mollusks. In addition, its changes over time can help in understanding the processes of fossilization in mineral skeletons. Therefore, studies were carried out on the texture of bivalve mollusks belonging to other genera in the *Mytilus* family, as well as of fossil shells. Studies of the texture of shells of freshwater mollusks were started to investigate the effect of habitat conditions on the formation of preferred orientations in shells.

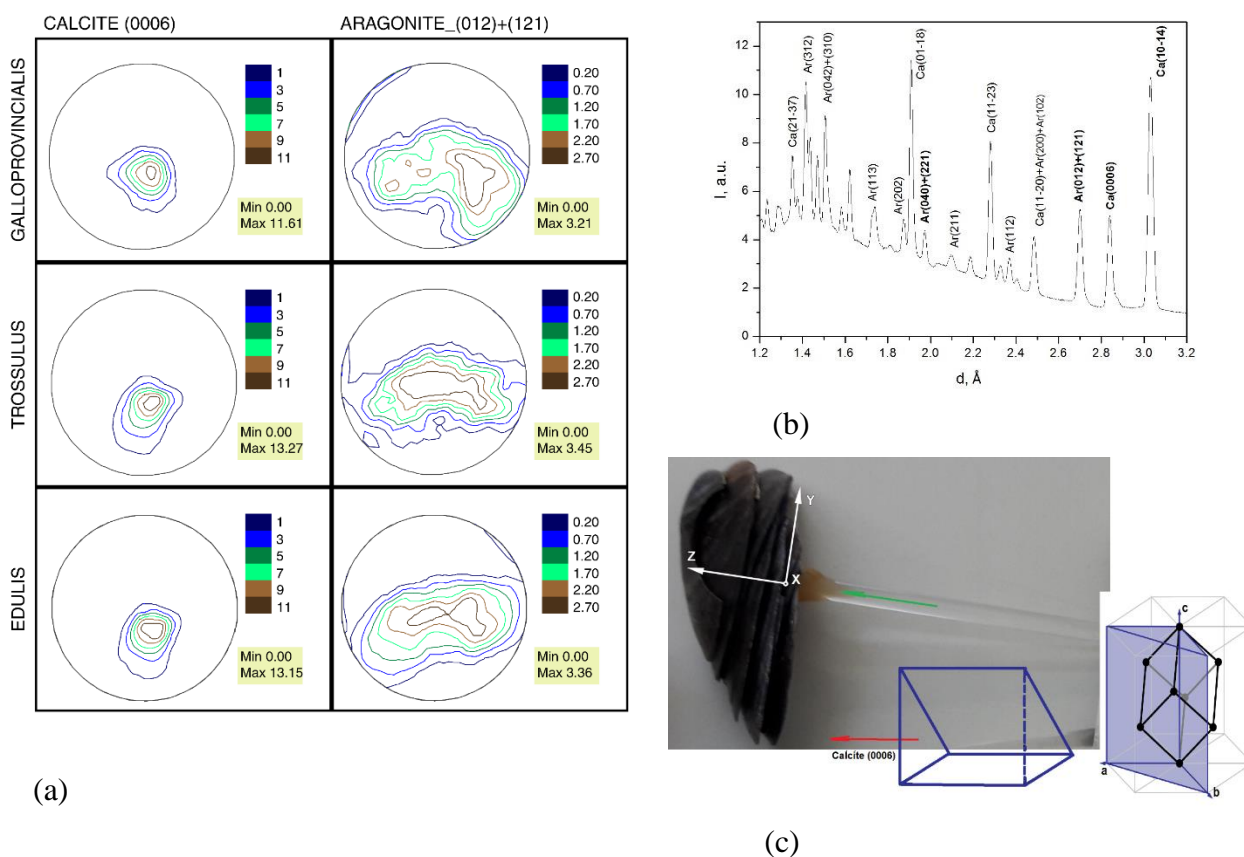


**Fig. 41.** Pole figures for shells of various species of mollusks *Mytilus* (a). An example of neutron diffraction pattern for *Mytilus edulis* shells (b). An explanation for the maxima in the pole figure (006) for the

Studies of aging processes in concrete samples intended for long-term storage of radioactive aluminum waste were carried out. Such concrete should have stable mechanical, physical and chemical properties. A comparison of the spectra obtained at intervals of one and two years for samples of different chemical compositions was performed. The measurements were carried out under the same conditions. It was revealed that for one of the samples during measurements after one year, the background increased sharply, which is probably due to the continuation of reactions accompanied by the release of hydrogen. A year later, this process stopped. For other samples, this process was not observed. However, crystallization continues in all samples two and three years after fabrication, since an increase in diffraction reflexes can be observed. This can lead to an increase in the anisotropy of physical properties over time. It was shown that among the studied samples based on the CEM III matrix, the sample without  $\text{LiNO}_3$  has the highest structural stability three years after fabrication [38].

A study of sandstone samples subjected to axial stress, confining pressure and pore pressure was performed on the Epsilon diffractometer using a triaxial compression chamber (Fig. 42). The purpose of the experiments was the identification of the features of deformation

mechanisms in rock samples under external and internal loads, which are used as reservoirs in studies of geothermal energy.

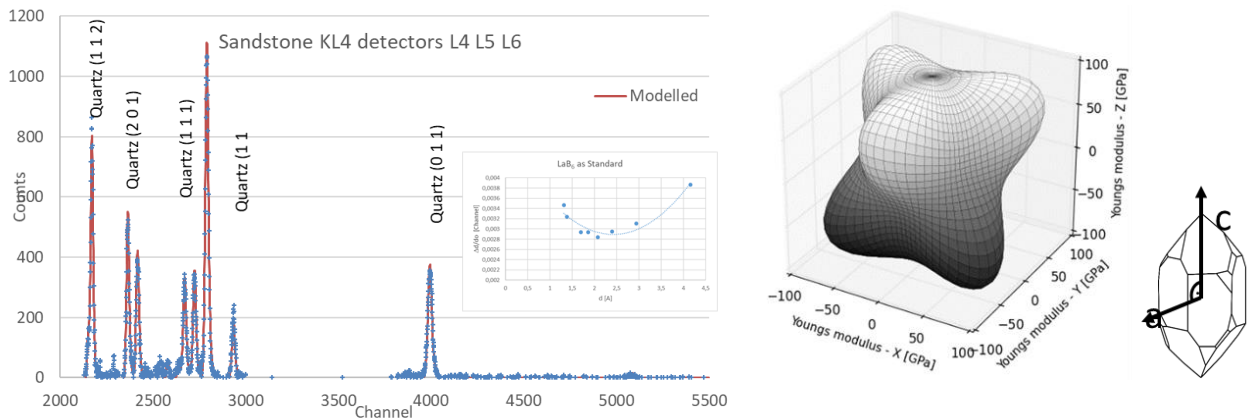
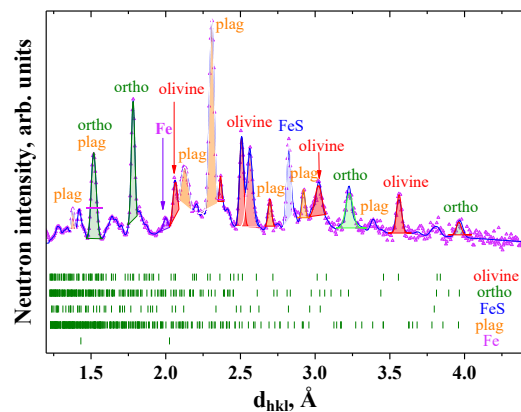


**Fig. 42.** Neutron diffraction spectrum of a sandstone sample obtained using a triaxial compression chamber during *in situ* experiments on the Epsilon diffractometer (left). Calculated Young's pseudo-module of quartz mineral (right).

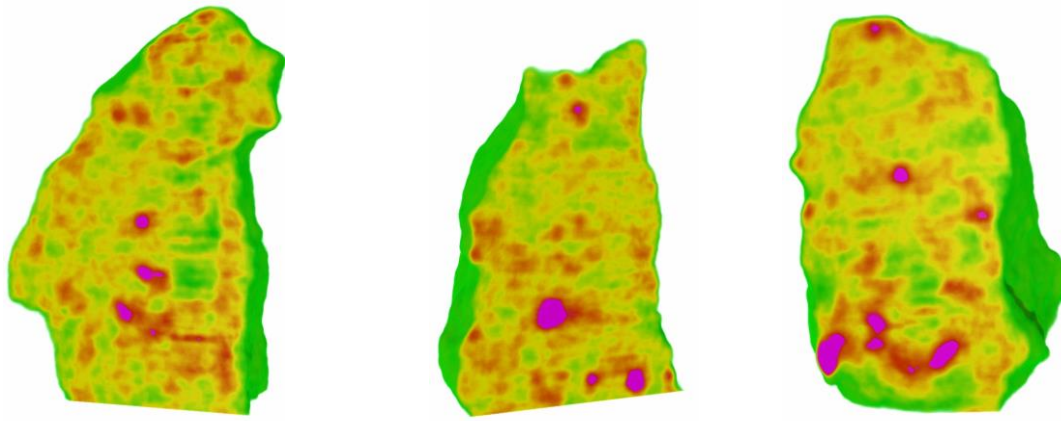
The internal structural organization and phase composition of a fragment of the Chelyabinsk meteorite were studied using neutron diffraction, tomography methods, optical microscopy, and Raman spectroscopy [39]. The bulk mineral composition of the meteorite and spatial distribution of different components were determined (**Fig. 43**). In addition to the previously found phases of olivine, orthopyroxene, plagioclase and troilite, the obtained data of optical microscopy and neutron diffraction provide evidence of the presence of the kamacite (FeNi) phase in the studied meteorite fragment. A heterogeneous distribution of iron in the olivine and orthopyroxene phases was observed, and morphological calculations were made to analyze the spatial arrangement of metal components.



(a)



(b)



(c)

**Fig. 43.** Photo of the studied fragment of the Chelyabinsk meteorite (a). Neutron diffraction pattern of the fragment, obtained using the DN-12 diffractometer and refined by the profile matching method (b). Fragments of the 3D model of the internal organization of the studied fragment obtained using neutron tomography. The pink areas correspond to metal grains (c).

#### 4. Instrument development

The head part — the splitter of channel 10 of the IBR-2 reactor with the operating GRAINS reflectometer (beamline 10b) — was upgraded to improve the characteristics of two (10a, 10b) beamlines. The old head part was dismantled. A new beam splitter with two double-disk background choppers (MIRROTRON, Hungary) was installed (**Fig. 44**). Beamline 10a, earlier equipped with a beam bender, was optimized for the future installation of a combined small-angle scattering/imaging setup.



**Fig. 44.** A new head part of channel 10 in the ring corridor of the IBR-2 reactor, consisting of two neutron guides and double-disk background choppers installed in the corresponding technological gaps.

In the framework of the project "A system for neutron *operando* monitoring and diagnostics of materials and interfaces for electrochemical energy storage devices at the IBR-2 reactor" (ELCHEM\_NS), the electrochemical cell for neutron reflectometry experiments was upgraded and improved. The new design of the cell (**Fig. 45**) in the "beam from bottom"

configuration provides better control of the cell filling with liquid electrolytes. The modification of the cell allowed us to significantly reduce the consumption of expensive deuterated electrolytes in experiments, and also made it possible to conduct contrast variation experiments with higher accuracy due to better control of the ratio between light and heavy components in electrolytes.

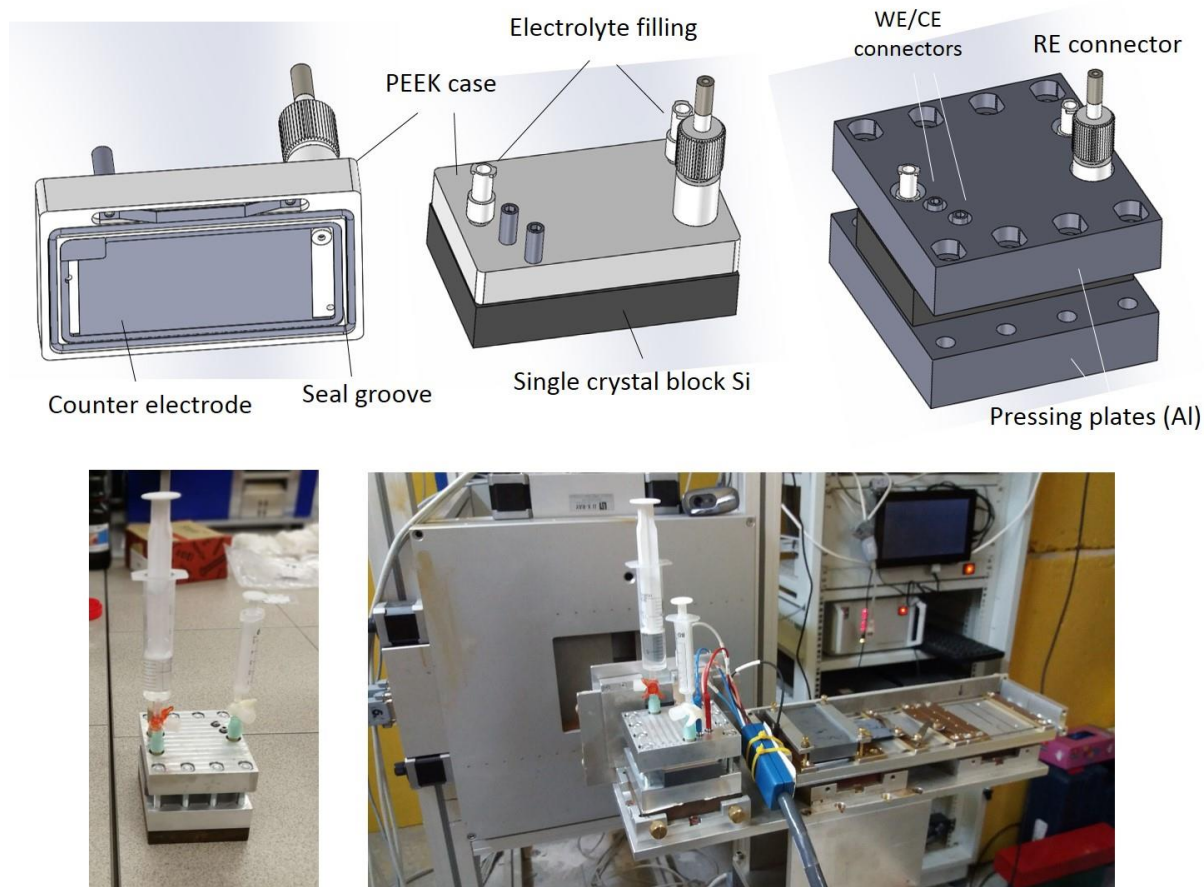


**Fig. 45.** Design of the electrochemical cell for neutron reflectometry and its assembly and installation for the experiment at the GRAINS reflectometer.

On the GRAINS reflectometer, the shielding of beamline 10 in the IBR-2 experimental hall was reconstructed; as a result the sample environment room was enlarged. In cooperation with the SC Department, the data acquisition and storage systems for 2D position-sensitive detectors were tested. Three types of the systems were used: two data acquisition systems produced in FLNP and a commercial analog-to-digital converter that was adjusted in FLNP to work with the PSD detector. For all systems, parameter ranges of correct operation were determined. The sources of errors reducing the operating ranges were found.

The possibilities of optimizing the initial structure of the solid-liquid interface in *in situ* experiments on neutron reflectometry with the aim of maximizing weak changes in the specular reflectivity curves following small changes at the interface, were considered [40, 41]. The interface is modeled as a carrier layer on a substrate, which is in contact with the solution and where an adsorption layer (thickness of up to 2000 Å) is deposited from the solution in time. The proposed optimization procedure was considered for the initial configuration of the electrochemical interface, where, when an electrical circuit is closed, from a liquid electrolyte with lithium ions an adsorption of transitional layer (known as solid electrolyte interphase) is

deposited on a metal electrode on a silicon substrate (**Fig. 46**). The study of this system allows one to introduce restrictions on the variation of parameters of the interface, which significantly simplifies the solution of the optimization problem. The work was carried out in collaboration with the Physics Department of the Taras Shevchenko National University of Kyiv (Kiev, Ukraine).

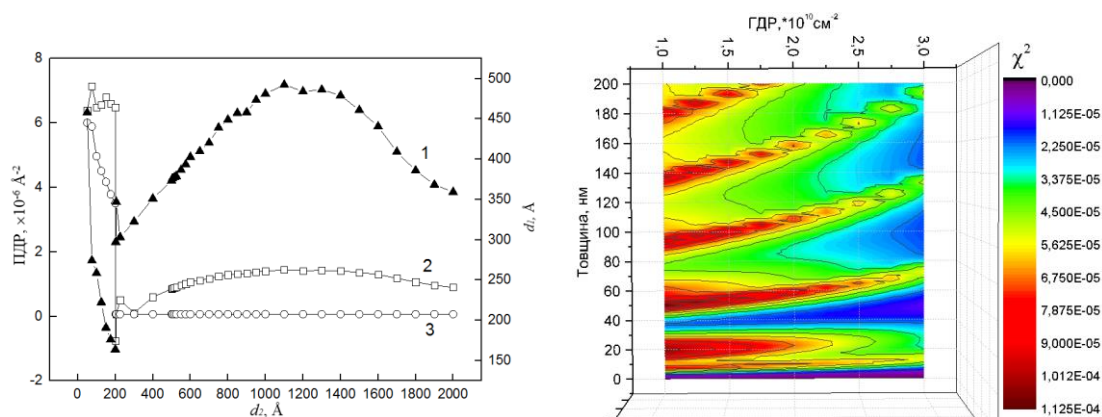
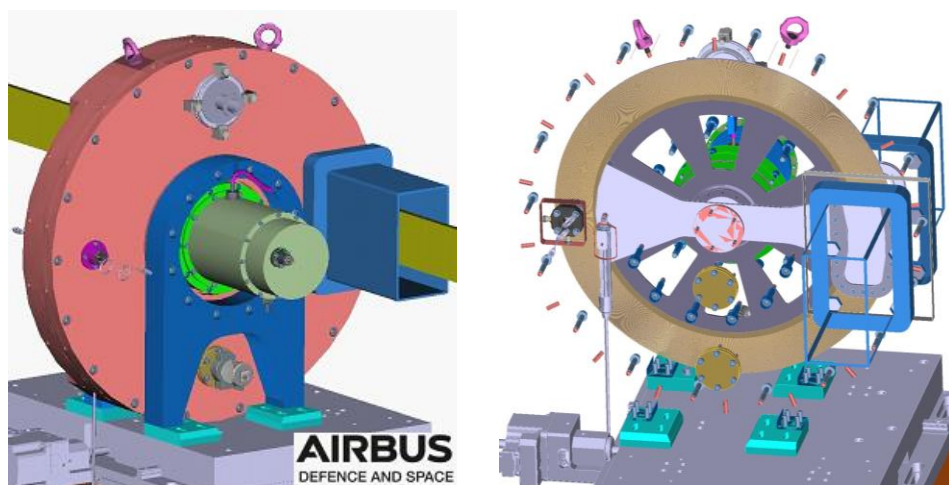


**Fig. 46.** (a) Dependence of optimal values of the thickness of carrier layer  $d_1$  (curve 1), SLD of carrier layer  $\rho_1$  (curve 2), SLD of solution  $\rho_s$  (curve 3) on the thickness of the adsorption layer  $d_2$  while fixing other parameters. (b) Dependence of the sensitivity of a reflectometry experiment on the thickness and density of the adsorption layer –  $\chi^2$  ( $d_2, \rho_2$ ) for the copper electrode.

On the GRAINS reflectometer, the modules of the SONIX+ software package for controlling the instrument were further developed and improved (debugging was performed, new services and options were added). The reorganization of communication lines was carried out: old cables were replaced and new cables for the control system were laid. The vacuum system was replaced.

Within the framework of the development of the FSD diffractometer, it is planned to manufacture a new Fourier chopper with an improved design and performance characteristics, which will be a rotor-stator system in a vacuum case (**Fig. 47**). A distinctive feature of the chopper is the presence of real radial slits (cut in the material of the stator plate and rotor disk) with an absorbing coating of  $^{10}\text{B}$  isotope. As a source of pickup signals, it is proposed to use a laser beam passing through the slits of the chopper, which will allow measuring the real transmission function exactly corresponding to the modulation of the neutron beam. This design will provide more accurate PID control and make it possible to eliminate phase errors (phase shifts of the pickup signal relative to the neutron signal), minimize the absorption and scattering by the material of the stator disk, and ensure less vibration and low gamma background. Thus, this will significantly improve the quality of diffraction patterns, i.e. reduce the background, increase the intensity of spectra and improve the profile and symmetry of diffraction peaks. The contract for manufacturing a new Fourier chopper for the FSD diffractometer was concluded with Airbus Defense and Space (Germany). At present, the design, basic technical solutions and parameters have been developed and agreed; the work has started on the fabrication of the main units of the Fourier chopper and control system.



a)

b)

**Fig. 47.** Model of a new Fourier-chopper for FSD: a) fully equipped in a vacuum case, b) internal structure of the chopper.

On the FSD diffractometer, a number of activities were performed in the framework of the development of sample environment systems. In particular, a Lauda Ultracool UC4 circulation chiller was installed for the MF-2000 mirror furnace, which is used to study the behavior of materials at high temperatures. On the mechanical uniaxial testing machine LM-29, the adaptation and installation of a new force sensor ( $F_{\max} = 125 \text{ kN}$ ) was carried out, which significantly expanded the range of available loads for sample testing. New Epsilon Tech extensometers were purchased, tested and installed for measurements of macrostrains of samples at room and high temperatures.

The development of the FSS Fourier diffractometer on IBR-2 beamline 13 was continued in cooperation with the SC Department. Radial collimators were installed on FSS in front of both Ost and West  $90^\circ$ -detectors, and the first experiments were carried out with the selection of a small scattering volume in the sample. At the exit of the mirror neutron guide of FSS, a new automated diaphragm (JJ X-RAY, Denmark) was installed and tested, which allows fast focusing of an incident neutron beam with the desired dimensions on the sample under study. To improve the performance characteristics of the diffractometer, a new mirror neutron guide with a vacuum housing was installed, which allows a several-fold increase of the flux in the short wavelength region. The neutron guide is designed to be plane-parallel in the horizontal plane (window width 10 mm) and linearly converging in the vertical plane (heights of the entrance and exit windows are 126 mm and 50 mm, respectively). Sections of the new neutron guide have a Ni/Ti supermirror glass coating with a critical index of  $m = 2$  (**Fig. 48**). The radius of curvature of the neutron guide is  $R = 1900 \text{ m}$ , and the characteristic wavelength is  $\lambda_c = 0.95 \text{ \AA}$ . Test experiments showed that the replacement of the neutron guide significantly extends the operating range in the region of small wavelengths and allows one to reliably detect up to 14 diffraction peaks of ferritic steel (**Fig. 48**). A comparative analysis of spectral distributions (**Fig. 48**) measured with the old and new neutron guides showed that there is a significant shift of the spectrum to short wavelengths ( $\Delta\lambda \approx 1.4 \text{ \AA}$ ). In this case, a significant decrease in the background from fast neutrons and gamma radiation is observed. A similar comparison for high-resolution RTOF diffraction spectra showed a significant increase in the intensity in the short-wavelength region of the diffraction spectrum. The level of the resolution of the diffractometer, determined for a standard sample, is  $\Delta d/d \approx 5.5 \cdot 10^{-3}$  at  $d = 2 \text{ \AA}$ ; the working range of interplanar distances is  $d_{hkl} = 0.5 \div 3.5 \text{ \AA}$ . To test the sensitivity of the instrument to shift and broadening of diffraction peaks, an experiment was performed on scanning a 10-mm thick EBW steel plate welded by electron beam welding. A small scattering volume (gauge volume) of  $2 \times 2 \times 10 \text{ mm}^3$  in the

depth of the sample material was defined using radial collimators installed in front of the Ost and West detectors. From the measurements for the specimen of the EBW steel plate, we obtained microstrain distributions (estimated from the broadening of diffraction peaks compared to the standard sample), as well as the distribution of residual stresses and strains (**Fig. 48**).

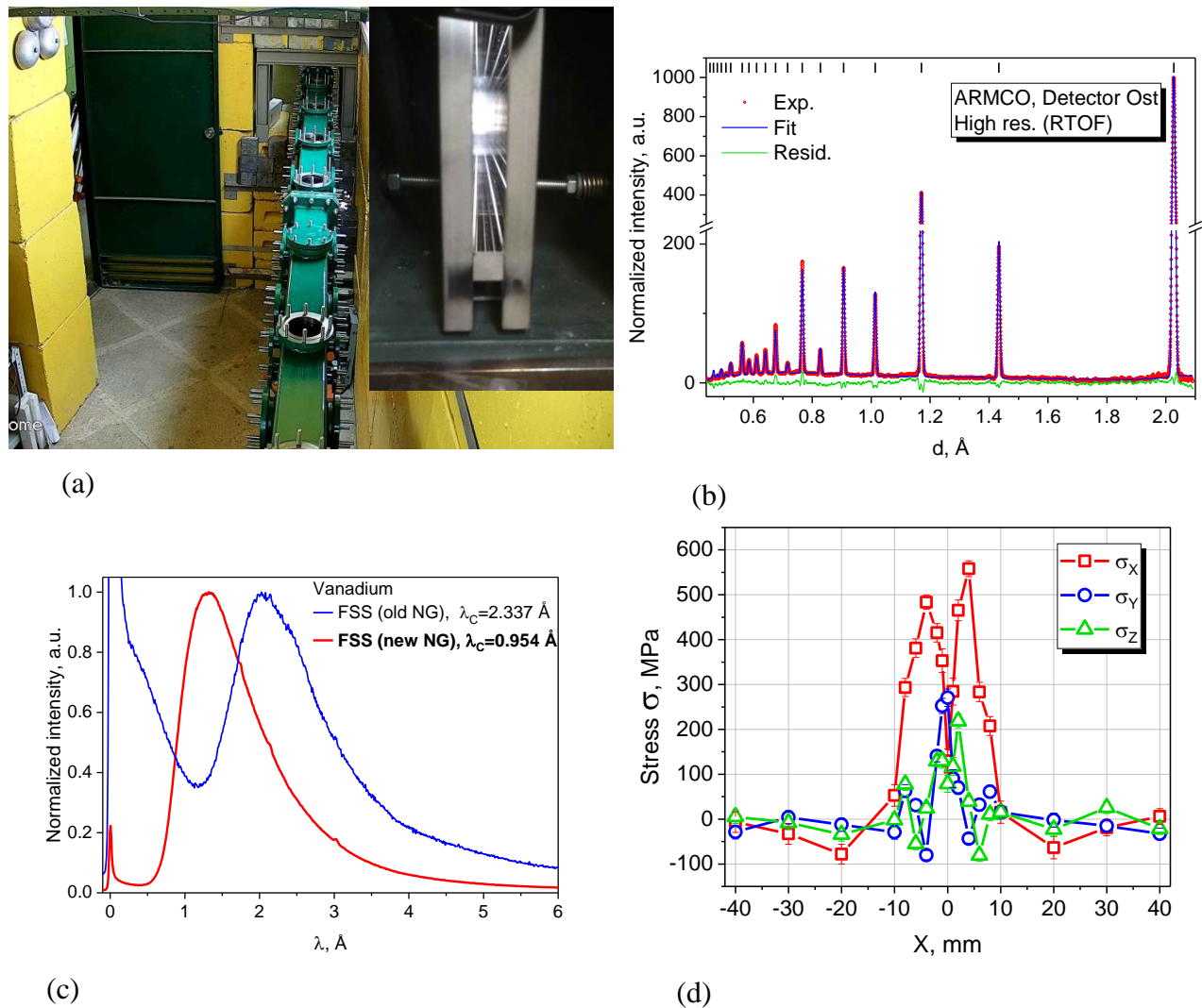


**Fig. 48.** Vacuum housing and mirror sections of the new neutron guide at FSS, beamline 13 of IBR-2 (a). High-resolution RTOF diffraction spectra from an ARMCO iron sample measured on FSS and treated by the Rietveld method (b). Comparison of spectral distributions measured on FSS with the old and new neutron guides (c). Stress distributions obtained for EBW sample (d).

On the REMUR reflectometer, the equipment for detecting secondary radiation over three channels (spin-flip neutrons, charged particles, and gamma rays) was put into operation (**Fig. 49**). At a typical set of instrument parameters ( $q$ -resolution – 10%, neutron wavelength – 1.5 Å, neutron beam cross section – 0.1 cm<sup>2</sup>, and neutron flux –  $2 \times 10^4$  n/cm<sup>2</sup>/s for a studied layer with a thickness of 5 nm), one can detect 22 isotopes in the charged particle detection channel, more than 100 isotopes in the gamma-ray detection channel, and obtain the minimum value of magnetization of a layer at the level of 1 G in the spin-flip neutron detection channel. Further progress, which will make the entire periodic table of elements available for research, is associated with an increase in the neutron intensity (by a factor of 10), a decrease in the background of fast neutrons and gamma-rays from the reactor core (by a factor of 5), and the use of a super-mirror neutron reflector (resolution of 1 Å).

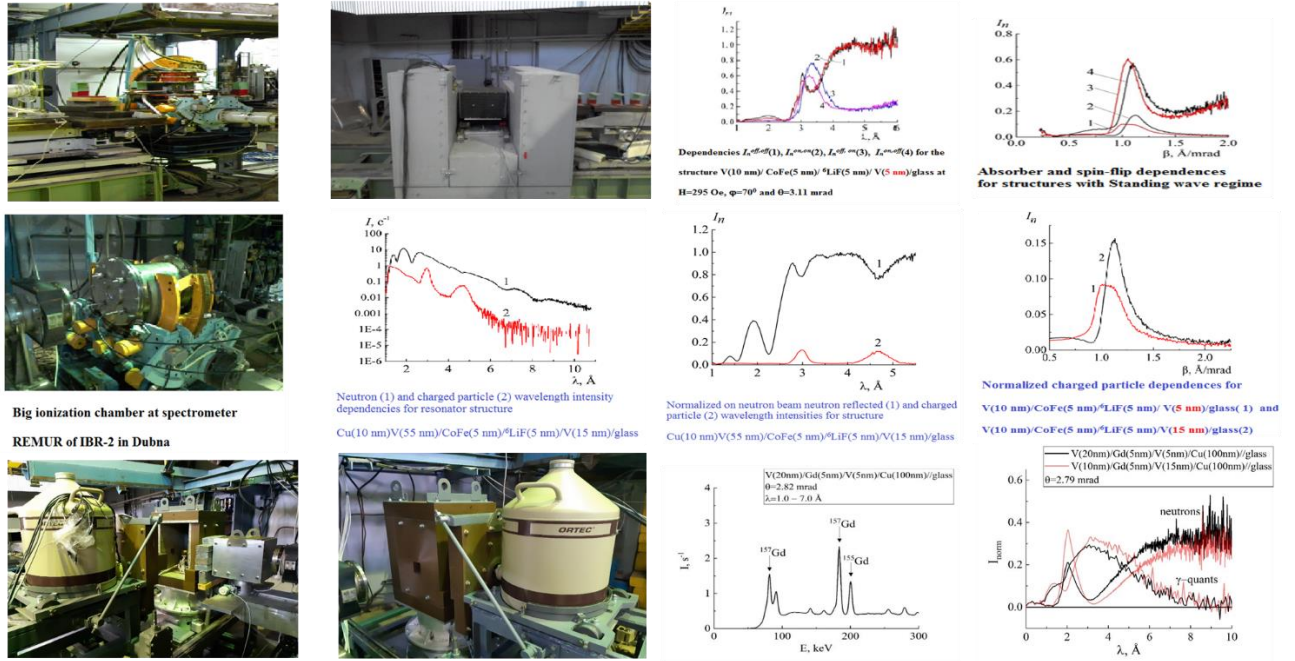


**Fig. 49.** Top: components of the charged particle channel – spin-flipper, guide field magnets, electromagnet, polarization analyzer with shielding. Right: dependences of reflected neutron intensity for four neutron spin transitions, secondary radiation intensity for two structures differing in position of magnetic (two upper curves) and absorbing (two lower curves) layers from the neutron reflector (5 and 15 nm). Middle row: charged particle detection channel – ionization chamber and experimental data. Bottom: a semiconductor gamma-ray detector and experimental data.

In the framework of the development of the prototype configuration of the SESANS spectrometer, in 2018, new spin rotators with a water cooling system (**Fig. 50**) were designed. They are characterized by a long-term operation with sawtooth current pulses with an amplitude of up to 200 A and provide the required characteristics of generated magnetic fields. According to the design model created using the SolidWorks software (**Fig. 50**), the use of liquid cooling will make it possible to increase the magnetic field gradient up to  $15 \times 10^4$  Gs/s. The new parameters will allow methodological measurements to be conducted on IBR-2 beamline 9 on the prototype of SESANS spectrometer with increased sensitivity. Water cooling radiators for spin rotators (**Fig. 50**) and magnetic cores made from ARMCO steel were manufactured in the FLNP workshops. Some radiators for power electronics have been manufactured and are ready for use (**Fig. 50**). The necessary chillers with a cooling rate of about 10 kW for the circulation of cooled water through the cooling circuits of the spin rotator coils and power electronics, were purchased. At present, the manufacturing of electromagnetic coils and corresponding cooling system according to the developed design documentation is in progress.

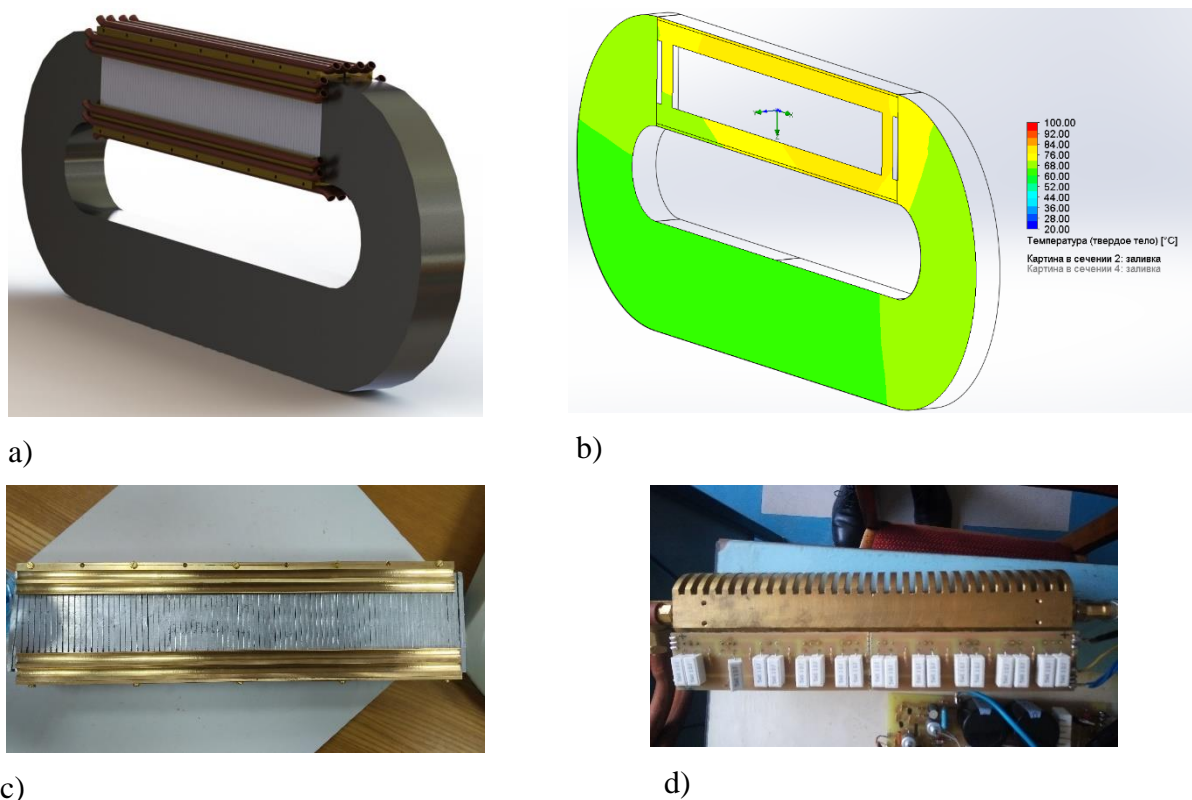
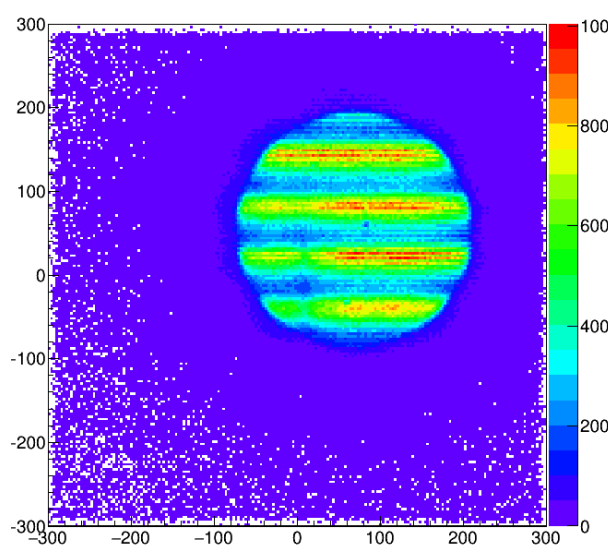


**Fig. 50.** a) Design of spin rotator coil with cooling system. Cooling radiators and magnetic cores for closing magnetic lines are made from ARMCO steel. b) Temperature distribution in spin rotator with liquid cooling. c) Water cooling radiators for spin rotators. d) Brass radiator with air-liquid cooling for transistors of power supply electronics.

The modernization of the YuMO spectrometer was continued. The main areas of work were the design of an additional changeable collimator, development of the sample environment system, and tests of a new-type position-sensitive detector. The software of the spectrometer was upgraded. In particular, in collaboration with LIT, algorithms were developed, the code was written and verified, measurements were carried out using a new program for processing experimental spectra from the position-sensitive detector (isotropic scattering) [42]. Experiments were carried out to estimate the required exposition time for measurements at the YuMO spectrometer. Estimates of the qualitatively necessary experimental time for one- and two-detector variants were made. It was shown that the use of the two-detector configuration of the experiment reduces the measuring time more than twice. When solving structural problems using modern software, the two-detector system provides a new qualitative level of data used in further analysis. The results of the work can be used in planning experiments at the YuMO spectrometer and in modernization of other instruments using the time-of-flight technique. The results are described in more detail in [43].

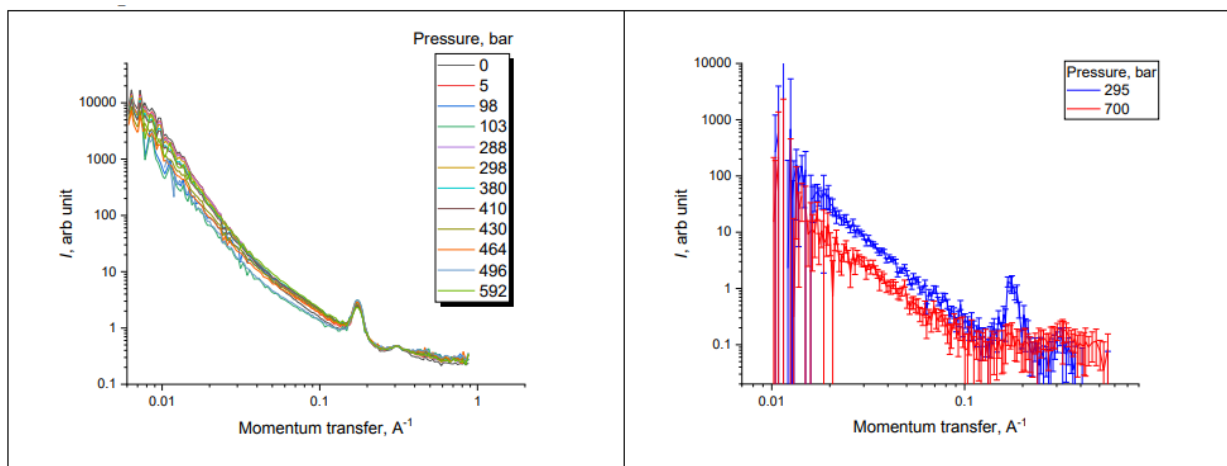
Experiments aimed at obtaining spectra, measuring fluxes and photographing the moderator were carried out on the YuMO instrument (**Fig. 51**). The measurements were made at the reduced reactor power of 400 kW. The compensator of the detector vessel was dismantled. The position-sensitive detector was placed in the beam. For photographing, the camera-obscura technique was used. The measurements were performed in the air at a flight path of more than 31 m and with the distance from the collimating pin-hole of about 14 m. The stable character of the neutron spectrum was observed. It was shown that flux spectra in maxima and minima (corresponding to the grooved moderator) do not differ. The ratio between the integral fluxes in the cavity and ridge was estimated to be a factor of 5. During the summer maintenance period, the grooved moderator was dismantled and later installed in its former position. The

measurements showed that the moderator was installed in its previous position with high accuracy.



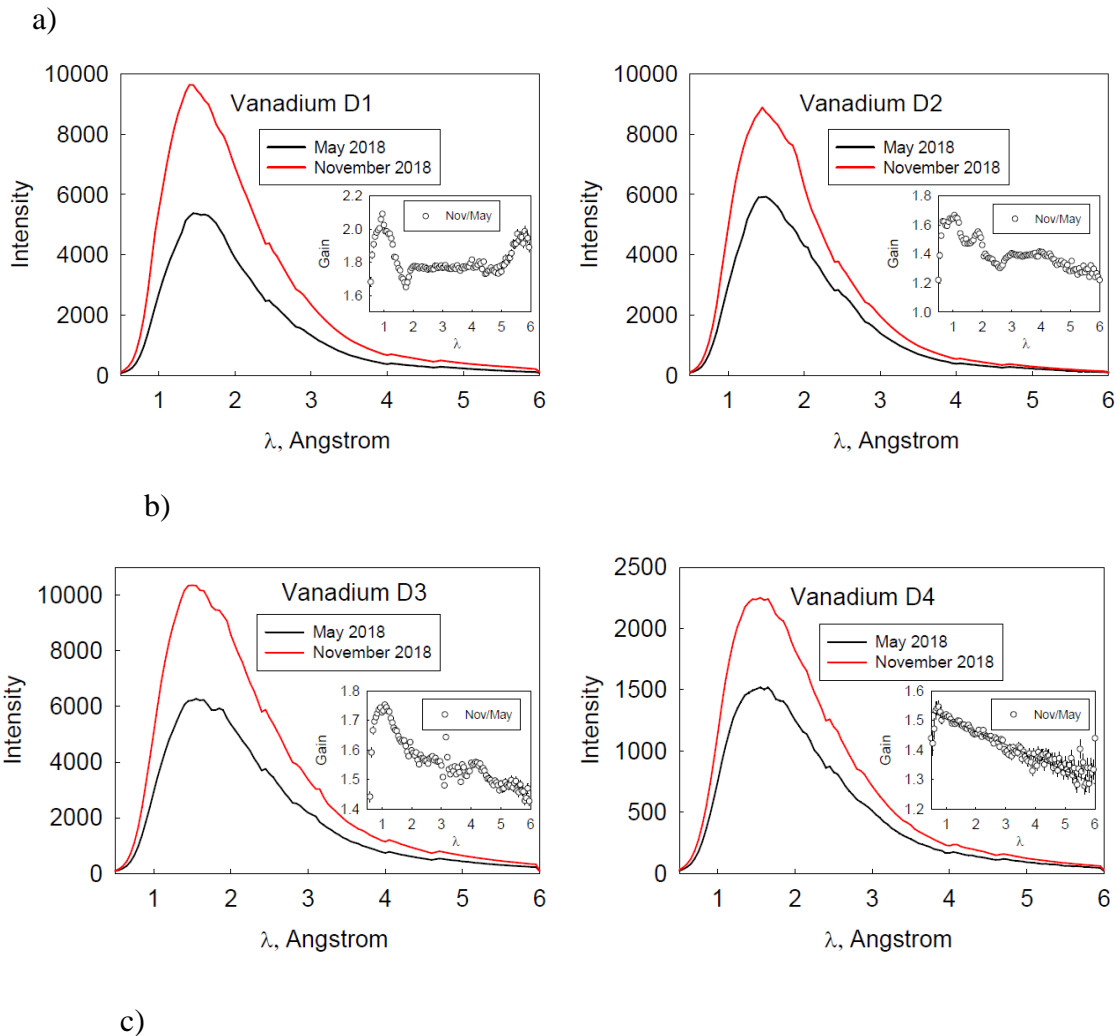
**Fig. 51.** Image obtained using a position-sensitive detector in the camera-obscura geometry at flight paths of 30 m (moderator-detector) and 14 m (cadmium pinhole diaphragm-detector).

Also, new non-standard equipment was tested at the spectrometer. A lithium-oxygen cell with control over the discharge process in the model system, was tested. A pressure cell (received from MEPhI) was used to study the filling of pores in granules of non-hydrophobized and hydrophobized  $\text{SiO}_2$  modified with alkylsilane in the pressure range from atmospheric to 800 bar (**Fig. 52**).



**Fig. 52.** SANS curves obtained for MCM-41-C1 sample under changes of pressure with  $\text{D}_2\text{O}$  (left) and 38%  $\text{D}_2\text{O}$  + 62%  $\text{H}_2\text{O}$  (right).

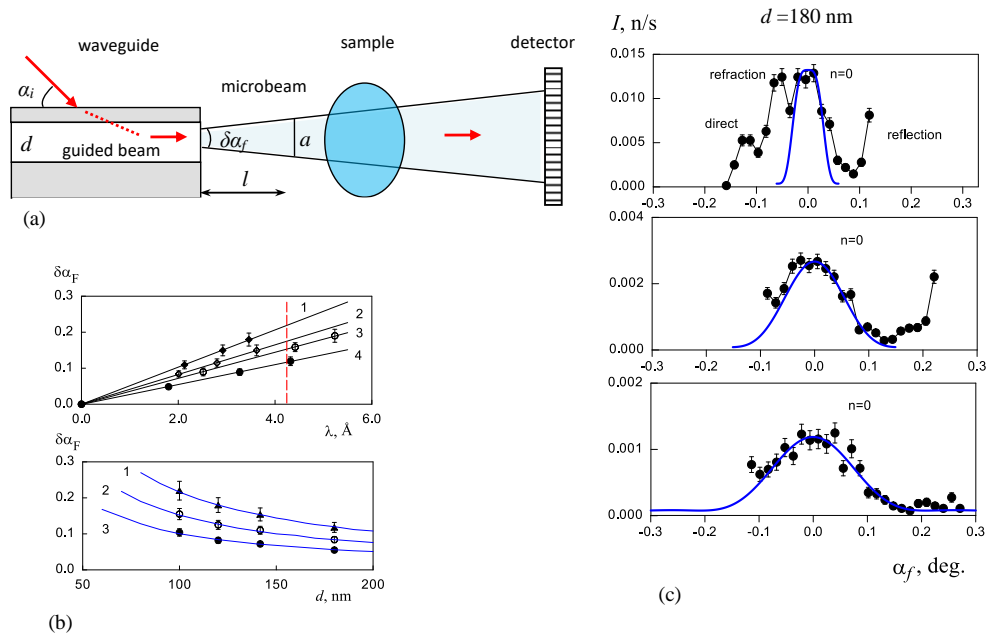
In the framework of the modernization of the NERA spectrometer, the end part of a conventional mirror neutron guide ( $m = 1$ ) 25 m long (full length of the entire neutron guide is about 100 m) was replaced with a supermirror neutron guide with vertical focusing ( $m \approx 5$ ) designed and manufactured by Swiss Neutronics. The average gain factor for the flux of thermal and cold neutrons at the sample position was about 1.5 (**Fig. 53**).



**Fig. 53.** a) Elements of supermirror neutron guide with vertical focusing for the NERA spectrometer. b), c) Spectral distribution of the neutron flux density measured by different detectors for vanadium sample before (May 2018) and after (November 2018) replacement of the end part of the old neutron guide ( $m = 1$ ) with a new supermirror neutron guide with vertical focusing ( $m = 5$ ).

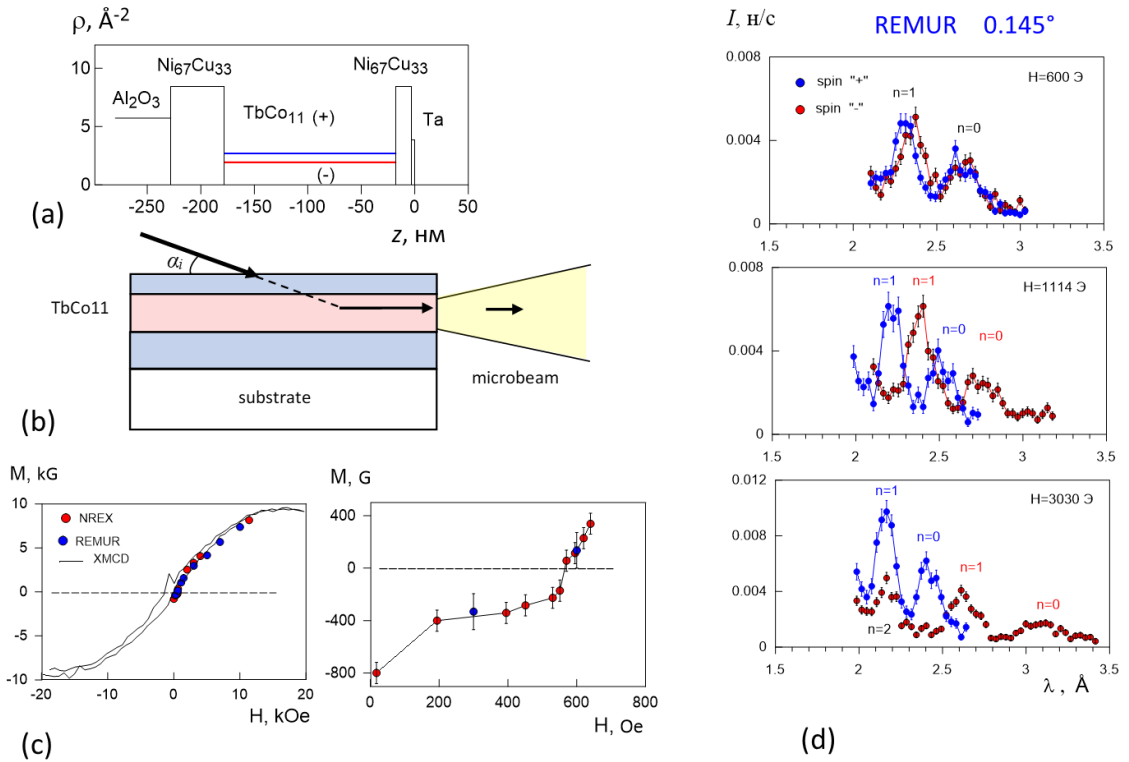
On the REMUR reflectometer, the divergence of a neutron microbeam outgoing from the edge of a planar waveguide was studied as a function of the neutron wavelength and the waveguide channel width [44]. The obtained experimental data are described in the framework of the conditions of Fraunhofer diffraction on a narrow slit. The divergence of the microbeam corrected on the angular divergence of the initial beam and the angular resolution of the detector increases linearly with increasing neutron wavelength and decreases inversely to the waveguide

channel width (**Fig. 54**). Additional measurements on the NREX reflectometer (reactor FRM-II, Garching, Germany) with a fixed wavelength confirmed that the divergence of the microbeam decreases inversely to the waveguide channel width.



**Fig. 54.** a) Geometry of an experiment with a neutron microbeam. b) Divergence of the microbeam corrected on the angular divergence of the initial beam and the angular resolution of the detector as a function of neutron wavelength (top, channel width 100 nm (1), 120 nm (2), 140 nm (3) and 180 nm (4)) and of the waveguide channel width (bottom,  $\lambda = 4.26$  Å (1),  $3.0$  Å (2) and  $2.0$  Å (3)). c) Dependence of the microbeam intensity on the angle of the scattered beam for channel width of 180 nm and fixed initial grazing angle of the beam:  $0.152^\circ$  (top),  $0.281^\circ$  (middle),  $0.369^\circ$  (bottom).

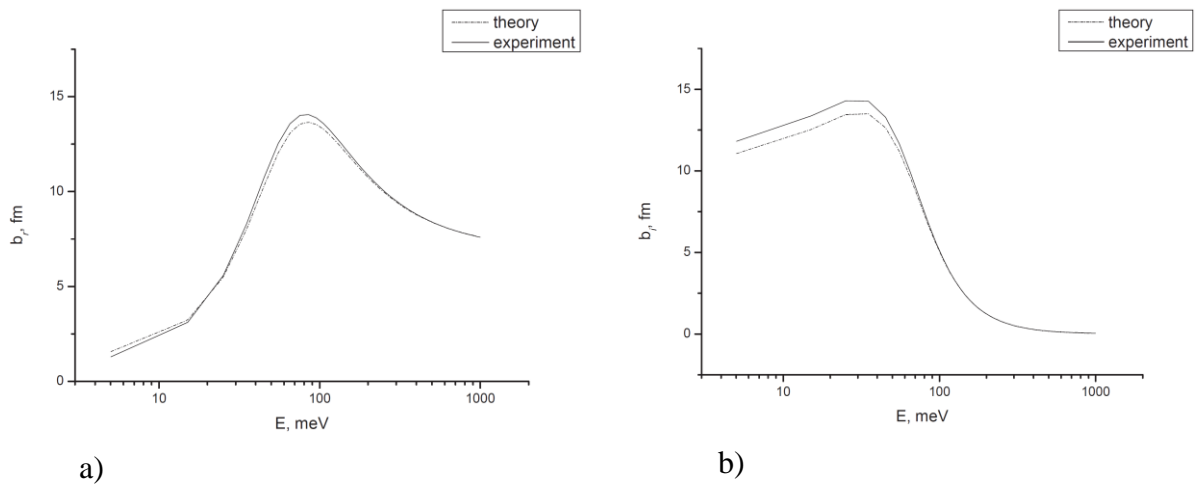
A technique for channeling polarized neutrons was developed to determine weak (of the order of 100 G) magnetization of films [45]. For this purpose, a resonant waveguide structure was used, in which the studied magnetic film with a low neutron scattering length density (SLD) was placed between two non-magnetic layers with a high SLD (**Fig. 55**). Inside this magnetic film, resonantly amplified neutron standing waves are formed, in which the position of resonances over neutron energy depends on the magnetization magnitude and the sign of the incident beam polarization. Neutrons propagate along the middle layer and exit the end of the film in the form of a narrow diverging microbeam. In the experiment on the REMUR reflectometer, a microbeam spectrum was recorded for the initial polarization states “+” and “-”. From the experimentally found positions of the resonance peaks of the 0-th order for the spin states “+” and “-”, the magnetization of the  $\text{TbCo}_{11}$  film (150 nm) was determined. The magnetization curve of the film obtained using neutrons in absolute units was combined with the hysteresis loop measured in arbitrary units using the X-ray magnetic circular dichroism (XMCD) method. The saturation magnetization of the film was about 10 kG; the sensitivity of the method – about 50 G.



**Fig. 55.** Scattering length density profile of resonant waveguide nanostructure (a), neutron beam propagation geometry (b), magnetization curve (c), scattered neutron spectra measured using the REMUR reflectometer (d).

The REFLEX reflectometer was used to determine the complex scattering length of gadolinium [46]. The interest to this problem is due to the possibilities of using Gd as a reference layer in layered structures studied by neutron reflectometry. Unlike most nuclei, the Gd nucleus has an absorption resonance, and both real and imaginary parts of its scattering length depend on the neutron wavelength. This dependence can significantly simplify the task of determining the scattering length density profile from neutron reflectometry data, since the dependence of the reflection coefficient on the momentum transfer in the presence of a reference Gd layer in the structure will significantly depend on the angle of incidence of incident radiation. Thus, measurements at different angles will provide several independent models for determining the scattering length density profile. To implement this approach, it is necessary to know the exact dependence of the scattering length of the reference layer on the neutron wavelength. The time-of-flight method is suitable for obtaining this dependence in a wide spectral range.

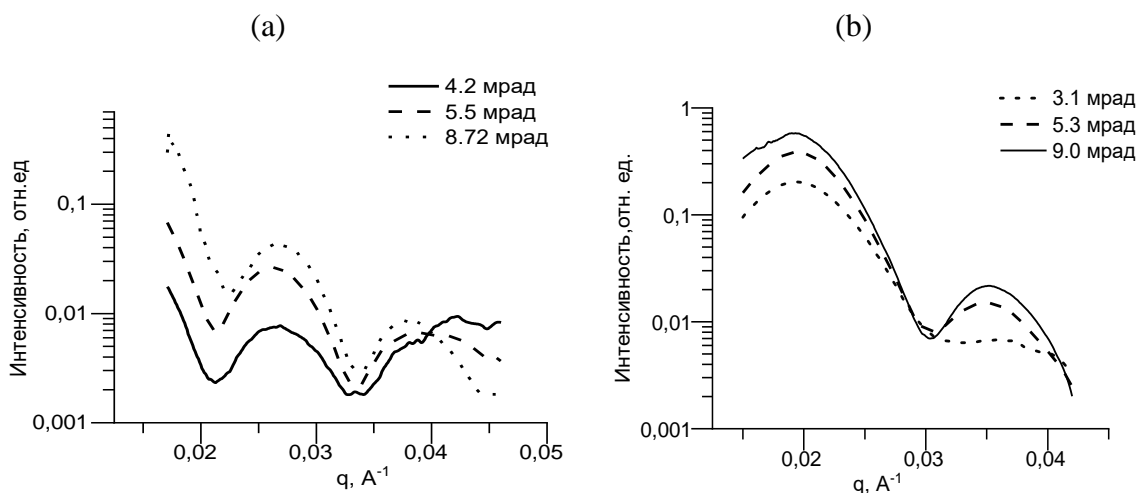
To experimentally determine the dependence of the scattering length of Gd on the neutron wavelength  $\lambda$  (Fig. 56), a neutron beam in the range of 1-10  $\text{\AA}$  was transmitted through a 5000- $\text{\AA}$ -thick Gd film placed at an angle  $\alpha$  to the incident beam. This configuration resulted in an effective increase in the thickness of the absorbing layer for more efficient data collection. The sample was prepared by magnetron sputtering at the "ULVAC" facility, IPM, UB RAS, Yekaterinburg.



**Fig. 56.** Experimental and calculated dependences of real (a) and imaginary (b) parts of scattering length of Gd on neutron energy.

On the REFLEX reflectometer, the possibility of using the resonant neutron scattering by Gd atoms for the experimental determination of the phase of the reflection coefficient in neutron reflectometry, was tested [46]. A series of three experiments was carried out with different scattering lengths of Gd in the reference layer in order to determine the complex reflection coefficient at various grazing angles (**Fig. 57**). The choice of angles was dictated by the need to use the neutron wavelength range, in which the maximum differences in reflectometry spectra are observed based on the numerical simulation results. Using the refined Gd scattering characteristics and structural parameters determined by X-ray reflectometry, an optical matrix was calculated for the Gd/V reference layer. Then, the modulus and phase of the complex reflection coefficient were calculated.

By measuring the neutron specular reflection coefficient for three different wavelengths for each value of momentum transfer, it was possible to solve the phase problem of neutron reflectometry and determine the modulus and phase of the complex reflection coefficient for the unknown part of the sample.



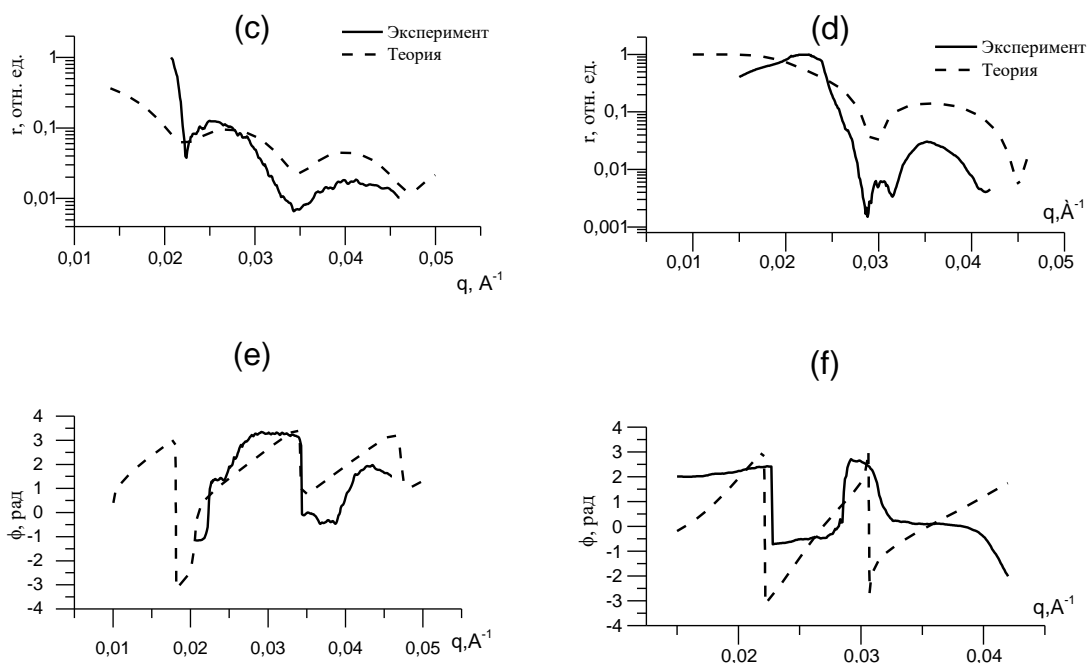


**Fig. 57.** Experimental and calculated neutron reflectometry curves for Si//Ti(550Å)/Gd(50Å)/V(50Å) and (b) Si//Cr(300Å)/Fe(300Å)/Cr(200Å)/Gd(50Å)/V(50Å) samples. Experimental and calculated modulus (c) and phase (e) of the complex reflection coefficient for Si//Ti(550Å) and module (d) and phase (f) of the complex reflection coefficient for Si//Cr(300Å)/Fe(300Å)/Cr(200Å).

A comparative analysis of theoretical calculations and experimental results of determining the modulus and phase of the complex reflection coefficient by the Gd reference layer method shows their good qualitative agreement. The worst consistency is observed within the region of small scattering vectors (below 0.02 Å<sup>-1</sup>) corresponding to large neutron wavelengths, which is explained by the weak energy dependence of the scattering length of Gd in this range. For the correct determination of the reflection coefficient in this interval, it is necessary to carry out additional measurements at smaller grazing angles. The obtained experimental results are in good qualitative agreement with the results of theoretical calculations performed for a model with nominal structural parameters. It can be expected that further development of the proposed method will make it possible to solve the phase problem of neutron reflectometry, including the studies of magnetic systems.

Using the VITESS software package, the influence of the background at the IBR-2 reactor on the reflectometry measurements was evaluated. For this purpose, the operation of a pulsed source with characteristics close to those of the IBR-2 reactor was simulated. A neutron flux formed by the main pulse was superimposed by a constant-in-time flux imitating a background induced, among other things, by the emission of delayed neutrons. The neutron flux in the constant-in-time background was chosen to be equal to 10% of the average flux of a pulsed source (**Fig. 58**). The moderator temperature of both sources (main and background) was assumed to be the same and amounted to 300 K. The simulation of reflectometry measurements showed that for the same neutron spectrum in the beam and the background, the delayed neutrons begin to smooth the specular reflection curves only at sufficiently high momentum transfer. This effect is insignificant in the working  $q$ -ranges of reflectometers at IBR-2 (**Fig. 58**). However, an increase in the effect should be expected in the case of a harder spectrum of the background, which is added to the reflected beam. Thus, the addition of a background component of 0.05% of the neutron flux incident on the sample to the time spectrum of the reflected beam results in a significant smoothing of the reflection curves to a minimum recorded

value of  $10^{-4}$ . Thus, this work shows the need for experimental measurements of the background spectrum at the IBR-2 reactor.

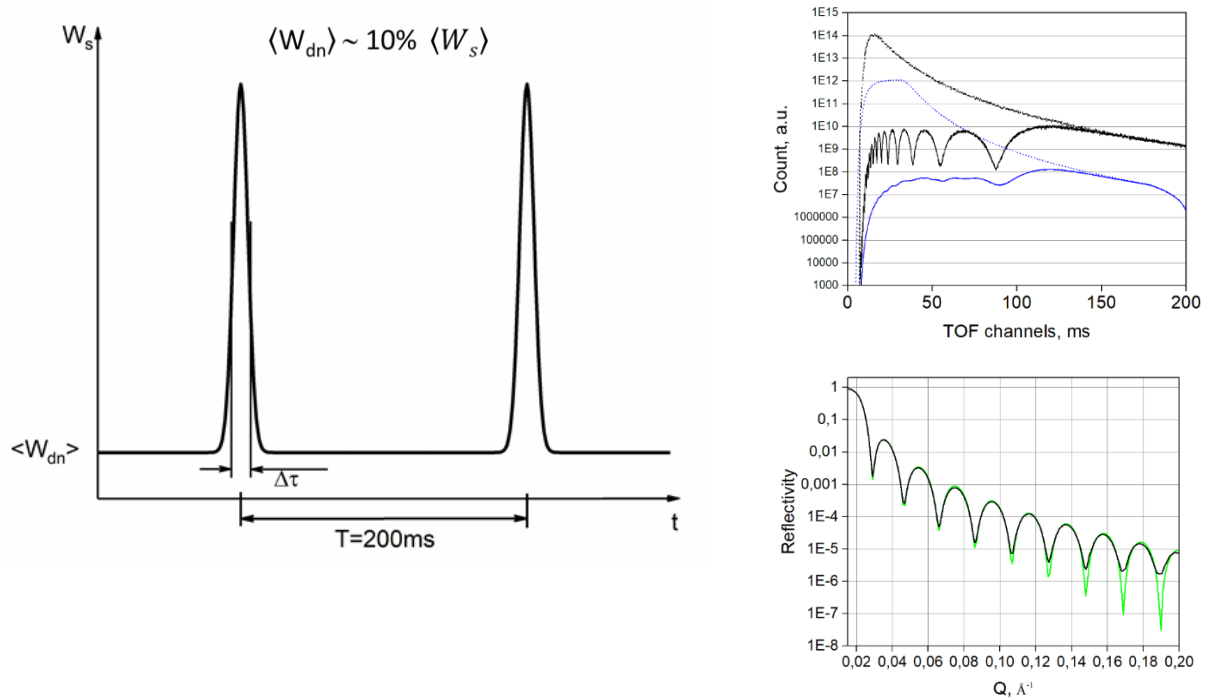


**Fig. 58.** Left: shape of the neutron power pulse in model calculations (the model generates two Gaussian pulses of the  $W_s$  source with a half-width  $\Delta\tau = 300 \mu\text{s}$ ; the additional background source produces a continuous neutron flux). Right: TOF spectra of direct and reflected beams for two sources separately (Top). Blue – delayed neutrons, black – neutrons from a pulsed source. The dotted line corresponds to direct beams, the solid line – reflected beams. Reflectivity curves with (black) and without (green) background source (Bottom).

In collaboration with the Institute of Nuclear Physics of the Ministry of Energy of the Republic of Kazakhstan (Almaty, Kazakhstan), the work on the design of a new instrument of radiography and tomography at the VVR-K stationary research reactor, as well as on the ordering and purchasing of special equipment and materials was conducted. The basic configuration of the instrument and biological shield were installed on beamline № 1 in the experimental hall of the reactor (**Fig. 59**). The thermal neutron flux measured at the exit of beamline № 1 is  $\sim 4.5 \times 10^8 \text{ n/cm}^2/\text{s}$ . First test experiments were performed, which demonstrated good prospects for using the neutron radiography and tomography facility at the VVR-K reactor for neutron research in various fundamental and applied research areas. The instrument was put into operation in November 2019.

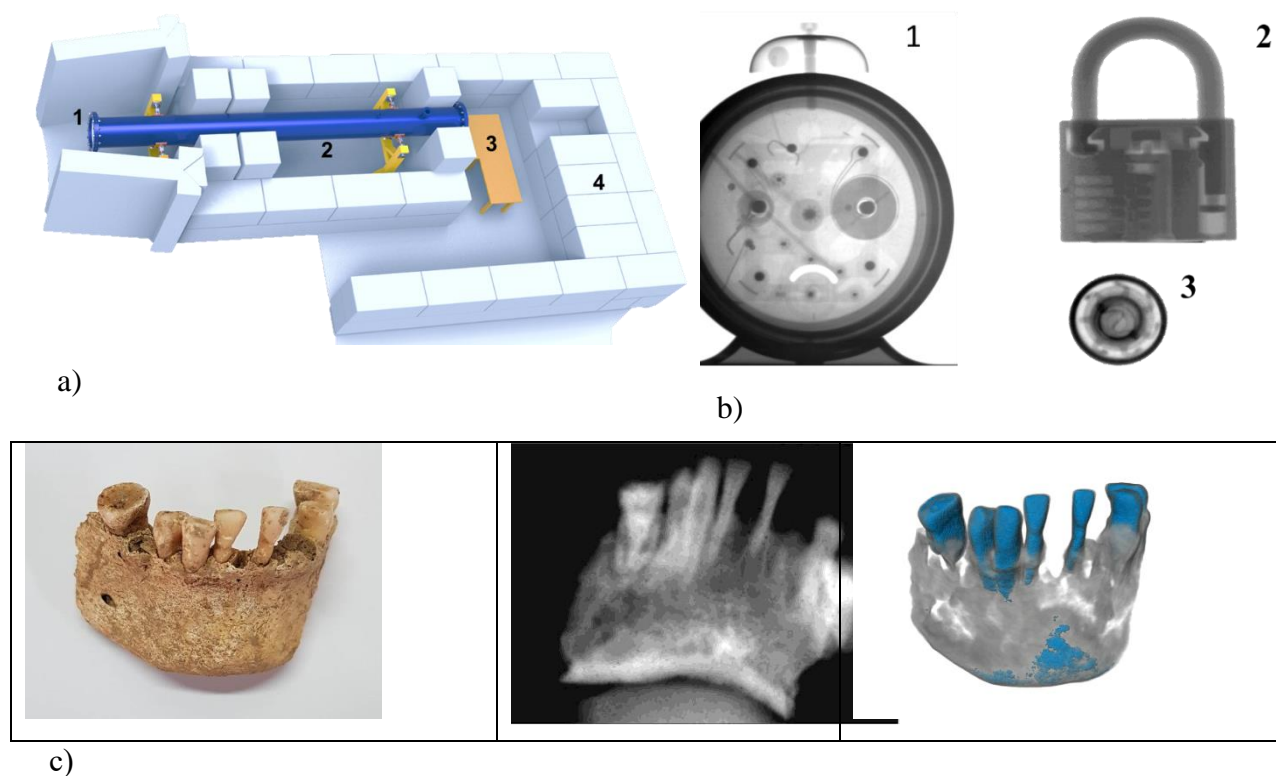


**Fig. 59.** a) Scheme of the basic configuration of the neutron radiography and tomography facility on beamline 1 of the VVR-K reactor: 1 – place of the shutter of experimental neutron beamline № 1; 2 – vacuum housing of the system of collimators forming a neutron beam; 3 – location of the detector system and positioning goniometers for neutron tomographic experiments; 4 – elements of concrete shielding against ionizing radiation exposure during neutron experiments. b) First neutron images obtained on the neutron radiography and tomography station of the VVR-K reactor: 1 – neutron image of an alarm clock; 2 – neutron image of a padlock; 3 – neutron image of the rotor of a small engine. c) Photo, neutron image and three-dimensional model of the lower jaw of a man of the Saka era found in burial mound №1 (village of Rakhat, Almaty region) obtained by neutron tomography.

An electrochemical cell was designed and manufactured for studying the structural and microstructural parameters of electrode materials using X-ray diffraction (**Fig. 60**). The cell is adapted for the use in a PANalytical Empyrean diffractometer. The weight of the assembled cell is 370 g, height – 45 mm, width – 64 mm. To avoid corrosion caused by organic solvents, all metal parts of the cell are made of a stainless alloy of HN60MB type.

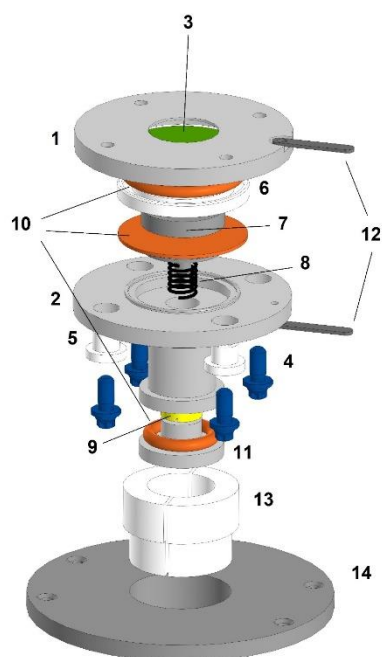


**Fig. 60.** A cell with a beryllium window for studying electrode materials in *operando* mode on an X-ray diffractometer. The cell consists of two body parts (1, 2); beryllium disk (3) with a diameter of 36.2 mm and thickness of 0.5 mm; four TORX E10 bolts (thread M5; length – 10 mm) with an internal hexagon with washers and bushings (4, 5); guide insert (6) of polyetheretherketone (PEEK) with a cavity for an electrolyte; composite current-collector substrate (7); spring (8, stainless steel, size 9 mm×1mm×6; length – 11 mm; recommended stiffness 0.4-0.7 N/mm), adjustable limiter with thread (9); 3 gaskets of various diameters and shapes (10) (recommended material is fluorinated rubber); screw cover (11); two current collector plates (12) fastened with screws to the cell body parts. Fastening to the 3-axis platform of the diffractometer is performed through plastic dielectric bushings (13) and aluminum disk support (14).

## References

1. J.Cong, K.Zhai, Y.Chai, D.Shang, D.D.Khalyavin, R.D.Thompson, D.P.Kozlenko et al., Spin-induced multiferroicity in the binary perovskite manganite  $\text{Mn}_2\text{O}_3$ . *Nature Communications* 9, 2996 (2018).
2. D.P.Kozlenko, N.T.Dang, N.O.Golosova, S.E.Kichanov, E.V.Lukin, P.J.Lampen Kelley, E.M.Clements, K.V.Glazyrin, S.H.Jabarov, T.L.Phan, B.N.Savenko, H.Srikanth, and M.H.Phan. Pressure-induced modifications of the magnetic order in the spin-chain compound  $\text{Ca}_3\text{Co}_2\text{O}_6$ . *Phys. Rev. B* 98, 134435 (2018).
3. D.P.Kozlenko, L.S.Dubrovinsky, S.E.Kichanov, E.V.Lukin, V.Cerantola, A.I.Chumakov, B.N.Savenko. Magnetic and electronic properties of magnetite across the high-pressure anomaly. *Scientific reports* 9, 4464 (2019).
4. A.M.Balagurov, I.A.Bobrikov, I.S.Golovin. Anomalous Behavior of an  $\alpha \rightarrow \gamma$  Phase Transition in Iron: Results of In Situ Neutron Diffraction Experiment. *JETP Letters*, 107, 558-563 (2018).
5. A.M.Balagurov, I.A.Bobrikov, S.V.Sumnikov, I.S.Golovin. Dispersed clusters in  $(\text{Fe,Cr})_3\text{Al}$  alloys: Neutron time-of-flight diffraction study. *Physical Review Materials*, Vol. 3, no. 1 (2019).
6. A.M.Balagurov, I.A.Bobrikov, I.S.Golovin. Effects of Ordering in  $\text{Fe-xAl}$  Alloys. *JETP Letters*, Vol. 110, No. 9, pp. 585–591 (2019).

7. A.M.Balagurov, N.Yu.Samoylova, I.A.Bobrikov, S.V.Sumnikov and I.S.Golovin. The first- and second-order isothermal phase transitions in Fe<sub>3</sub>Ga-type compounds. *Acta Cryst. B* 75, pp.1024-1033 (2019).
8. A.V.Nagorny, V.I.Petrenko, M.Rajnak, I.V.Gapon, M.V.Avdeev, B.Dolnik, L.A.Bulavin, P.Kopcansky, M.Timko. Particle assembling induced by non-homogeneous magnetic field at transformer oil-based ferrofluid/silicon crystal interface by neutron reflectometry. *Appl. Surf. Sci.* 473, 912 (2019).
9. P.A.Selyshchev, V.I.Petrenko, M.Rajnak, B.Dolnik, J.Kurimsky, P.Kopcansky, M.Timko, L.A.Bulavin, Non-uniform distribution of ferrofluids spherical particles under external electric field: Theoretical description. *Journal of Molecular Liquids* 278 (2019) 491–495.
10. O.Kyzyrna, N.Bashmakova, Yu.Gorshkova, O.Ivankov, I.Mikheev, M.Kuzmenko, S.Kutovyy, T.Nikolaienko. Interaction between the plant alkaloid berberine and fullerene C<sub>70</sub>: experimental and quantum-chemical study. *J.Mol.Liq.* 278, 452 (2019).
11. S.V. Tomylo, O.V. Tomchuk, O.I. Ivankov, V. Ryukhtin, L.A. Bulavin, M.V. Avdeev. Multilevel structure of diamond nanoparticles – liquid crystal composites // *Materials Today: Proceedings* (2018).
12. T.V.Tropin, M.L.Karpets, Ye.Kosiachkin, V.L.Aksenov. X-ray reflectometry for comparison of structural organization of fullerenes C<sub>60</sub>/C<sub>70</sub> in polystyrene thin films. *Fullerenes, Nanotubes and Carbon Nanostructures* (2019) in press.
13. O.V.Tomchuk, M.V.Avdeev, A.E.Aleksenskii, A.Y.Vul, O.I.Ivankov, V.V.Ryukhtin, J.Füzi, V.M.Garamus, L.A.Bulavin. Sol-gel transition in nanodiamond aqueous dispersions by small-angle scattering. *Journal of Physical Chemistry C* 123 (2019) 18028-18036.
14. M.V.Avdeev, I.A.Bobrikov, V.I.Petrenko. “Neutron methods for tracking lithium in operating electrodes and interfaces”. *Physical Sciences Reviews* (2018) 20170157.
15. M.V.Avdeev, A.A.Rulev, E.E.Ushakova, Ye.N.Kosiachkin, V.I.Petrenko, I.V.Gapon, E.Yu.Kataev, V.A.Matveev, L.V.Yashina, D.M.Itkis. On nanoscale structure of planar electrochemical interfaces metal/liquid lithium ion electrolyte by neutron reflectometry. *Applied Surface Science* 486 (2019) 287–291.
16. V.A.Vizgalov, T.Nestler, A.Vyalikh, I.A.Bobrikov, O.I.Ivankov, V.Petrenko, M.V.Avdeev, L.V.Yashina, D.M.Itkis. The role of glass crystallization processes in preparation of high Li-conductive NASICON-type ceramics. *CrystEngComm* 21 (2019) 3106-3115.
17. M.V.Avdeev, M.S.Yerdauletov, O.I.Ivankov, S.A.Bocharova, F.S.Napolsky, V.A.Krivchenko. On the effect of carbon additives on the porosity of positive electrodes based on LiFePO<sub>4</sub> for lithium-Ion batteries. *Journal Surface Investigation.* 13 (2019) 614-618.
18. T.K.Zakharchenko, M.V.Avdeev, A.V.Sergeev, A.V.Chertovich, O.I.Ivankov, V.I.Petrenko, Y.Shaoh-Horn, L.V.Yashina and D.M.Itkis. Small-angle neutron scattering studies of pore filling in carbon electrodes: mechanisms limiting lithium–air battery capacity. *Nanoscale* 11 (2019) 6838-6845.
19. V.D.Zhaketov, Yu.V.Nikitenko, A.V.Petrenko, S.N.Vdovichev, A.V.Churakov, A.Csik. Reflexivity and correlation of magnetic states of nanostructures in the Nb(70nm)/Ni<sub>0.65</sub>Cu<sub>0.35</sub>(6.5nm)//Si ferromagnet-superconductor heterostructure. *JETP* 127, 508 (2018).
20. A.A.Lezov, A.S.Gubarev, A.N.Podsevalnikova, A.S.Senchukova, E.V.Lebedeva, M.M.Dudkina, A.V.Tenkovtsev, T.N.Nekrasova, L.N.Andreeva, R.Yu.Smyslov, Yu.E.Gorshkova, G.P.Kopitsa, A.Rădulescu, V.Pipich, N.V.Tsvetkov. Temperature-responsive star-shaped poly(2-ethyl-2-oxazoline) and poly(2-isopropyl-2-oxazoline) with central thiacalix[4]arene fragments: structure and properties in solutions. *Colloid and Polymer Science* 297, 285 (2019).

21. N.Kučerka, Hrubovčák P., Dushanov E., Kondela T., Kholmurodov Kh.T., Gallová J., Balgavý P. Location of the general anesthetic n-decane in model membranes. *J. Mol. Liq.*, 276, 624 (2019).
22. A.Zeleňáková, P.Hrubovčák, O.Kapusta, N.Kučerka, A.Kuklin, O.Ivankov, & V.Zeleňák. Size and distribution of the iron oxide nanoparticles in SBA-15 nanoporous silica via SANS study. *Scientific Reports*, 9(1), 1-9 (2019).
23. M.A.Kiselev, D.N.Selyakov, I.V.Gapon, A.I.Ivankov, O.M.Ipatova, V.L.Aksenov, M.V.Avdeev. Investigation of Nanodrug Phospholipovit by Small-Angle Neutron Scattering. *Crystallography Reports* 64 (2019) 656-661.
24. A.A.Nabiyev, A.K.Islamov, A.M.Maharramov, M.A.Nuriyev, R.S.Ismayilova, A.S.Doroshkevich, A.Pawlukojc, V.A.Turchenko, A.Olejniczak, M.Ī.Rulev, V.Almasan, A.I.Kuklin. "Structural Studies of dielectric HDPE+ZrO<sub>2</sub> polymer nanocomposites: filler concentration dependences", *Journal of Physics: Conference Series*, 994 (2018) 012011.
25. J.W.P.Schmelzer, T.V.Tropin. Kinetic criteria of vitrification and pressure-induced glass transition: dependence on the rate of change of pressure. *Thermochimica Acta*, V.677, pp.42-53 (2019).
26. J.W.P.Schmelzer, T.V.Tropin. Glass transition, crystallization of glass-forming melts, and entropy. *Entropy*, 20(2), 103 (2018).
27. O.P.Artykulnyi, V.I.Petrenko, L.A.Bulavin, O.I.Ivankov, M.V.Avdeev. Impact of poly (ethylene glycol) on the structure and interaction parameters of aqueous micellar solutions of anionic surfactants. *Journal of Molecular Liquids* 276 (2019) 806–811.
28. O.V.Tomchuk, M.V.Avdeev, O.I.Ivankov, L.A.Bulavin, V.L.Aksenov. Features of colloidal aggregation in tetraetoxisilan/water/ethanol ternary mixtures by small-angle neutron scattering. *Journal Surface Investigation* 12 (2019) 3-7.
29. R.Keppeler. Crystallographic preferred orientations in eclogites – A review. *Journal of Structural Geology* 115, 284 (2018).
30. M.Neikter, R.Woracek, T.Maimaitiyili, Ch.Scheffzük, M.Strobl, M.-L.Antti, P.Åkerfeldt, R.Pederson & C.Bjerkén. "Alpha texture variations in additive manufactured Ti-6Al-4V investigated with neutron diffraction", *J. Additive Manufact.* 23, 225 (2018).
31. M.L.Fedoseev, S.N.Petrov, A.K.Islamov, N.F.Drozdova, T.A.Lychagina, D.I.Nikolaev "Multimethodological approach to the study of carbide particle dimensions in high-strength steel", *Letters on Materials*, 8, 323 (2018).
32. A.I.Ziza, M.S.Mikhailov, V.V.Tsukanov, D.I.Nikolaev, T.A.Lychagina. A study of retained austenite transformation during high-strength Cr-Ni-Mo-V steel tempering. *Letters on Materials*, 8, 146 (2018).
33. D.I.Nikolayev, T.A.Lychagina, A.A.Zisman, E.A.Yashina. Directly verifiable neutron diffraction technique to determine retained austenite in steel. *Advanced Engineering Materials*, 20 (4), 2018 <https://doi.org/10.1002/adem.201700559>.
34. A.Badmaarag, Ch.Scheffzük, D.Sangaa, I.Hishigdemberel, L.Enkhtur. Investigation of internal residual microstrain of quartz-containing polycrystalline sample using neutron time-of-flight diffraction method. Submitted to *Journal of Institute of Physics and Technology* (2018) (in Mongolian).
35. E.Gadalińska, A.Baczmański, S.Wroński, P.Kot, M.Wroński, M.Wróbel, Ch.Scheffzük, G.Bokuchava, K.Wierzbowski. "Neutron diffraction study of phase stresses in Al/SiC<sub>p</sub> composite during tensile test". *Metals and Materials International* 25 (2019) 657-668.
36. P.Kot, A.Baczmański, E.Gadalińska, S.Wroński, M.Wroński, M.Wróbel, G.Bokuchava, Ch.Scheffzük, K.Wierzbowski. "Evolution of phase stresses in Al/SiC thermal cycling and compression test studied using diffraction and self-consistent models". *Journal of Materials Science and Technology* (2019), doi: 10.1016/j.jmst.2019.03.046.

37. D.I.Nikolayev, T.A.Lychagina, A.V.Pakhnevich. Experimental neutron pole figures of minerals composing bivalve mollusc shells. *Springer Nature Applied Science*, 2019, 1:344.
38. T.A.Lychagina, D.I.Nikolayev, M.BalasoIU, M.Nicu, L.Ionascu, A.C.Dragolici, F.Dragolici. Aging Studies of Low pH Cement-Based Materials Used for Aluminum Radioactive Waste Conditioning. 2019, *Romanian Journal of Physics* 64, 802.
39. S.E.Kichanov, D.P.Kozlenko, A.K.Kirillov, E.V.Lukin, B.Abdurakhimov, N.M.BelozeroVA, A.V.Rutkauskas, T.I.Ivankina, B.N.Savenko. A structural insight into the Chelyabinsk meteorite: neutron diffraction, tomography and Raman spectroscopy study. *Springer Nature Applied Sciences* 1:1563 (2019).
40. V.I.Petrenko, Ye.N.Kosiachkin, L.A.Bulavin, M.V.Avdeev. Optimization of the initial interface configuration for in-situ neutron reflectometry experiments. *Journal of Surface Investigation: X-ray, Synchrotron and Neutron Techniques*, Vol. 14, No. 2, pp.215–219 (2020).
41. V.I.Petrenko, Ye.N.Kosiachkin, L.A.Bulavin, M.V.Avdeev. “On Enhancement of the Adsorption-Layer Effect at the Metallic Electrode–Liquid Electrolyte Interface in Specular Neutron Reflectometry Experiments”, *Journal of Surface Investigation: X-ray, Synchrotron and Neutron Techniques*, 12(4) (2018) 651–657.
42. A.Soloviev, S.Kutuzov, O.Ivankov, A.Kuklin. "Primary Data Treatment Software for Position-Sensitive Detector of Small-Angle Neutron Scattering Spectrometer in the Isotropic Pattern Scattering Case", *EPJ Web Conf.* 173, 05015 (2018).
43. A.I.Kuklin, O.I.Ivankov, D.V.Soloviev, A.V.Rogachev, Y.S.Kovalev, A.G.Soloviev, A.K.Islamov, M.BalasoIU, A.V.Vlasov, S.A.Kutuzov, A.P.Sirotin, A.S.Kirilov, V.V.Skoi, M.I.Rulev, V.I.Gordeliy "High-throughput SANS experiment on two-detector system of YuMO spectrometer", *Journal of Physics: Conference Series* 994, 012016 (2018).
44. S.V.Kozhevnikov, V.D.Zhaketov, T.Keller, Yu.N.Khaydukov, F.Ott, F.Radu, “Divergence of neutron microbeams from planar waveguides”, *NIM A* (2018), doi: 10.1016/j.nima.2018.10.211.
45. S.V.Kozhevnikov, V.D.Zhaketov, T.Keller, Yu.N.Khaydukov, F.Ott, Chen Luo, Kai Chen, F.Radu. Polarized neutron channeling in weakly magnetic films. *NIM A* 927 (2019) 87.
46. E.S.Nikova, Y.A.Salamatov, E.A.Kravtsov, V.I.Bodnarchuk, V.V.Ustinov. Experimental determination of gadolinium scattering characteristics in neutron reflectometry with reference layer. *Physica B: Condensed Matter*, 552 (2019) 58–61.

## 5. Financing of theme 1121

Planned budget for theme 1121

	2018 kUSD	2019 kUSD	2020 kUSD
Consumables	588.4	861	264
Equipment	712.6	576	395.6
R&D	70.0	58.0	20.0
Scientific and Information Support	–	20	15.0
ISTC	168.7	168.7	168.7
<b>Total</b>	1539.7	1683.7	863.3

Additional sources of financing – 900 kUSD per year, including:

Grants and programs of Plenipotentiaries of Poland, Czech Republic, Slovakia, Romania, Kazakhstan, Bulgaria;

BMBF-JINR Agreement;

South Africa-JINR Agreement;

Egypt-JINR Agreement;

Serbia-JINR Agreement;

RSF Grants;

RFBR Grants.

**List of organizations collaborating with the NICM Department.**

**Collaboration:**

<b>Country or international organization</b>	<b>City</b>	<b>Institute or Laboratory</b>
JINR	Dubna	BLTP, VBLHEP, LRB, FLNR, DLNP, LIT
Azerbaijan	Baku	IP ANAS, AzTU
Argentina	Bariloche	CNEA
Belarus	Minsk	BSU, IAP NASB, INP BSU, SPMRC NASB, RI PCP BSU, NC PHEP BSU, RIPChP BSU
	Grodno	SUG
Bulgaria	Sofia	IMS BAS, ISSP BAS, IE BAS, IEES BAS, INRNE BAS
Czech Republic	Prague	IG CAS, IMC CAS, IP CAS, CTU, BC CAS
	Ostrava	V\ v SB-TUO
	Rez	NPI CAS
Egypt	Cairo	EAEA,CU
France	Grenoble	IBS
	Saclay	LLB
Germany	Berlin	HZB, BAM
	Bayreuth	Univ.
	Bochum	RUB
	Halle	MLU
	Hamburg	DESY
	Gottingen	Univ.
	Geesthacht	HZG
	Darmstadt	TU Darmstadt
	Dortmund	TU Dortmund
	Dresden	TU Drezden, IKTS
	Kiel	CAU, IFM-GEOMAR
	Karlsruhe	KIT
	Konstanz	Univ.
	Potsdam	GFZ
	Rostock	Univ.
	Stuttgart	MPI-FKF
Freiberg	TUBAF, IMF TUBAF	
Hungary	Julich	FZJ
	Budapest	Wigner RCP
	Szeged	US

India	Gurgaon	Amity Univ.	
	Patna	NIT Patna	
Japan	Matsumoto	Shinshu Univ.	
	Minato	Keio Univ.	
Kazakhstan	Almaty	INP	
	Rudny	RII	
Latvia	Riga	ISSP UL, IPE	
Moldova	Chisinau	IMB ASM	
Mongolia	Ulaanbaatar	IPT MAS, MUST	
Norway	Trondheim	NGU	
Poland	Warsaw	INCT	
	Białystok	UwB	
	Wroclaw	WUT, UW	
	Krakow	JU, NINP PAS, AGH-UST	
	Lublin	UMCS	
	Lodz		
	Poznan	AMU	
	Swierk	NCBJ	
	Siedlce	UPH	
	Szczecin	WPUT	
	Russia	Moscow	GC RAS, IA RAS, IBMC, IC RAS, IEPT RAS, IGEM RAS, IGIC RAS, IMET RAS, INMI RAS, ICP RAS, NRC Institute of Immunology FMBA, ITEP, IPE RAS, ISPM RAS, NNRU “MEPhI”, MIET, MITHT, MSU, NIKIET, NRC KI, SINP MSU, SC “VNIINM”, NUST “MISiS”, MUCTR, PIN RAS, IA RAS
		Moscow,	HPPI RAS, ISAN, INR RAS
		Troitsk	
Belgorod		BelSU	
Dolgoprudny		MIPT	
Dubna		Dubna Univ., LITON	
Gatchina		PNPI RAS	
Yekaterinburg		IMP UB RAS, USU	
Kazan		KSTU, KNRTU	
Kaliningrad		IKBFU	
Krasnoyarsk		IP SB RAS, SibFU	
Nizhny		UNN, IPM RAS	
Novgorod			
Perm		ICMM UrB RAS, ITCh UrB RAS	
Petrozavodsk		IG KarRC RAS	
Podolsk	GIDROPRESS		
Rostov-on-Don	RIP SFU		

	St. Petersburg	IPTI RAS, SPbSU, IMC RAS
	Sterlitamak	SSPI
	Tomsk	NPI TPU
	Tula	TSU
	Chernogolovka	ISSP RAS
Romania	Bucharest	IFIN-HH, INCDIE ICPE-CA, INFLPR, NIMP, ISS, UB, UPB, UMF, UTM
	Baia Mare	TUCN-NUCBM
	Constanta	UOC
	Craiova	UC
	Cluj-Napoca	I.N.C.D.T.I.M., RA BC-N, UBB, UTC-N
	Pitesti	SCN, UPIT
	Timisoara	ICT, ISIM, LMF CCTFA, UPT, UVT
	Targoviste	UVT
	Tulcea	DDNI
	Iasi	NIRDTP, UAI, UAIC, TUIASI, USAMV
Serbia	Belgrade	INS "VINCA"
	Novi Sad	UNS
Slovak Republic	Bratislava	CU
	Kosice	IEP SAS
South Africa	Pretoria	Necsa
Spain	Madrid	CENIM-CSIC
Switzerland	Villigen	PSI
	Zurich	ETH
Taiwan	Hsinchu	NSRRC
Tajikistan	Dushanbe	ICChem ASRT
United Kingdom	Didcot	RAL
Ukraine	Kiev	IPMS NASU, NTSU, ISC NASU
	Kharkov	IERT NASU, KFTI NASU
	Donetsk	DonIPE NASU, DonNU
Uzbekistan	Tashkent	INP UAS
Vietnam	Hanoi	IOP VAST
	Da Nang	DTU

**List of prizes awarded to the Department employees in 2018 – 2020.**

**JINR Prizes**

**2018**

I prize in nomination ‘Experimental Physics Research’ for a series of studies:

“Correlation of structure and physical properties in ordered iron-based alloys”.

Authors: A.M. Balagurov, I.A. Bobrikov, S.V. Sumnikov, I.S. Golovin, V.V. Palacheva.

I prize in nomination ‘Applied Research and Technology’ for a series of studies:

“Structure and properties of aqueous solutions of C60 and C70 fullerenes for biological applications”.

Authors: E.A. Kyzyma, V.I. Petrenko, O.I. Ivankov, M.V. Avdeev, V.L. Aksenov, L.A. Bulavin, Yu.I. Prylutsky.

**2019**

I prize in nomination ‘Applied Research and Technology’ for a series of studies:

“Application of neutron diffraction to study structural and microstructural transformations of Li-ion electrode materials during operation”.

Authors: I.A. Bobrikov, A.M. Balagurov, N.Yu. Samoylova, S.V. Sumnikov, O.Yu. Ivanshina, R.N. Vasin.

II prize in nomination ‘Applied Research and Technology’ for a series of studies:

“Neutron radiography and tomography at the pulsed high-flux IBR-2 reactor: development of the experimental facility and results of the interdisciplinary applied research”.

Authors: D.P. Kozlenko, S.E. Kichanov, A.V. Belushkin, E.V. Lukin, K. Nazarov, A.V. Rutkauskas, G.D. Bokuchava, B.N. Savenko, I.A. Saprikina.

## List of grants allocated for investigations conducted in the Department in 2018-2020.

№	Organization	Period	Title	Leader
1.	RSF	2017-2019	RSF Grant 17-12-01540 Monitoring and study of mesoscopic structures on planar and developed electrochemical interfaces for lithium power sources by neutron scattering.	M.V.Avdeev
2.	RSF	2017-2018	RSF Grant 17-12-00025 Development of small-angle scattering methods and investigation of vesicles and nanodrugs at neutron and synchrotron sources.	M.A.Kiselev
3.	RSF	2019-2022	RSF Grant 19-72-20080 Heterogeneous structural states in Fe-based alloys with magneto-mechanical coupling: correlation between physical and engineering properties (at IBR-2).	I.S.Golovin (NUST «MISiS» A.M.Balagurov (JINR)
4.	RSF	2019-2022	RSF Grant 19-75-20121 Novel hybrid and carbon aerogels – synthesis and structural studies using small-angle scattering methods (at IBR-2).	A.E.Baranchikov (IGIC RAS) Yu.Ye.Gorshkova (JINR)
5.	RSF	2019-2022	RSF Grant 19-72-20133 Microstructured hydrogels with embedded nanoparticles (at IBR-2).	O.E.Philippova (MSU) A.I.Kuklin (JINR)
6.	RSF	2019-2022	RSF Grant 19-72-20186 The effect of membrane fluidity and disorder on the location of peptides in model biological membranes studied by neutron scattering (at IBR-2).	N.Kucerka (JINR)
7.	RFBR	2017-2019	RFBR Grant 17-02-00112 “ Structural mechanisms of formation of magnetic properties of cobalt intermetallides: neutron studies at high pressures	B.N.Savenko
8.	RFBR	2018-2020	RFBR Grant 18-02-00359 “ Magnetic ordering and spin crossover in structurally complex cobalt oxides: neutron studies with variation of thermodynamic parameters	D.P.Kozlenko
9.	RFBR	2018-2020	RFBR Grant 18-02-00325 “ Coherent cluster ordering of atoms in	A.M.Balagurov

			iron-based intermetallic compounds	
10.	RFBR	2018-2020	RFBR Grant 17-52-44024_Mong_a “ Studies of the defect structure of nanosystems and transition processes in them using thermal neutron scattering	A.M.Balagurov
11.	RFBR	2018-2019	RFBR Grant 18-52-00020_Bel_a Complex study of the mechanism of exchange interactions, magnetotransport phenomena and spin transitions in cobaltites with perovskite-type structure	V.V.Sikolenko
12.	RFBR	2019-2020	RFBR Grant 19-52-45009_Ind_a Phase stabilization and its structural impact on magnetoelectric coupling in multiferroics $\text{Bi}_{2-x}\text{M}_x\text{WO}_6$ (M= Mn, Fe, Co).	S.E.Kichanov
13.	RFBR	2019-2020	RFBR Grant 19-12-50056 _Expansion Neutron scattering in studies of functional iron-based alloys (Fe-Ga, Fe-Al, etc.)	A.M.Balagurov